Nicholas M. N. Steinbrink

Beyond-Standard Model Neutrino Physics Sensitivity with KATRIN

2017

WWU
MÜNSTER

Experimentelle Physik

Dissertationsthema

Beyond-Standard Model Neutrino Physics Sensitivity with KATRIN

Inaugural-Dissertation
zur Erlangung des Doktorgrades der Naturwissenschaften
im Fachbereich Physik
der Mathematisch-Naturwissenschaftlichen Fakultät
der Westfälischen Wilhelms-Universität

vorgelegt von
Nicholas Martin Norman Steinbrink
aus Soest

2017

Dekan:	Prof. Dr. Michael Klasen
Erster Gutachter:	Prof. Dr. Christian Weinheimer
Zweiter Gutachter:	Prof. Dr. Gernot Münster
Tag der mündlichen Prüfung:	
Tag der Promotion:	

"*What a long way has passed to the modern scientist whose performance is permanently judged by how often his publications are cited in scientific journals! Meanwhile, he is confronted with the risk of reducing science to its pure "technical" aspect, being forced to integrate new technologies into his work regularly and to take the role of an administrator too often. (..) The scientist, however, may not become discouraged by such negligibility, tribute to a modernism being as demanding as stimulating. He must - and that is the essence of his profession - stay creative and that brings him close to the artist. (...) Considering all this, there is hope that the profession of the scientist like in the time of Leonardo da Vinci, while absolutely prioritizing scientific precision, more and more contributes to a synthesis of science and art, the fundamental constituents of human genius.*"

Christian Bréchot [1]

[1] Jean Claude Ameisen, *Quand l'art rencontre la science*, Preface. Translated from German ed., Frederking & Thaler, München (2007).

Abstract

Despite the success of the Standard Model (SM) as effective theory of particle physics, there is strong evidence of fundamental physics beyond the SM. In particular, the yet unknown nature of dark matter points to the existence of further stable particles and the discovery of neutrino oscillation showed that neutrinos are massive, contrary to the assumptions of the SM. The Karlsruhe Tritium Neutrino Experiment (KATRIN) aims at a measurement of the absolute neutrino mass with a 90 % C.L. sensitivity of 0.2 eV by measuring the endpoint region of the tritium β-decay spectrum from a windowless gaseous molecular tritium source using an integrating spectrometer of the MAC-E-Filter type. In this thesis, certain prospects of extending the sensitivity of KATRIN towards smaller neutrino mass scales and phenomena of physics beyond the SM are explored. Three particular issues are being studied.

1. In order to improve the absolute neutrino mass sensitivity, the idea of using the MAC-E-Filter in a time-of-flight mode (MAC-E-TOF) is being discussed, in which the neutrino mass is determined by a measurement of the electron time-of-flight (TOF) spectrum that depends on the neutrino mass. In principle, this method is especially sensitive, since the β-electrons are slowed down to distinguishable velocities by the MAC-E-Filter. Their velocity depends strongly on their surplus energy above the electric retarding potential. Using MAC-E-TOF, a statistical sensitivity gain is expected. Because a small number of retarding-potential settings is sufficient for a complete measurement, in contrast to about 40 different retarding potentials used in the standard integrating mode, there is a gain in measurement time and hence statistical power. The improvement of the statistical uncertainty of the squared neutrino mass has been determined by Monte Carlo simulation to be a factor 5 for an ideal case, neglecting background and timing uncertainty. Additionally, two scenarios to determine the time-of-flight of the β-electrons are discussed, which use the KATRIN focal plane detector (FPD) for creating the stop signal and different methods for obtaining a start signal. These comprise the hypothetical idea of *electron tagging*, where passing electrons are detected with minimum interference and the more realistic case of *gated filtering*, where the electron flux is periodically cut off by pulsing the pre-spectrometer potential.

2. Due to the sharp energy resolution and high source luminosity, KATRIN also has in principle some sensitivity on keV scale sterile neutrinos, which are promising candidates for warm dark matter (WDM). The mixing between active and sterile neutrinos with a mixing angle θ would lead to a second spectral component with a relative contribution of $\sin^2\theta$, located below the Q value minus the mass of the sterile neutrino. Since KATRIN is optimized for measurement of neutrino masses in the sub-eV range, the search for keV scale sterile neutrinos requires additional strategies to cope with the high count-rate in the parts of the spectrum, which are sensitive to the sterile neutrino, and to eliminate systematics, which are crucial due to the small expected mixing angle (astrophysical limit $\sin^2\theta \lesssim 10^{-7}$). Therefore, the idea of MAC-E-TOF spectroscopy is also applied to the scenario of keV scale sterile neutrinos. In particular,

this would help to suppress the systematics and to increase the signal-to-background ratio by distinguishing the parts in the β-spectrum with higher energies without sterile neutrino information. The sensitivity of a TOF mode to keV scale sterile neutrinos has been determined by Monte Carlo simulations. In order to extract the sensitivity from a model without sampling the full statistics of up to $\sim 10^{18}$ counts, a variant of importance sampling, called *self-consistent importance sampling* (SCIS) has been developed and used. The simulations show that an ideal TOF mode would be able to push the sensitivity by nearly half an order of magnitude in terms of $\sin^2\theta$ statistics-wise. If exemplary systematics in the form of an unknown column density in the tritium source, determining the inelastic scattering probability, are included, the benefit grows to over an order of magnitude. In addition, the implementation of the TOF via gated filtering has been simulated. It is shown that, for the most simple implementation, this method would not be superior to the integral mode; however, additional optimizations of the detector and timing parameters are possible, which could further improve the performance.

3. In addition to the sterile neutrino hypothesis, certain models of non-standard neutrino interactions may also have implications for the tritium β-spectrum. An example are weak non $V - A$-contributions, also denoted as right-handed currents. They can for instance be mediated by right-handed W bosons in the left-right symmetric model (LRSM). In this extension of the SM, an additional $\mathrm{SU(2)_R}$ symmetry in the high-energy limit is introduced, which naturally includes sterile neutrinos and predicts the seesaw mechanism. In tritium β-decay, this leads to an additional term from interference between left- and right-handed interactions, which enhances or suppresses certain regions near the endpoint of the beta spectrum. The sensitivity of KATRIN to right-handed currents is estimated for the scenario of a light sterile neutrino with a mass of some eV. This has been performed with a Bayesian analysis using Markov Chain Monte Carlo (MCMC). The simulations show that in principle KATRIN is able to set sterile neutrino mass-dependent limits on the interference strength. The sensitivity is significantly increased, if the Q value of the β-decay can be sufficiently constrained. However, the sensitivity is not high enough to improve current upper limits from right-handed W boson searches at the LHC.

Zusammenfassung

Trotz des Erfolgs des Standardmodells (SM) als effektive Theorie der Teilchenphysik gibt es starke Evidenz für fundamentale Physik jenseits des SM. Insbesondere die bisher unbekannte Natur der dunklen Materie weist auf die Existenz weiterer stabiler Teilchen hin, und die Entdeckung der Neutrinooszillation hat gezeigt, dass Neutrinos entgegen der Annahmen des SM massiv sind. Das Ziel des Karlsruher Tritium Neutrino Experiments (KATRIN) ist eine Bestimmung der absoluten Neutrinomasse mit einer Sensitivität von 0.2 eV bei 90 % Konfidenzniveau durch Messung des Endpunktbereichs des Tritium β-Zerfallsspektrums aus einer fensterlosen, gasförmigen, molekularen Tritiumquelle mithilfe eines integrierenden Spektrometers des MAC-E-Filter-Typs. In dieser Arbeit werden gewisse Möglichkeiten erforscht, die Sensitivität von KATRIN in Richtung kleinerer Neutrinomassenskalen und Phänomene jenseits des Standardmodells zu erweitern. Drei Beispiele werden dabei behandelt.

1. Um die absolute Neutrinomassensensitivität zu verbessern, wird die Idee diskutiert, den MAC-E-Filter in einem Flugzeitmodus (MAC-E-TOF) zu benutzen, in dem die Neutrinomasse durch Messung des Flugzeitspektrums der Elektronen bestimmt wird, welches von der Neutrinomasse abhängt. Prinzipiell ist diese Methode besonders empfindlich, da die β-Elektronen durch den MAC-E-Filter auf unterscheidbare Geschwindigkeiten abgebremst werden. Die Geschwindigkeit hängt stark von der Überschussenergie oberhalb des elektrischen Retardierungspotentials ab. Mithilfe der MAC-E-TOF-Spektroskopie wird ein Anstieg der Sensitivität erwartet. Weil bereits eine kleine Anzahl von Potential-Einstellungen, im Gegensatz zu ungefähr 40 verschiedenen Retardierungspotentialen im integrierenden Standardmodus, für eine Messung ausreicht, steht mehr Messzeit und somit mehr Statistik zur Verfügung. Die Verbesserung der statistischen Unsicherheit des Neutrinomassenquadrats wurde unter Annahme eines idealen Falls ohne Untergrund und mit optimaler Zeitauflösung mittels Monte Carlo-Simulation auf einen Faktor 5 beziffert. Zusätzlich werden zwei Szenarien diskutiert, um die Flugzeit der β-Elektronen zu bestimmen, welche den KATRIN Focal Plane Detector (FPD) zur Erzeugung eines Stop-Signals und verschiedene Methoden zur Erzeugung eines Start-Signals verwenden. Diese umfassen die hypothetische Idee des *Electron Taggings*, bei der einfallende Elektronen mit minimaler Inteferenz registriert werden und den realistischeren Fall des *Gated Filterings*, bei dem der Elektronenfluss durch Pulsen des Vorspektrometer-Potentials periodisch abgeschnitten wird.

2. Aufgrund der scharfen Energieauflösung und der hohen Quellstärke hat KATRIN im Prinzip auch eine gewisse Sensitivität auf sterile Neutrinos mit Massen von einigen keV, welche vielversprechende Kandidaten für warme dunkle Materie (WDM) sind. Die Mischung zwischen aktiven und sterilen Neutrinos mit einem Mischungswinkel θ würde zu einer zweiten spektralen Komponente mit einem relativen Beitrag von $\sin^2\theta$ führen, welche sich unterhalb des Q-Werts abzüglich der Masse des sterilen Neutrinos befindet. Da KATRIN für eine Messung der Neutrinomasse im Sub-eV-

Bereich optimiert ist, erfordert die Suche nach sterilen Neutrinos mit keV-Massen zusätzliche Strategien, um die hohe Zählrate in den sensitiven Teilen des Spektrums zu verarbeiten und und um systematische Unsicherheiten zu eliminieren, welche aufgrund des zu erwartenden kleinen Mischungswinkels (astrophysikalische Grenze $\sin^2\theta \lesssim 10^{-7}$) kritisch sind. Daher wird die Idee der MAC-E-TOF-Spektroskopie auch auf das Szenario von sterilen Neutrinos mit keV Massen angewendet. Das würde insbesondere dazu beitragen, die systematische Unsicherheit zu unterdrücken und das Signal-Untergrund-Verhältnis zu verbessern, indem die Teile des β-Spektrums mit höheren Energien und ohne sterile Neutrino-Information vom Rest unterschieden werden können. Die Sensitivität des Flugzeitmodus auf sterile Neutrinos mit keV-Massen wurde durch Monte Carlo-Simulationen bestimmt. Um die Sensitivität aus einem Modell zu gewinnen, ohne die volle Statistik von bis zu $\sim 10^{18}$ Ereignissen zu sampeln, wurde eine Variante des Importance Samplings, genannt *Self-consistent Importance Sampling* (SCIS) entwickelt und angewendet. Die Simulation zeigen, dass ein idealer Flugzeitmodus imstande wäre, die statistische Sensitivität auf $\sin^2\theta$ um fast eine halbe Größenordnung anzuheben. Falls zusätzlich eine exemplarische systematische Unsicherheit im Form einer unbekannten Säulendichte in der Tritiumquelle mit berücksichtigt wird, welche die inelastische Streuwahrscheinlichkeit beeinflusst, wächst der Verbesserungsfaktor um mehr als eine Größenordnung an. Darüberhinaus wurde die Umsetzung der Flugzeitmessung mittels Gated Filtering simuliert. Es wird gezeigt, dass diese Methode im Falle der einfachstmöglichen Umsetzung nicht besser als der integrierende Modus ist. Allerdings sind weitere Optimierungen des Detektors und der Zeitparameter möglich, welche die Leistung weiter verbessern könnten.

3. Zusätzlich zur sterilen Neutrino-Hypothese haben auch gewisse Modelle mit Neutrino-Wechselwirkungen jenseits des Standardmodells Einflüsse auf das Tritium β-Spektrum. Ein Beispiel sind schwache Non-$V-A$-Beiträge, auch als rechtshändige Ströme bezeichnet. Diese können etwa durch rechtshändige W-Bosonen im Left-Right Symmetric Model (LRSM) vermittelt werden. In dieser Erweiterung des SM wird eine zusätzliche $SU(2)_R$-Symmetrie eingeführt, welche auf natürliche Weise sterile Neutrinos beinhaltet und den Seesaw-Mechanismus vorhersagt. Im Tritium β-Zerfall führt das zu einem zusätzlichen Interferenzterm zwischen links- und rechtshändigen Wechselwirkungen, welcher bestimmte Regionen nahe des Endpunkts im β-Spektrum unterdrückt oder verstärkt. Die Sensitivität von KATRIN auf rechtshändige Ströme wird für das Szenario eines leichten sterilen Neutrinos mit einer Masse von einigen eV bestimmt. Dies wurde mit einer Bayes'schen Analyse mithilfe des Markov Chain Monte Carlo (MCMC)-Verfahrens durchgeführt. Die Simulationsergebnisse zeigen, dass KATRIN prinzipiell in der Lage ist, Limits auf die Interferenzstärke als Funktion der sterilen Neutrinomasse zu setzen. Die Sensitivität ist deutlich erhöht, falls der Q-Wert des Tritium-β-Zerfalls genügend eingegrenzt werden kann. Allerdings ist die Sensitivität nicht hoch genug, um derzeitige obere Grenzen von rechtshändigen W-Boson-Suchen am LHC zu übertreffen.

Preface

The aim of this thesis is to explore some of the prospects to improve the KATRIN sensitivity to the absolute neutrino mass scale and to extend it to other phenomena beyond the Standard Model in the neutrino sector.

Chapter 1 will provide an introduction into neutrino physics, including a brief outline of the history and the current research issues, the physics of massive neutrinos, the methods of measuring the neutrino mass and the hypothesis of sterile neutrinos. **Chapter 2** is a short overview over the KATRIN experiment, its basic principles, its components and the analysis strategy. In **Chapter 3** the idea of measuring the neutrino mass by a new time-of-flight mode is discussed and simulation results are presented. Two measurement methods and their implications are investigated. The model used to simulate the time-of-flight is compared with measurements from the KATRIN commissioning runs SDS I and II. **Chapter 4** deals with the KATRIN sensitivity to keV sterile neutrinos, which are candidates for warm dark matter. Again, the idea of a time-of-flight mode is investigated in order adapt KATRIN to the additional systematics at lower retarding potentials. For the simulations, a dedicated sensitivity estimation method based on importance sampling has been employed. In **Chapter 5** the sensitivity of KATRIN to right-handed currents in presence of eV scale sterile neutrinos is investigated, with a detailed discussion of the signature of such a phenomenon and a sensitivity simulation performed by Markov Chain Monte Carlo (MCMC) method. Finally, **Chapter 6** places the findings into further context and gives an outlook on future studies on the issues.
The results of chapter 3 have already been published [Ste+13], while the results of chapter 5 have been accepted for publication [Ste+17b], and those of chapter 4 are currently prepared for publication. The respective chapters are based on the original drafts of these publications and have been edited for consistency, especially with regards to the mathematical definitions, and to ensure a coherent reading experience. Regarding those papers with independent contributions from co-authors, I guarantee that the parts adopted in this thesis have all been written originally by myself.

All equations, e.g., decay spectra and Lagrangians, follow the convention of natural units, $\hbar = c = 1$. All particle masses are therefore given in eV.

Contents

Chapter 1

Neutrino Physics

1.1 History and Research Overview

Despite being proposed already in 1930 by Pauli [Pau30] to guarantee energy conservation in β-decay and experimentally verified in the 1950s in the Cowan Reines experiment [Cow+56], neutrinos still pose fundamental unanswered questions. It was long unclear if neutrinos are massless or have at least a small mass. In 1957, Pontecorvo considered the possibility of neutrino oscillations between neutrinos and antineutrinos [Pon57]. While this could never be experimentally observed, it laid the groundwork for a later, more elaborated theory of oscillation between at least two flavor states ν_e and ν_μ, in case neutrinos are massive [MNS62]. Meanwhile, in the same year, the Goldhaber experiment [GGS58] showed that neutrinos have only left-handed helicity[1]. The muon neutrino ν_μ was finally detected in 1962 at the Brookhaven National Laboratory [Dan+62]. With the tau neutrino ν_τ, which was detected in 2000 at the DONUT experiment [Kod+01], three generations of neutrinos are known today.

The neutrino oscillation hypothesis gained some popularity in the context of the *solar neutrino problem*. In the late sixties at the Homestake experiment [Cle+98], solar neutrinos could be detected for the first time, but the flux was three times less then expected. The tension could be resolved if electron neutrinos are converted into other flavors. However, for a long time, experiments were only able to find upper limits for massive neutrinos. The standard model of particle physics has therefore been built on the premise that there are no neutrinos with right-handed chirality[2] and thus no Dirac-mass term, which would mean that the neutrino mass is zero. However, the successful discovery of neutrino oscillations at the SuperKamiokande experiment in 1998 [Fuk+98] and the SNO experiment in 2001 [Ahm+01] finally allowed no other conclusion other than neutrinos are massive. This also solved the solar neutrino problem, where the deficit was explained by the combination of vacuum oscillations and resonantly enhanced oscillations in the sun (MSW effect [Wol78; MS85]).

Thanks to a large number of oscillation experiments with neutrinos from different sources (reactor, oscillator, atmosphere, sun), the squared mass differences between the mass states and the mixing angles between the mass and flavour states are well known nowadays. Still, as the standard model neutrino theory has been falsified, there are many unsolved issues connected with the quest for a fundamental neutrino theory beyond the standard model. Obviously, the **absolute neutrino mass scale** is one of the most crucial questions, which can not be solved by oscillation experiments (section 1.4). The current upper limit on the neutrino mass comes from the β-decay experiments in Mainz [Kra+05]

[1] which is the projection of the spin on the momentum of the particle
[2] which is identical to the helicity in case of a massless particle

and Troitsk [Ase+11] with $m(\nu_e) \lesssim 2\,\text{eV}$ [3]. The KATRIN experiment [KAT04], which is planned to start data-taking in the end of 2017, aims to improve the sensitivity by one order of magnitude and will be discussed in detail in chapter 2. Another unsolved problem is the **neutrino mass hierarchy**, where the current knowledge allows either a normal hierarchy of the mass states $m_1 < m_2 < m_3$ or an inverted hierarchy $m_3 < m_1 < m_2$ (section 1.3.3).[4] This will hopefully be solved in the next years with new dedicated oscillation experiments such as NOνA [Ayr+05] and HyperKamiokande [Abe+16]. Furthermore unknown is the magnitude of the **CP violation** of neutrino oscillation, which can possibly be answered by next-generation oscillation experiments. As well, it is unclear if neutrinos are **Majorana particles**, in which case they would be identical with their antiparticles. This is studied via the search for neutrinoless double β-decay ($0\nu\beta\beta$) with experiments such as GERDA [Ago+17] (section 1.4.2).

Closely related with the neutrino mass and the Majorana or Dirac nature of the neutrinos is the search for **sterile neutrinos** (section 1.5), which have right-handed chirality and thus do not take part in weak interactions. With the discovery of massive neutrinos, the Standard Model view that there are only neutrinos with left-handed chirality (*active* neutrinos) has been taken into doubt. Depending on their mass, the assumption of sterile neutrinos can lead to useful predictions, such as warm dark matter (WDM) (section 1.5.3), leptogenesis (section 1.5.4) or the solution of short baseline oscillation anomalies (section 1.5.2). Sterile neutrinos also play a critical role in the neutrino **mass generation mechanism** due to their mixing with active neutrinos (section 1.3.4). To study the mass generation mechanism, finally, is a crucial steps towards a **new fundamental theory** beyond the standard model.

1.2 Standard Model Neutrinos

Despite the evidences for physics beyond, the Standard Model (SM) is still empirically valid as the current effective fundamental theory of particle physics. As a quantum field theory, all known fundamental particles are results of a canonical quantization of underlying fields, which follow certain symmetries. In this picture, matter is composed of spin 1/2-fermions while the interactions between them are carried out by spin 1-bosons. The fermions can be grouped into quarks (*up*- and *down*-type, respectively) and leptons (charged ones and electrically neutral *neutrinos*). For each of them, there exists also a corresponding antiparticle.[5] The number of gauge bosons is determined by the generators of the *gauge group* they correspond to. The number of fermions is not a priori limited, yet the decay width of the Z^0-resonance [Abr+91] suggests that for each of type of fermion there are exactly three generations.

The interactions result from an $SU(3)_C \times SU(2)_L \times U(1)_Y$ gauge invariance of the *Lagrangian* $\mathcal{L}$. The SU(3) group describes the strong interaction mediated by 8 different gluons. These can only couple to themselves and the quarks which have one of three different color charge states C (plus three anti-color states for the anti-quarks) each. $SU(2)_L$ and $SU(1)_Y$ together form the electroweak interaction where the $SU(2)_L$ is represented by the weak isospin I_3, mediated by the three W bosons W^+, W^- and W^0 and the $U(1)_Y$ by the weak hypercharge $Y = 2(Q - I_3)$, mediated by the B^0 boson. Due to the maximal parity violation of the weak interaction, which was detected in the Wu experiment [Wu+57], the

[3] See chapter 2.1.1 for the definition of the electron neutrino mass.

[4] It is known from the MSW effect on solar neutrinos (section 1.3.2) that $m_1 < m_2$.

[5] However, if neutrinos are Majorana particles, they are identical with their antiparticles.

weak bosons of the $SU(2)_L$ couple only to particles with left-handed chirality, explaining the subscript L.[6]

All masses are generated by the Higgs Mechanism. This introduces a SU(2) doublet field $\varphi = (\varphi^+, \varphi^0)$, whose potential has a non-zero vacuum expectation value v. Thus, the electroweak $SU(2)_L \times U(1)_Y$ symmetry is broken to the weak SU(2) and electromagnetic U(1) symmetry. In this process, some bosons and fermions get masses by coupling to the Higgs field. The fundamental B^0 and W^0 bosons superpose to the Z^0 bosons and the photon γ. After the transformation, one degree of freedom of the Higgs field remains, corresponding to the Higgs particle, which is a scalar with spin 0. The Higgs particle is the latest verified standard model particle, which has been discovered in 2012 at the LHC [ATL12; CMS12]. To summarize, all elementary particles postulated by the Standard Model are shown in fig. 1.1.

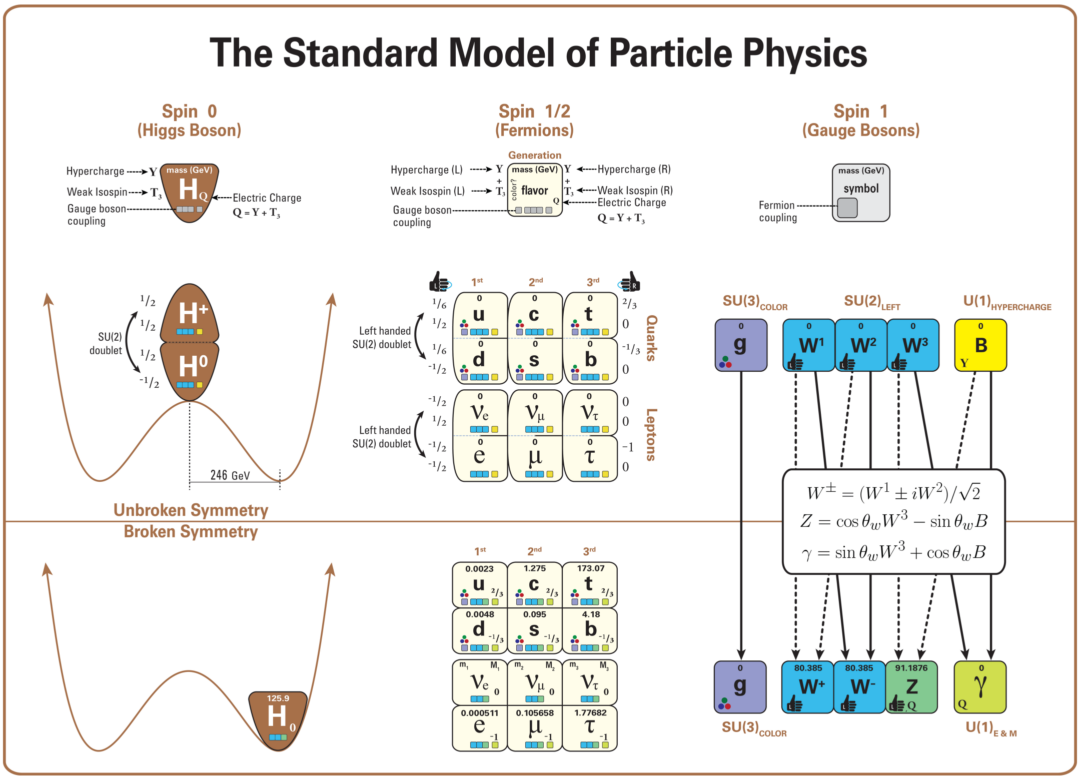

Figure 1.1: Particle content of the standard model. Figure from [Boy14]

As the following sections focus on the physics of neutrinos, their properties as standard model particles shall be recapitulated briefly. Neutrinos belong to the leptons and have no electric charge, thus they interact only weakly. They carry a weak isospin of $I_3 = 1/2$. There is one neutrino for each fermion generation, thus there exist three neutrinos ν_e, ν_μ, ν_τ. They carry a lepton number of $L = 1$ and a lepton family number of $l_\alpha = 1$, corresponding to their generation $\alpha = e, \mu, \tau$. For anti-neutrinos, it amounts to $L = -1$ and $l_\alpha = -1$, respectively. In the original Standard Model without neutrino oscillations, both lepton number and lepton family number are conserved.

[6] That means that they are eigenvalues of the left-handed chirality projection operator $P_L = \frac{1}{2}(1-\gamma_5)$, where γ_5 is one of the Dirac matrices. In the relativistic limit, the chirality coincides with the helicity, which is the projection of the spin on the momentum direction.

1.3 Massive Neutrinos

1.3.1 Solar Neutrino Problem and Discovery of Neutrino Oscillations

The discovery of neutrino oscillations and the consequential violation of lepton family number conservation has shown that there is physics beyond the standard model in the neutrino sector. First experimental hints for neutrino oscillations were found with the Homestake experiment [Cle+98] which became known as the *solar neutrino problem* (SNP). Solar neutrinos were detected by capture on chlorine, leading to transformation into argon,

$$^{37}\mathrm{Cl} + \nu_e \rightarrow {}^{37}\mathrm{Ar} + e^- . \tag{1.1}$$

The measured flux was significantly lower than expected from the solar standard model [BSB05]. The discrepancy could be confirmed by other solar neutrino experiments such as GALLEX [Ham+99], SAGE [Abd+02] and GNO [Alt+05].

The crucial step towards the solution of the problem have been the discoveries of neutrino oscillation with Super-Kamiokande [Fuk+98] and SNO [Ahm+01]. Super-Kamiokande detected neutrinos by measuring Cherenkov radiation emitted from relativistic electrons within a large water tank, after elastic scattering (ES) reactions on electrons,

$$\nu_\alpha + e^- \rightarrow \nu_\alpha + e^- \qquad \text{(ES)} . \tag{1.2}$$

This reaction is foremost sensitive to ν_e but partly also to ν_μ. It is only relevant for solar neutrinos, which have energies mostly below $\mathcal{O}$(MeV). Atmospheric neutrinos with higher energies can be detected in quasi-elastic and deep-inelastic charged current reactions on hydrogen and oxygen nuclei,

$$\bar{\nu}_\alpha + p \rightarrow l_\alpha^+ + n \tag{1.3}$$
$$\nu_\alpha + n \rightarrow l_\alpha^- + p \tag{1.4}$$
$$\tag{1.5}$$

where an (anti-)lepton $l_\alpha^{+/-}$ of the same generation α as the (anti-)neutrino $\overset{(-)}{\nu}_\alpha$ is produced. In the deep-inelastic case a hadronic shower is produced in addition to the lepton. Given the energies of atmospheric neutrinos, these reactions are sensitive on ν_e and ν_μ. The results showed a deficit of the expected atmospheric ν_μ flux from the downward hemisphere. This was consistent with oscillations of ν_μ into ν_τ.

The SNO experiment, in contrast, used deuterium as target and was thus sensitive to all three neutrino flavors by the additional neutral current (NC) and charged current (CC) reactions,

$$\nu_e + d \rightarrow e^- + p + p \qquad \text{(CC)} \tag{1.6}$$
$$\nu_\alpha + d \rightarrow \nu_\alpha + p + n \qquad \text{(NC)} . \tag{1.7}$$

In case of solar neutrinos, the CC reaction is only allowed for ν_e, since the neutrino energy is not sufficient to produce a muon, while the NC reaction is allowed for all three neutrinos flavors. With the NC channel measuring the total flux of neutrinos and the CC channel measuring the ν_e flux separately, SNO was therefore successful in confirming oscillations of solar neutrinos for the first time, laying the groundwork towards the resolution of the solar neutrino problem.

1.3.2 Neutrino Oscillation Theory

The idea of neutrino oscillation has first been proposed by Pontecorvo [Pon57] and later been refined by Maki, Nakagawa, and Sakata in 1962 [MNS62]. The theoretical fundament is a non-trivial mixing between the flavor eigenstates (ν_e, ν_μ, ν_τ) and three different mass eigenstates (ν_1, ν_2, ν_3) of the neutrinos, where at least one is required to have a mass eigenvalue $m_i > 0$, which furthermore needs to be different from the other mass states. The mechanism has similarities to the quark mixing in the standard model and can be described by a unitary 3×3 matrix, the *Pontecorvo–Maki–Nakagawa–Sakata* (PMNS) matrix,

$$\begin{pmatrix} \nu_e \\ \nu_\mu \\ \nu_\tau \end{pmatrix} = U \begin{pmatrix} \nu_1 \\ \nu_2 \\ \nu_3 \end{pmatrix} = U_{\mathrm{PMNS}} \cdot D_{\mathrm{M}} \begin{pmatrix} \nu_1 \\ \nu_2 \\ \nu_3 \end{pmatrix} \tag{1.8}$$

with

$$U_{\mathrm{PMNS}} = \begin{pmatrix} c_{12}c_{13} & s_{12}c_{13} & s_{13}\,\mathrm{e}^{-\delta_{13}} \\ -s_{12}c_{23} - c_{12}s_{23}s_{13}\,\mathrm{e}^{\mathrm{i}\delta_{13}} & c_{12}c_{23} - s_{12}s_{23}s_{13}\,\mathrm{e}^{\mathrm{i}\delta_{13}} & s_{23}c_{13} \\ s_{12}c_{23} - c_{12}c_{23}s_{13}\,\mathrm{e}^{\mathrm{i}\delta_{13}} & -c_{12}s_{23} - s_{12}c_{23}s_{13}\,\mathrm{e}^{\mathrm{i}\delta_{13}} & c_{23}c_{13} \end{pmatrix} \tag{1.9}$$

and

$$D_{\mathrm{M}} = \begin{pmatrix} 1 & 0 & 0 \\ 0 & \mathrm{e}^{\mathrm{i}\lambda_2} & 0 \\ 0 & 0 & \mathrm{e}^{\mathrm{i}\lambda_3} \end{pmatrix}. \tag{1.10}$$

Here, s_{ij} and c_{ij} stand for $\sin\theta_{ij}$ and $\cos\theta_{ij}$, where θ_{ij} are three mixing angles. The diagonal matrix D_M contains two Majorana phases and is different from unity if neutrinos are Majorana particles, i.e. identical to their own antiparticles. δ_{13} is a Dirac phase and is $\neq 0$ if neutrino oscillation violates CP conservation. If neutrinos are produced in weak interaction, they are in a well-defined flavor eigenstate, which is itself a superposition of the three mass eigenstates. Applying the time-dependent Schrödinger equation on this state gives different frequencies of the phase evolution for each mass eigenstate contribution, if the mass eigenvalues m_i are slightly different. Therefore, there is a non-zero probability of detecting the neutrino in a different flavor state than it was created, after propagating a certain distance L.

Using a plane-wave ansatz, the appearance probability for flavor β, given initial flavor α, can be approximated by

$$P_{\nu_\alpha \to \nu_\beta} = \sum_{k,j} U^*_{\alpha k} U_{\beta k} U_{\alpha j} U^*_{\beta j} \exp\left(-\mathrm{i}\frac{|\Delta m^2_{kj}| L}{2E}\right), \tag{1.11}$$

where $\Delta m^2_{kj} = m^2_k - m^2_j$ is the squared mass difference between the mass eigenstates k and j [MP04]. The complex exponential function gives rise to an oscillation of the appearance probability with an *oscillation length* of

$$L_{\mathrm{osc}} = \frac{4\pi E}{|\Delta m^2_{ij}|}. \tag{1.12}$$

The formula gets more complicated for the full consideration of all three generations and includes combination of multiple mass differences Δm^2_{kj}. However, for oscillations from a well-defined initial flavor state, usually one mass difference dominates.

MSW Effect

In addition to the vacuum oscillation described by eq. (1.11), there are resonantly enhanced neutrino oscillations, also known as *Mikheyev–Smirnov–Wolfenstein (MSW) effect* [Wol78; MS85]. The effect is caused by the circumstance that ν_e can interact with electrons both via charged currents and neutral currents, while ν_μ and ν_τ can only interact with electrons via neutral currents. This gives rise to effective mass states and mixing angles which are different from those in vacuum. For a given electron density, the effective mixing reaches a maximum. If a ν_e is produced in a region of higher electron density than in the resonance case and if it propagates under adiabatic conditions (i.e. sufficiently slow changes of the density) into a region with lower density, there is a high chances that it is converted into a different flavor. Thus, the MSW effect has been successful in explaining the solar neutrino problem, since such conditions are met in the sun. Global fits of oscillation data favor the *LMA (large mixing angle)* solution with $\theta_{12} \approx 34°$, leading to a survival probability $P_{ee} = \sin(2\theta_{12}) \approx 34\,\%$ at $\sim$ MeV neutrino energies [BGP02; FL04]. Since the MSW effect does only work if m_1 is not the heaviest state, the results determine that $m_1 < m_2$.

1.3.3 Oscillation Parameters

A number of neutrino oscillation experiments since the first positive Super-Kamiokande results have been able to complete the current knowledge about the neutrino oscillation parameters. Each type of experiment uses a different neutrino source and a different *baseline* (distance between detector and source) and is thus sensitive to different parameters. Combining these single results gives a coherent global picture of neutrino oscillation. As of today, three mixing angles (θ_{12}, θ_{23} and θ_{13}) and two mass differences (Δm^2_{12} and Δm^2_{23}) are known. The most recent addition has been the mixing angle θ_{13}, which was measured in 2012 by Daya Bay [An+12] and other experiments. There are basically four types of experiments.

Atmospheric neutrino experiments detect ν_μ and ν_e (plus anti-neutrinos), created in collisions of cosmic rays with the earth's atmosphere. These are produced with a ratio of $\nu_\mu : \nu_e \simeq \bar{\nu}_\mu : \bar{\nu}_e \gtrsim 2 : 1$ and have energies from some MeV up to the TeV scale. Experiments are mostly sensitive to $\Delta m^2_{23} := m^2_{\mathrm{atm}}$ and θ_{23}. The most wide-known example is SuperKamiokande [Fuk+98].

Solar neutrino experiments detect ν_e, created in solar fusion processes with energies up to some MeV as predicted by the Solar Standard Model [BSB05]. They are mostly sensitive to $\Delta m^2_{12} := m^2_{\mathrm{sol}}$ and θ_{12}. Examples are the already mentioned Homestake experiment [Cle+98], GALLEX [Ham+99], SAGE [Abd+02] and SNO [Ahm+01].

Accelerator neutrino experiments detect highly energetic $\overset{(-)}{\nu}_\mu$ at the GeV scale, produced in a particle accelerator and focused on a detector at a long baseline of some 100 – 1000 km. These are sensitive alternatives to atmospheric neutrino experiments when it comes to measure Δm^2_{23} and θ_{23}, but also θ_{13}. Examples are T2K [Abe+11] and MINOS [Ada+11].

Reactor neutrino experiments use the flux of $\bar{\nu}_e$, emitted in β-decays of fission products in nuclear reactors, to measure θ_{13}. The neutrinos have energies similar to solar neutrinos of up to some MeV and the baseline is usually in the order of some km. Examples are KamLAND [Egu+03], DayaBay [An+12], Reno [Seo16] and DoubleChooz [Las16].

parameter	best fit value	3σ region
Δm^2_{21} (eV^2)	7.4×10^{-5}	$6.9 \times 10^{-5} - 8.0 \times 10^{-5}$
$\lvert\Delta m^2_{23}\rvert$ (eV^2)	2.5×10^{-3}	$2.4 \times 10^{-3} - 2.6 \times 10^{-3}$
$\sin^2\theta_{12}$	0.30	$0.25 - 0.35$
$\sin^2\theta_{23}$	0.50	$0.38 - 0.63$
$\sin^2\theta_{13}$	0.022	$0.019 - 0.025$

Table 1.1: Global best fit values and 3σ regions for squared mass differences and mixing angles. Values from [Pat+16] (averaged for normal and inverted hierarchy).

The current results from a global fit of all oscillation experiments are shown in table 1.1 and fig. 1.2. Regarding the CP violation phase δ_{13}, there has been no definitive result yet, however $\delta_{13} = 0$ is disfavored at 2σ confidence level [Pat+16]. As the sign of Δm^2_{23} is still unknown, there are two different mass ordering scenarios compatible with the parameters. Either a *normal hierarchy* with $m_1 < m_2 \ll m_3$ or an *inverted hierarchy* with $m_3 \ll m_1 < m_2$ is possible. This can in principle either be solved by using the matter enhanced oscillation inside the earth (as e.g. in the NOvA experiment [Ayr+05]) or by measuring the small difference between Δm^2_{13} and Δm^2_{23} in next-generation oscillation experiments [QV15]. Furthermore, one distinguishes between a *quasi-degenerate* scheme, where $m_1 \approx m_2 \approx m_3$, as opposed to a *hierarchical* mass scheme, where the mass differences are significantly larger than the lightest neutrino mass, $\Delta m^2_{kj} > m^2_{\mathrm{min}}$. If the absolute mass scale is sufficiently large, the mass splittings become negligible, which is called a *quasi-degenerate* scenario. An illustration of the possible mass scenarios is shown in fig. 1.3.

1.3.4 Neutrino Mass Generation

The evidence for non-zero neutrino masses requires the Standard Model to be extended by a mass-generation mechanism for the neutrinos. In the SM Lagrangian there is no right handed chiral neutrino singlet, in contrast to the other fermions. This naturally leads to a neutrino with zero mass and only left handed helicity. In order to account for a non-vanishing neutrino mass, the most simple extension would be to include a right handed neutrino singlet *ad hoc* and to add a Yukawa interaction term between left-handed neutrino doublet, Higgs doublet and right-handed singlet. Considering only one generation, this would be written as

$$\mathcal{L}_{\mathrm{mass,D}} = \mathcal{L}_{\mathrm{mass,SM}} - y_\nu(\bar{\nu}, \bar{\mathrm{e}})_{\mathrm{L}} \begin{pmatrix} \varphi^+ \\ \varphi^0 \end{pmatrix}^C \nu_{\mathrm{R}} + \mathrm{h.\,c.}\,, \tag{1.13}$$

where y_ν is a Yukawa coupling constant and the superscript C stands for charge-conjugation. This is a pure *Dirac mass* term. Expanding around the Higgs vacuum expectation value (VEV) v and applying a local U(1) gauge transformation yields

$$\mathcal{L}_{\mathrm{mass,D}} = \mathcal{L}_{\mathrm{mass,SM}} - m_\nu \bar{\nu}_{\mathrm{L}} \nu_{\mathrm{R}} + \mathrm{h.\,c.}\,, \tag{1.14}$$

where

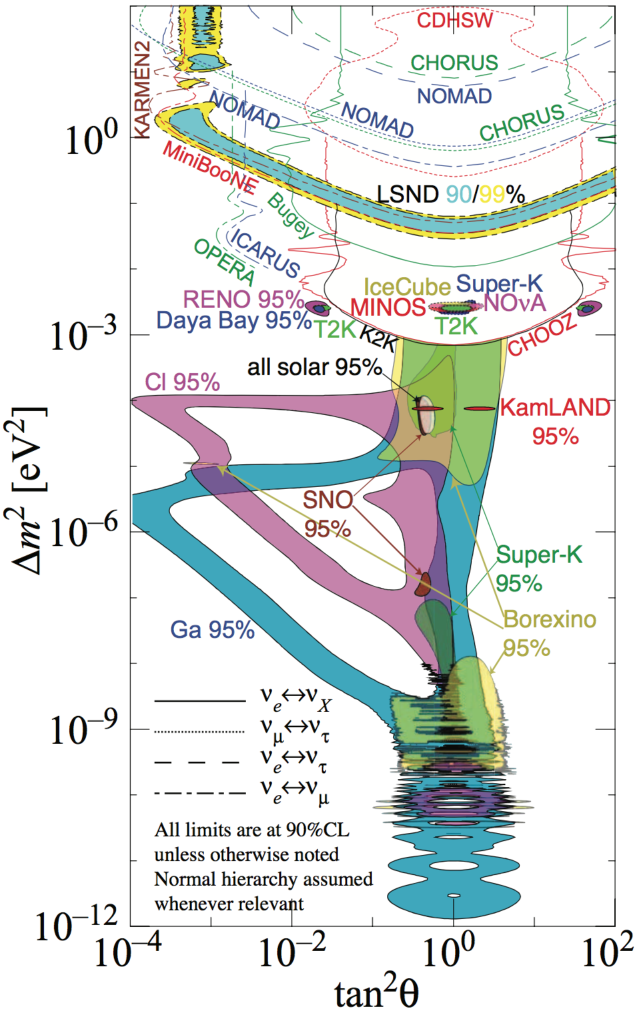

Figure 1.2: Overlay of results from the oscillation experiments for atmospheric, solar and reactor neutrinos. Figure adopted from [Pat+16], courtesy of H. Murayama [Mur14].

$$m_\nu = \frac{y_\nu \cdot v}{\sqrt{2}} \,. \tag{1.15}$$

However, due to the smallness of the neutrino mass, the Yukawa coupling constants for the neutrinos y_ν would have to be several orders of magnitude smaller compared to those for the other fermions, which are nearly equal. A more natural result is achieved by addition of *Majorana mass* terms. Any implementation of such terms lead to the consequence that neutrino and antineutrino are identical and thus violate lepton number conservation. A Lagrangian that combines Dirac and Majorana mass terms can be written in matrix form after U(1) symmetry breaking,

$$2\mathcal{L}_{\mathrm{mass,D+M}} = \mathcal{L}_{\mathrm{mass,SM}} - (\bar{\nu}_\mathrm{L}, (\bar{\nu}_\mathrm{R})^C) \begin{pmatrix} m_\mathrm{L} & m_\mathrm{D} \\ m_\mathrm{D} & m_\mathrm{R} \end{pmatrix} \begin{pmatrix} (\nu_\mathrm{L})^C \\ \nu_\mathrm{R} \end{pmatrix} . \tag{1.16}$$

The matrix can be diagonalized with the two eigenvalues m_1 and m_2. For the special case of $m_\mathrm{L} = 0$, that gives

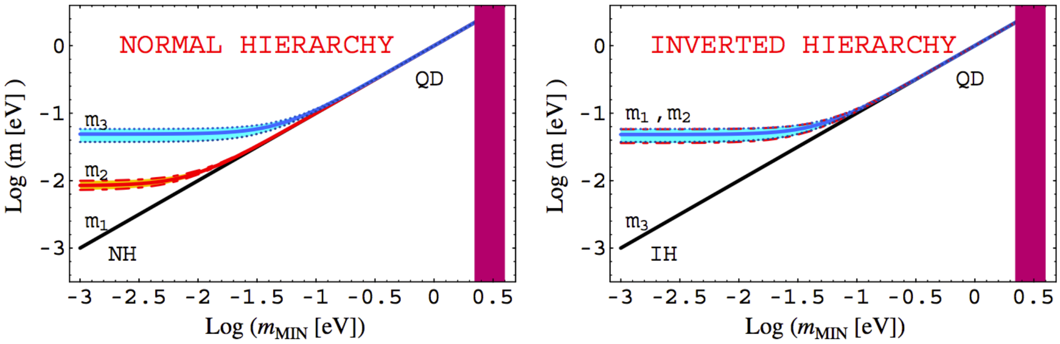

Figure 1.3: Magnitude of neutrino mass states as function of the smallest mass state for both normal and inverted hierarchy scenarios, compatible with the current mass differences obtained from oscillation experiments. *QD* stands for the *quasi-degenerate* region, where the mass differences are small relative to the absolute mass scale. Figure from [Moh+07].

$$m_1 = \frac{m_{\mathrm{D}}^2}{m_{\mathrm{R}}} \qquad m_2 = m_{\mathrm{R}}\ . \tag{1.17}$$

This is a *seesaw mechanism type I* [MP04]. If m_1 is low, then m_2 becomes high and vice versa. The model is able to explain why the observable neutrino masses are significantly lower than the other fermion masses of the same generation, while still keeping the Yukawa couplings for all fermions at the same scale. In the standard approach, one would expect m_{D} to be close to the other fermion masses and m_{R} to be at the GUT scale ($\sim 10^{10}$ GeV – 10^{15} GeV). As this simplified picture deals with only one generation, m_1 becomes the mass of the *active* neutrino state while m_2 is then the mass of the *sterile* neutrino state. This formalism can be extended to three active neutrino generations. The mass matrix then has the dimension $(3+N)\times(3+N)$, where N is the number of right-handed neutrino singlets.

In a minimal extension, one would expect m_{L} to be zero, since the corresponding mass term violates weak isospin and is forbidden in standard model. However, by adding a five-dimensional operator such as a Higgs triplet [KK77], $m_{\mathrm{L}} > 0$ becomes allowed. For sufficiently high m_{L}, one obtains a *type II seesaw*. A Higgs triplet is proposed in some extensions of the Standard Model, e.g. in grand unified theories (GUTs) or the left-right symmetric model (LRSM, section 1.5.5). In many cases, that type of seesaw favorably leads to a quasi-degenerate neutrino mass scheme [DBM12].

1.3.5 Cosmic Neutrinos

The absolute neutrino mass scale plays a crucial role in cosmology. *Relic neutrinos* from the early universe may contribute to a significant part of the energy density in the universe Ω_{tot}. This *cosmic neutrino background* (CνB) has been created at a freeze-out temperature $T_\nu \approx 1$ MeV, when the interaction rate of neutrinos $\Gamma_\nu(T)$ became smaller than the Hubble expansion rate $H(T)$ and therefore the neutrinos decoupled out of thermal equilibrium. The temperature of the CνB as of today is linked to the temperature of the cosmic microwave background (CMB) by

$$T_\nu^0 = (11/4)^{1/3}\, T_\gamma^0 \ = 1.9\,\mathrm{K}, \tag{1.18}$$

which is due to the reheating of the photon gas after the e^+-e^- annihilation at T =

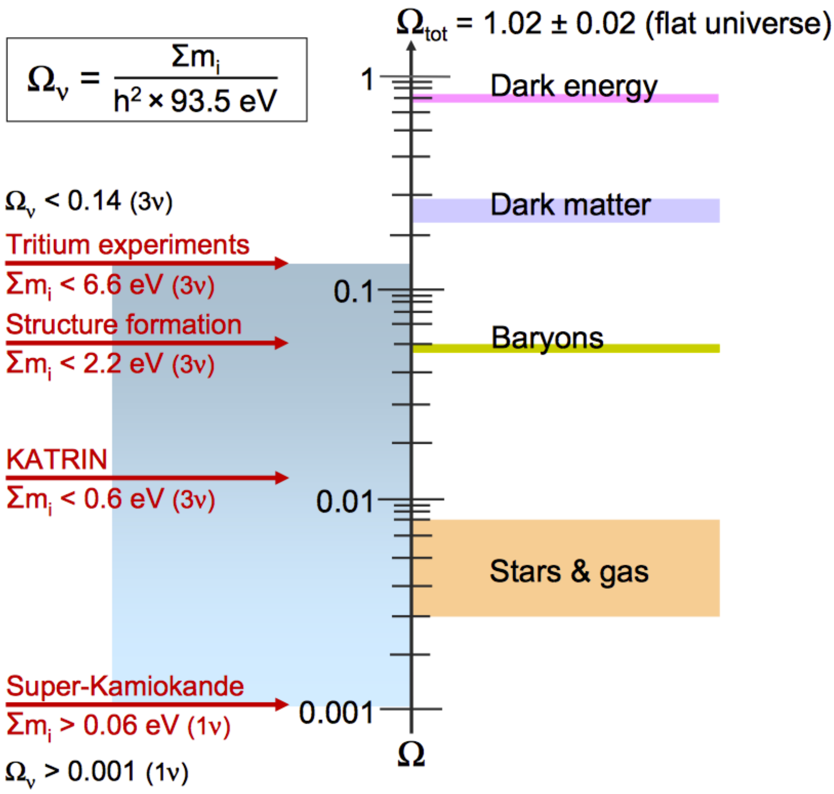

Figure 1.4: Contribution of neutrino energy density Ω_ν to the total energy density of the universe Ω_{tot} as a function of the sum of the neutrino mass states $\sum m_i$. Figure from [KAT04]

1/2 MeV [MP04], where the CMB temperature $T_\gamma^0 = 2.725\,\text{K}$ [Fix09] has been inserted. Likewise, the number densities of photons and neutrinos are linked via

$$n_\nu^0 = \frac{3}{4}\frac{g_\nu}{g_\gamma}\left(\frac{T_\nu^0}{T_\gamma^0}\right)^3 n_\gamma^0 = 336\,\text{cm}^{-3}, \tag{1.19}$$

where the factor 3/4 stems from different statistics for fermions and bosons and the factor $g_\nu/g_\gamma = 6/2$ is given by the ratio of relativistic degrees of freedom for neutrinos and photos. The number density of relic photons, $n_\gamma^0 = 411\,\text{cm}^{-3}$, can be derived from Planck's law, given the CMB temperature. The energy density of neutrinos in terms of the critical density, $\rho_c = h^2 \cdot 1.05 \times 10^4 \text{eV}/\text{cm}^3$, is then given via the number density and sum of all three mass states,

$$\Omega_\nu = \frac{\rho_\nu}{\rho_c} = \frac{\langle m_\nu \rangle\, n_\nu^0}{\rho_c} = \frac{\sum_i m_i n_\nu^0}{3\rho_c} = \frac{\sum_i m_i}{93.14\, h^2\ \text{eV}}, \tag{1.20}$$

with the dimensionless Hubble parameter $h = 0.678$ [Ade+16]. Figure 1.4 shows the contribution of neutrinos to the total energy density of the universe as a function of the neutrino mass scale. It can be seen that within the current experimental limits neutrinos contribute possibly to a significant amount of the total energy density. Yet, since the mass is still unknown, the neutrino contribution is not well constrained.

1.4 Neutrino Mass Measurement

As outlined, oscillation experiments are sensitive to the mass splittings but not to the absolute neutrino mass scale. In the last section, particularly two motivations for a measurement of the absolute neutrino mass were given. First, it allows to constrain mass generation models. Especially, via the seesaw relation (1.16), the active neutrino mass is linked to physics beyond the Standard Model. Second, the neutrino mass is significant in cosmology, where it determines the contribution of neutrinos to energy density of the universe. There are mainly three ways to constrain the neutrino mass scale.

1.4.1 Cosmic Structure Formation

As relativistic particles, neutrinos can escape the density fluctuations of cold dark matter and baryons. Therefore, cosmic structures cannot be formed at scales below the free-streaming length,

$$\lambda_{\mathrm{FS}}(z) = 8\frac{1+z}{\sqrt{\Omega_\Lambda + \Omega_{\mathrm{m}}(1+z)^3}}\left(\frac{\mathrm{eV}}{m_\nu}\right) h^{-1}\mathrm{Mpc} \tag{1.21}$$

[LP14], where z denotes the redshift, Ω_Λ the dark energy density fraction and Ω_{m} the matter density fraction. If there is a significant neutrino contribution to dark matter (*Hot Dark Matter*, HDM), structures above the free-streaming scale are created first, whereas smaller structures are created at a later epoch. The most stringent bounds on neutrino masses from cosmology can be derived by combining data from multiple kinds of sources, which include anisotropy of the cosmic microwave background (CMB), baryonic acoustic oscillations (BAO) and large scale structure (LSS) data.[7] However, fits of cosmological datasets are strongly model-dependent and prone to degeneracies and systematics. Therefore, a complementary measurement by lab-based experiments is important for a credible constraint. The most recent cosmological constraints are given by data from the Planck sattelite [Ade+16], which state

$$\sum_i m_i < 0.68\,\mathrm{eV} \qquad \text{(Planck)} \tag{1.22}$$

$$\sum_i m_i < 0.23\,\mathrm{eV} \qquad \text{(Planck+BAO)} \tag{1.23}$$

at 95 % C.L., where the upper result is based on an analysis of Planck data only[8] and the lower result includes external BAO data.

1.4.2 Neutrinoless Double β-Decay

Provided that neutrinos are Majorana particles, constraints on the neutrino mass can be derived from the half-life of isotopes undergoing *neutrinoless double β-decay* ($0\nu\beta\beta$). It is a variant of the double β-decay with neutrino emission ($2\nu\beta\beta$),

$$2\mathrm{n} \rightarrow 2\mathrm{p} + 2\mathrm{e}^- + 2\bar{\nu}_e\ , \tag{1.24}$$

[7] In case of a sufficiently light neutrino mass, neutrinos are still relativistic at the time of the photon decoupling. Therefore, the imprint of massive neutrinos in the CMB consist mainly of effects on the background cosmology and late-time effects such as lensing in the power spectrum [LP14].

[8] using the "TT+lowP" configuration and including lensing

which occurs in even-even isotopes where a single β-decay is forbidden energetically or due to spin coupling, as e.g. in ^{76}Ge. If $\nu_e = \bar{\nu}_e$, there is a chance that no neutrino is emitted,

$$2n \longrightarrow 2p + 2e^- \,, \tag{1.25}$$

which can be viewed in the corresponding Feynman diagram as the two neutrinos annihilating each other (fig. 1.5, right). This requires a helicity-flip of the neutrino, since, though neutrino and anti-neutrino are identical under Majorana nature, the neutrino still needs to be right-handed in order to take part in weak interactions in the role of an anti-neutrino. That is only possible for a non-vanishing neutrino mass, which enters the probability of such an event quadratically. Since the decay energy is carried completely by the electrons in 0νββ, the signature is a peak at the Q value in the summed electron energy spectrum (fig. 1.6). The decay rate of the 0νββ component is given by

$$\Gamma^{0\nu} = G^{0\nu} |M_{\mathrm{nucl}}|^2 m_{\mathrm{ee}}^2 \,, \tag{1.26}$$

where $G^{0\nu}$ is a phase space factor, M_{nucl} the nuclear matrix element and m_{ee}^2 the *effective Majorana neutrino mass*, which is defined as [Wei03]

$$m_{\mathrm{ee}} = \left| \sum_i \mathrm{e}^{\mathrm{i}\alpha_i} |U_{\mathrm{e}i}^2| m_i \right| \,. \tag{1.27}$$

The complex phases α_i are combined from the CP violating and Majorana phases in the neutrino mixing matrix (1.9). Depending on their values, they can possibly give rise to cancellations, which may lead to $m_{\mathrm{ee}} < m_i$. The largest uncertainty in constraining the neutrino mass via 0νββ yet arises from the calculation of the nuclear matrix element M_{nucl}. The most recent bound was published by the GERDA collaboration [Ago+17], which state an upper limit on the half-time of

$$T_{1/2}^{0\nu} < 5.3 \times 10^{25}\,\mathrm{y} \,, \tag{1.28}$$

translating into a neutrino mass bound of

$$m_{\mathrm{ee}} < 0.15 - 0.33\,\mathrm{eV} \,, \tag{1.29}$$

depending on the considered nuclear matrix element.

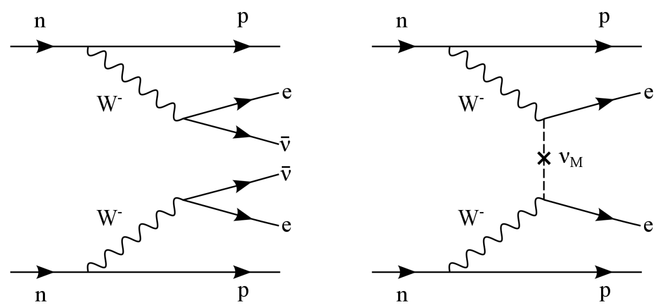

Figure 1.5: Feynman graphs for double β-decay with neutrino emission (2νββ, left) and neutrinoless double β-decay (0νββ, right). Figure from [Erl].

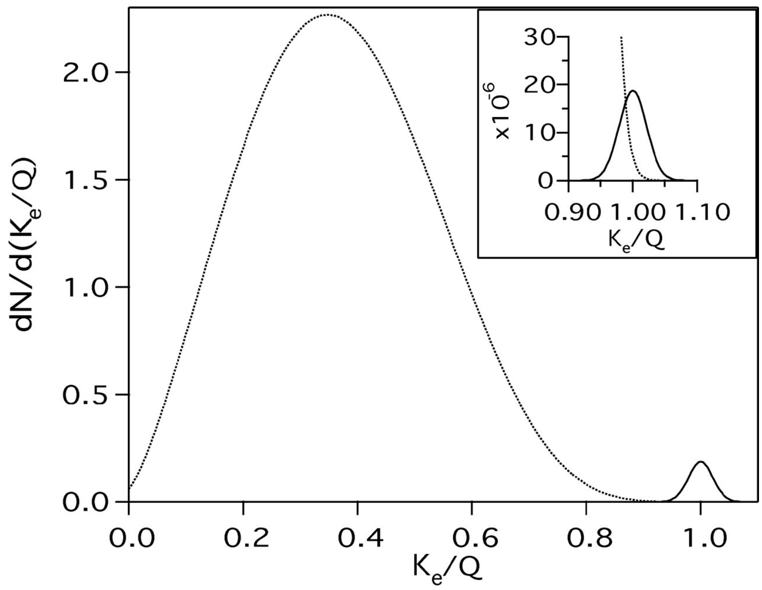

Figure 1.6: Summed electron energy spectrum for $2\nu\beta\beta$ (dotted line) and $0\nu\beta\beta$ (solid line). Figure from [EV02].

1.4.3 Single β-Decay

A theoretically straightforward way to constrain the neutrino mass is to measure the endpoint region of the β-decay spectrum of a suitable isotope. The principle in itself is model-independent, since it is only based on kinematic arguments. A prominent example is the β^- decay

$$n \rightarrow p + e^- + \bar{\nu}_e \; , \tag{1.30}$$

where the available decay energy is shared by the electron and the antineutrino, yielding a continuous kinetic energy spectrum of the electron. The maximum kinetic energy of the electron, called the β *endpoint*, in case of a massless neutrino is determined by Q value,

$$E_0 = E_{\max}(m_\nu = 0) = Q_\beta - E_\mathrm{R} = m_\mathrm{i} - m_\mathrm{f} - m_\mathrm{e} - E_\mathrm{R}, \tag{1.31}$$

where m_i and m_f are the masses of the initial and the final state, respectively, and E_R is the nuclear recoil energy. If, however, the neutrino has a non-zero mass m_ν [9], the maximum kinetic energy is given by

$$E_{\max}(m_\nu > 0) = Q_\beta - E_\mathrm{R} - m_\nu = m_\mathrm{i} - m_\mathrm{f} - m_\mathrm{e} - E_\mathrm{R} - m_\nu \; . \tag{1.32}$$

In order to determine the neutrino mass, the endpoint region of the differential kinetic energy spectrum of the electron (short: *β spectrum*) is measured, which generally can be derived from Fermi's Golden Rule,

$$\frac{\mathrm{d}\Gamma}{\mathrm{d}E}(E) = 2\pi \, |M|^2 \, \rho(E) \; , \tag{1.33}$$

where M is the transition matrix element and $\rho(E)$ the phase space density. A non-vanishing neutrino mass does not only reduce the maximum kinetic energy but also the available phase space near the endpoint, leading to a characteristic imprint well distinguish-

[9]For simplicity, we assume a quasi-degenerate scenario where $m_\nu \approx m_1 \approx m_2 \approx m_3$.

able from the Q value. A general solution for β^- decay can be derived (cf. [OW08; Dre+13]), which, neglecting possible electronic and rotational-vibrational excitations of the daughter isotope or molecule, is given by

$$\begin{aligned} \frac{\mathrm{d}\Gamma}{\mathrm{d}E}(E) &= N\,\frac{G_\mathrm{F}^2}{2\pi^3}\cos^2(\theta_\mathrm{C})\,|M_\mathrm{nucl}(E)|^2\,S(E)\,F(E,Z')\cdot p\cdot(E+m_\mathrm{e}) \\ &\quad\cdot\sum_i |U_{\mathrm{e}i}|^2\cdot(E_0-E)\cdot\sqrt{(E_0-E)^2-m_i^2}\,\Theta(E-E_0-m_i)\,, \end{aligned} \tag{1.34}$$

where N is the number of atoms, G_F the weak coupling constant, θ_C the Cabbibo angle, $M_\mathrm{nucl}(E)$ the nuclear matrix element, $S(E)$ a shape-factor and $F(E,Z')$ the Fermi function, which describes the Coulomb interaction between electron and daughter nucleus. The shape factor accounts for the transport of angular momentum in case of forbidden decays and is $S(E) = 1$ in case of allowed decays. Additionally, the nuclear matrix element is only constant for allowed decays. The phase space density is then given by the product of the electron momentum p, the electron energy $E + m_\mathrm{e}$, the neutrino energy $E_0 - E$ and the neutrino momentum $\sqrt{(E_0-E)^2-m_i^2}$, which is summed incoherently over the mass states m_i via the absolute squares of the mixing matrix elements $|U_{\mathrm{e}i}|^2$. The Heaviside function $\Theta(E-E_0-m_i)$ assures $\mathrm{d}\Gamma/\mathrm{d}E = 0$ for $E > E_0 - m_i$. The decay spectrum will be discussed in detail for the isotope tritium (T) as used in the KATRIN experiment [KAT04] in section 2.1.1 .

Tritium Experiments

Tritium is one of the most common isotopes used for β-decay experiments. The advantages are a relatively low Q value of $Q \approx 18.6\,\mathrm{eV}$, leading to a significant imprint of a massive neutrino in the spectrum, a short half-life of $T_{1/2} \approx 12.3\,\mathrm{y}$, providing a large decay rate and the fact that it is a super-allowed β-decay, where the nuclear matrix element M_nucl is energy-independent and the decay scheme has no intermediate states. Tritium has been used in the Mainz [Kra+05] and Troitsk [Ase+11] experiments, which give the most stringent bounds from lab-based experiments as of today, which state

$$m_{\nu_\mathrm{e}} < 2.3\,\mathrm{eV} \qquad \text{(Mainz)} \tag{1.35}$$

$$m_{\nu_\mathrm{e}} < 2.05\,\mathrm{eV} \qquad \text{(Troitsk)} \tag{1.36}$$

at 95 % C.L. Both experiments used an integrating electromagnetic spectrometer of the *MAC-E-Filter* type (magnetic adiabatic collimation with an electrostatic filter [Pic+92], see section 2.1.2) which measures the kinetic electron energy spectrum in a high pass filter mode by blocking all electrons with kinetic energies below a variable threshold qU. In general, β-decay experiments have the advantage of being model-independent and quite insensitive to systematics, which makes their bounds well reliable.

Cryogenic Bolometers

An alternative variant of β experiments has grown in recent years which utilizes cryogenic bolometers. There, the complete decay energy except that of the neutrino is absorbed by the detector material, leading to a subtle temperature increase, which is transformed into an electric signal. Source, detector and readout are integrated in a compact unit, called *micro-calorimeter*. The advantage of that setup is its high scalability by increasing the number of micro-calorimeter units. Furthermore, the calorimetric principle allows a direct measurement of the differential energy spectrum and avoids some of the systematics of using an external source.

A promising example is the ECHo experiment [Has+16], which uses the decay of holmium (^{163}Ho) into dysprosium (^{163}Dy$*$) via electron capture,

$$^{163}\mathrm{Ho} + \mathrm{e}^- \longrightarrow {}^{163}\mathrm{Dy}^* + \nu_\mathrm{e} \; . \tag{1.37}$$

It has a half-life of $T_{1/2} \approx 4570\,\mathrm{y}$ and a low Q value of $Q \approx 2.8\,\mathrm{keV}$ [Eli+15]. Similar to classic β-decay experiments, a massive neutrino leads to an deficit in the $^{163}\mathrm{Dy}^*$ de-excitation spectrum close to the Q value. ECHo uses low temperature metallic magnetic calorimeters (MMC) with a SQUID readout, yielding an energy resolution of $\approx 2\,\mathrm{eV}$. The next stage with 1000 Bq activity is supposed to reach a neutrino mass sensitivity of $< 20\,\mathrm{eV}$ for one year measurement time and is planned to be enhanced to reach a sub-eV sensitivity in the future.

1.5 Sterile Neutrinos

The seesaw model, as described in section 1.3.4, assumes neutrinos with right-handed chirality as crucial constituents in order to keep the active neutrino mass scale small. These right-handed neutrino singlets are called *sterile* since they do not take part in any Standard Model interaction. Though there has been no experimental evidence for sterile neutrinos yet, they are theoretically well motivated in various scenarios beyond the Standard Model, such as the Left-Right Symmetric Model (LRSM) [MP75] or some Grand Unified Theories (GUT) [BY98]. Furthermore, they pose a plausible explanation for some unsolved problems, such as dark matter [Dre+17] and Baryon asymmetry [KRS85], depending on the mass scale and the model parameters.

1.5.1 Fundamental Concept

Sterile neutrinos ν_R are gauge singlets under $SU(2)_\mathrm{L}$ with right-handed chirality. A neutrino in a pure state ν_R takes no part in any standard model interaction, in contrast to the *active neutrino* states of the standard model. However, as eq. (1.16) illustrates for the example of one active plus one sterile neutrino state, the mass states of sterile neutrinos are not necessarily identical with the flavor states, but a result from a diagonalization of the mass matrix. Similarly to the mixing between the three known active flavors and mass states (section 1.3.2), the possibility of mixing between sterile and active flavor and mass states, respectively, exists. The mixing matrix (1.9) can therefore be extended for an arbitrary number N of sterile states,

$$U_\mathrm{ext} = \begin{pmatrix} U_\alpha & U_{\alpha\mathrm{s}} \\ U_{\mathrm{s}\alpha} & U_\mathrm{s} \end{pmatrix} , \tag{1.38}$$

where U_α is a 3×3 matrix, describing the mixing purely between active states, and U_s a $N \times N$ matrix, describing the mixing between sterile states. While U_s is not physically observable without additional right-handed interactions (see section 1.5.5), the matrices $U_{\alpha\mathrm{s}}$ and $U_{\mathrm{s}\alpha}$ take into account the mixing between active and sterile states, which can have physical effects. In the important seesaw limit, defined by $m_\mathrm{R} \gg m_\mathrm{D}$ (1.16), the active mixing matrix U_α is similar to the 3×3 mixing matrix (1.9) and nearly unitary, while the elements of $U_{\alpha s}$ and $U_{s\alpha}$ are small [Aba+].

In many experimental scenarios, it is sufficient to consider only one sterile generation of interest ν_s with a mass state ν_4. In that case, the mixing matrix (1.38) gains three additional mixing angles, two CP violating phases and one Majorana phase. For a full parametrization, see e.g. [GJ08; BRZ11]. Since in the seesaw limit $m_4 \gg m_1,\ m_2,\ m_3$ and $\theta_{14}, \theta_{24}, \theta_{34} \ll \theta_{12},\ \theta_{13},\ \theta_{23}$, one can describe the mixing between a given active flavor state ν_α and the additional sterile state approximately by a single active-sterile mixing angle θ_s,

$$\begin{pmatrix} \nu_\alpha \\ \nu_s \end{pmatrix} \approx \begin{pmatrix} \cos\theta_s & \sin\theta_s e^{-i\delta_s} \\ -\sin\theta_s e^{i\delta_s} & \cos\theta_s \end{pmatrix} \begin{pmatrix} 1 & 0 \\ 0 & e^{i\lambda_4} \end{pmatrix} \begin{pmatrix} \nu_{123} \\ \nu_4 \end{pmatrix}, \tag{1.39}$$

with an effective Dirac phase δ_s and a new Majorana phase λ_4, using the abbreviation $\nu_{123} = \sum_i U_{\alpha i}\nu_i$. Hence, in case of a non vanishing mixing angle θ_s, every active neutrino produced in weak interactions also has a contribution by ν_4 (see fig. 1.7). Similar to active neutrino flavor oscillations, this also gives rise to the possibility of oscillations between active and sterile neutrinos. Furthermore, sterile neutrinos are therefore detectable in β-decay via the contribution by $|U_{e4}|^2 = \sin^2\theta_{14}$ in the decay spectrum (1.34). The phenomenology of a sterile neutrino contribution in the tritium β-decay is discussed in further detail in chapter 1.5.3.

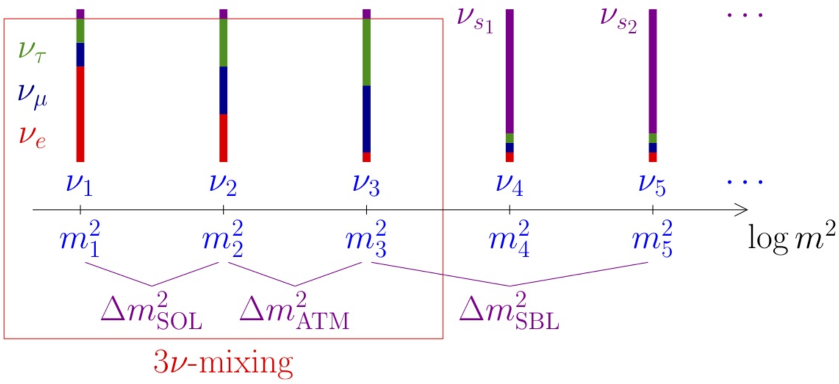

Figure 1.7: 3 + N neutrino mixing scheme with N added sterile neutrinos. *SBL* stands for short baseline. Figure from [Giu13].

There are no a priori constraints on the number and absolute scale of the sterile mass states. A natural choice from a theory point of view seems to be $N = 3$, which is assumed in some extensions of the SM (e.g. in the neutrino minimal standard model (νMSM) [ABS05; AS05]). However, to guide the experimental search for sterile neutrinos it is sufficient to focus on one additional sterile neutrino at a certain mass range, as with (1.39). Considering the mass scale, the most straightforward choice is to assume the mass of sterile neutrinos to be at a scale $m_{\mathrm{GUT}} \sim 10^{10}$ GeV – 10^{15} GeV, leading to the simple seesaw scheme of (1.16). However, in low-energy seesaw models [Aba+] there is also room for lighter sterile neutrinos, while still satisfying the criterion of suppressing the active neutrino mass scale naturally (see e.g. [ABS05]). That can be embedded in a broader framework responsible for the generation of lighter sterile neutrinos, such as e.g. the Froggatt-Nielsen mechanism [MN11], the split seesaw [KTY10] or a broken symmetry such as $L_e - L_\mu - L_\tau$ [LMN11]. Depending on the model and in particular on the mass scale of the new sterile neutrino, certain experimental anomalies can be explained or unsolved problems be taken care of.

1.5.2 eV Scale: Short Baseline Anomalies

Several experimental anomalies might be explained by a sterile neutrino on the mass scale of a few eV. These arise for instance from the reactor neutrino anomaly [Men+11], where a recent re-evaluation of the expected antineutrino flux from reactor neutrino experiment suggests a 3 % lower flux than expected. Similarly, the calibration of solar neutrino experiments GALLEX and SAGE [Ans+95; Abd+06; Abd+09; Kae+10], where radioactive sources have been placed inside the experiments, have shown a signifiant deficit of the observed count rate with respect to the calculated cross-section. These observations can be interpreted as short baseline (SBL) oscillations into a sterile state with a mass splitting $|\Delta m_s^2| := |\Delta m_{14}^2| \sim \mathcal{O}(\text{eV})$. Furthermore, the SBL accelerator neutrino oscillation experiments LSND [Ath+98] and MiniBooNE [Agu+07] showed evidence for $\bar{\nu}_\mu \rightarrow \bar{\nu}_e$ oscillations, which can not be explained with the standard three flavor oscillation scheme. However, there is tension between the data, as the results could not be reproduced by KARMEN and MINOS [Aba+].

Furthermore, the hypothesis is difficult to reconcile with cosmology. Measurements of primal abundance of deuterium at the time of the Big Bang Nucleosynthesis (BBN) [Coo+14; Cyb+16] and Cosmic Microwave Background (CMB) measurements with Planck [Ade+16] suggest that the effective number of neutrino degrees of freedom in the universe is inconsistent with a fourth neutrino with a mass of only a few eV. The tension can in principle be solved, e.g., by assuming certain non-standard interactions [HHT14; Arc+15; Arc+16]. On the other hand, the hypothesis has further been challenged by IceCube, which found no evidence for light sterile neutrinos [Aar+16]. The question might finally be solved by the KATRIN experiment (chapter 2) which will be able to exclude nearly the complete parameter space from the reactor neutrino anomaly [FB11; SH11; EP12; Kle14] (figure 1.8). Additionally, dedicated experimental efforts such as SOX [Bra+16], STEREO [Peq15] and DANSS [Ale+16] are currently under way to test the sterile neutrino hypothesis in short-baseline oscillations. Analyses of data from the KATRIN predecessor experiments in Mainz [Kra+13] and Troitsk [Bel+13] could already exclude a small region of the parameter space.

1.5.3 keV scale: Warm Dark Matter

Sterile neutrinos on a mass scale of a few keV have some reputation as candidates for warm dark matter (WDM) [Dre+17]. The discussion about WDM is partly motivated by issues regarding structure formation on small scales, which are not yet solved within the prominent cold dark matter (CDM) scenario, where dark matter is formed by supersymmetric weakly interacting massive particles (WIMPs). Examples include the *missing satellites problem*, where less and smaller dwarf satellite galaxies have been observed than predicted in N body simulations of CDM scenarios [Kly+99]. Additionally, CDM predicts the existence of massive subhalos, which either contradicts the observed number density or the internal kinematics (*too big to fail problem*) [BBK11; Pap+15]. A further example is the *cusp-core problem*, where the dark matter density profile of galaxies is predicted to increase steeply at small scales (cusps), while observations show that it is nearly flat in the center (cores) [NFW96].

A number of simulations show that these problems can be avoided if dark matter is warm and formed by a sterile neutrino with a mass of a few keV (e.g. [MFL12; Lov+12; Sch+12; DDS13; VSS14]). The production of the existing abundance of dark matter can either occur thermally via active-sterile oscillation (e.g. the Dodelson Widrow mechanism [DW94]) or by an efficient resonance mechanism (e.g. via lepton-number-driven resonant MSW conversion [SF99; LS08]). While thermal production requires a sufficiently large mix-

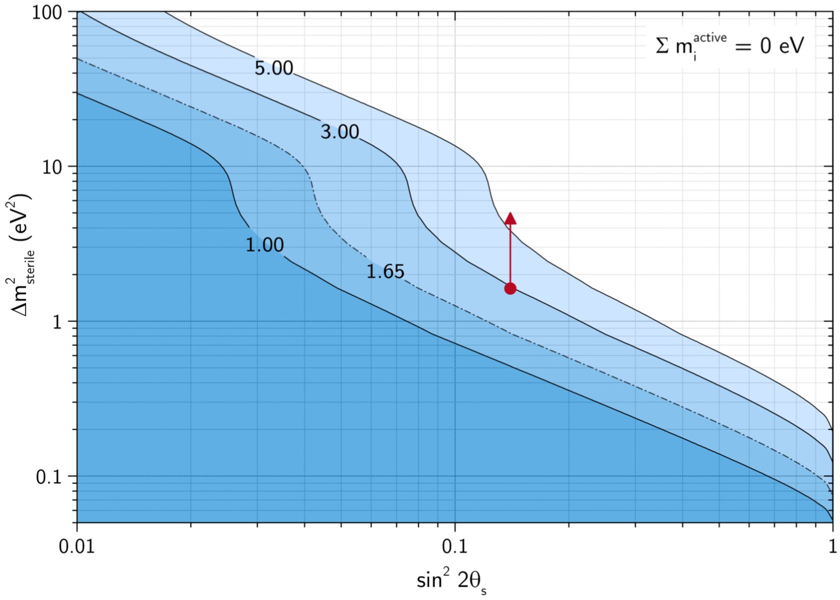

Figure 1.8: Sensitivity of KATRIN to a sterile neutrino, assuming three years of data taking and using the measurement distribution optimized for an active neutrino mass measurement. The contours show the confidence levels in terms of standard deviations σ, with the dashed line corresponding to 90 % C.L.. The parameter range favored for the solution of the reactor antineutrino anomaly [Men+11] is indicated by the red arrow. Figure from [Kle14].

ing angle, resonant production can also obtain the correct dark matter abundance for extremely small mixing angles. The sterile neutrino can decay radiatively into an active neutrino plus a photon with energies given by half the mass of the sterile neutrino, $E = m_s/2$, each. That can be used to establish bounds on the mixing angle with active neutrinos via search for an emission line using X-ray satellites (e.g. [Boy+06; WLP12]). Additionally, an upper bound can be derived theoretically, since a too large mixing angle would lead to overproduction of dark matter. The bound on the mixing angle is strongly mass-dependent (figure 1.9), however at most

$$\sin^2 \theta_s \lesssim 5 \times 10^{-8} \,. \tag{1.40}$$

The mass range can been constrained on the lower side by the Pauli exclusion principle in galactic cores (Tremaine-Gunn bound [TG79]) and by probing the matter power spectrum at small scales via Lyman-α forest data [Vie+05]. An upper bound can be established by gamma-ray line emission from the Galactic center region [YBW08]. This gives

$$0.5\,\mathrm{keV} \lesssim m_s \lesssim 50\,\mathrm{keV} \,. \tag{1.41}$$

Moreover, possible evidence of relic sterile neutrinos with mass $m_s = 7.1$ keV has been reported in XMM-Newton data [Bul+14; Boy+14]. In principle, keV scale sterile neutrinos can also be searched for in β-decay experiments [Veg+13; Mer+15a], as already outlined in the case of eV scale sterile neutrinos (section 1.5.2). However, the strong constraints on the mixing angle make this a very challenging task, requiring novel experimental and statistical means. The sensitivity of such an approach on the example of the KATRIN experiment will be discussed in chapter 4.

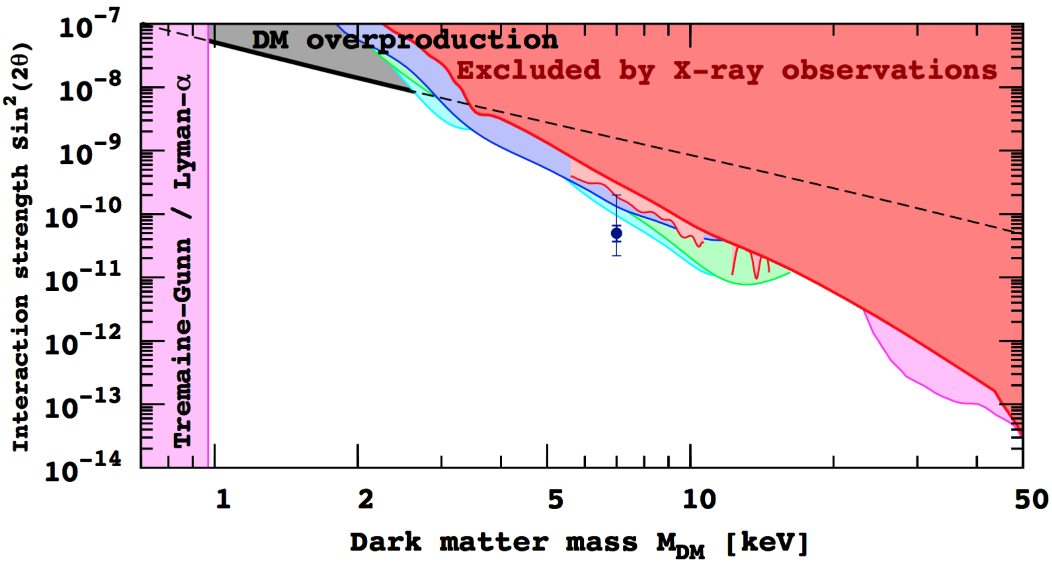

Figure 1.9: Current X-ray limits on the mixing angle $\sin^2(2\theta_s)$ as a function of the sterile neutrino mass $M_{\mathrm{DM}} := m_s$ on basis of multiple observations (see [Dre+17]). Masses below $m_s \lesssim 0.5$ keV are excluded by the Tremaine-Gunn bound [TG79] and Lyman-α data [Vie+05]. For masses below $m_s \lesssim 3$ keV, a model-dependent upper bound can be derived on basis of thermal production [DW94]. The reported signal from [Bul+14; Boy+14] (blue), which would imply a sterile neutrino with $m_s = 7.1$ keV, has been included. Figure from [Dre+17].

1.5.4 GeV Scale and Above: Leptogenesis

A particular motivation for the assumption of sterile neutrinos is the problem of baryogenesis, i.e. why there is more matter than antimatter in the universe. For efficient baryogenesis, the three Sakharov conditions [Sak91] have to be met:

1. violation of baryon number B invariance,
2. violation of C and CP invariance and
3. freeze-out out of thermal equilibrium.

While these conditions can be met in principle within the standard model, the CP violation within the quark mixing matrix alone is not strong enough to account for the present baryon asymmetry [HS95]. Therefore, a plausible scenario which is often considered is leptogenesis via sterile neutrinos [FY86]. In this mechanism, leptons are produced spontaneously from CP violating decays of heavy sterile neutrinos. The lepton asymmetry is then converted into baryon asymmetry via sphaleron processes, conserving baryon minus lepton number, $B-L$. In general, this mechanism requires large sterile neutrino masses $m_s \gtrsim 10^9$ GeV in order to establish enough CP asymmetry [DI02]. However, the mass bound can be lowered down to the GeV scale if oscillations between sterile neutrinos are instead the source of CP asymmetry, which is transferred into the active sector via the Yukawa coupling. This requires two heavy sterile neutrinos with quasi-degenerate masses and sufficiently large CP violation in the sterile mixing (e.g. [Sha08]).

1.5.5 Left-Right Symmetries

In section 1.5.1 it was mentioned that sterile neutrinos are singlets of all Standard Model interactions and thus any interactions with sterile neutrinos are only possible indirectly via active-sterile mixing. However, it is possible to think of extensions of the Standard Model with additional interactions, where sterile neutrinos take part directly. One such framework is the left-right symmetric model (LRSM) [PS74; MP75; SM75], which adds an additional $SU(2)_R$ symmetry acting only on right-handed fermion fields. Therefore, the new symmetry allows particularly interactions between sterile neutrinos and other right-handed fermions. At high energy scales, $SU(2)_R$ and $SU(2)_L$ are unified with equal coupling strength and parity is restored. However, after electroweak symmetry breaking, right-handed bosons W_R and Z_R are formed, which become very massive with respect to the left-handed weak bosons, thus suppressing $SU(2)_R$ interactions. To account for the symmetry breaking and give rise to Majorana masses for neutrinos, two Higgs triplets $\Delta_{L/R}$ and a Higgs bi-doublet ϕ are introduced. The LRSM is an elegant explanation for the parity violation of the weak interaction and can naturally accommodate light sterile neutrinos and the seesaw mechanism [MS80; BHL10; PP13; BR13].

The theory can be tested by experimental search for right-handed bosons. Current experimental limits of the mass of W_R from the LHC give [CMS14; ATL12]

$$m_{W_R} \gtrsim 3\,\text{TeV} \tag{1.42}$$

Furthermore, through mixing of left-handed and right-handed bosons, it can lead to contributions in neutrinoless double β-decay [BR13] and classic β-decay [BHR14]. The latter case will be discussed in detail on example of the KATRIN experiment for a scenario with sterile neutrinos on the eV scale (chapter 5).

Chapter 2

The KATRIN Experiment

In the last chapter, the motivation for a measurement of the absolute neutrino mass was outlined and various experimental methods have been presented to accomplish that goal, including a precise measurement of the endpoint region of the tritium β-decay spectrum. Additionally, it could be shown that tritium β-decay experiments are also potentially sensitive to sterile neutrinos. In this chapter, the upcoming *Karlsruhe Tritium Neutrino experiment* (KATRIN) [KAT04] will be explained in detail, which is built with the aim of improving the existing neutrino mass limits from tritium β by an order of magnitude to 0.2 eV (90% C.L.). The chapter will start with the general ideas and physics underlying the experiment. Then, the KATRIN specifications and set-up are described in detail.

2.1 Principles

2.1.1 Tritium β-Decay

As mentioned before (section 1.4.3), tritium is an ideal candidate for a neutrino mass measurement due to its low Q value of $Q \approx 18.6\,\mathrm{keV}$, short half-life of $t_{1/2} = 12.3\,\mathrm{y}$ and the absence of any intermediary states or energy-dependent nuclear matrix elements since it decays via a super-allowed transition. In the KATRIN experiment, a gaseous source is used [Bab+12], where tritium exists in molecular form T_2. For this particular case, the differential β-spectrum (eq. 1.34) can be written (e.g., refs. [OW08; Dre+13]) as

$$\begin{aligned}\frac{\mathrm{d}\Gamma}{\mathrm{d}E}(E) &= N\frac{G_\mathrm{F}^2}{2\pi^3}\cos^2(\theta_C)\,|M_\mathrm{nucl}|^2\,F(E,Z')\cdot p\cdot(E+m_\mathrm{e})\cdot \\ &\quad \sum_{i,j}|U_{\mathrm{e}i}|^2\cdot P_j\cdot(E_0-V_j-E)\cdot\sqrt{(E_0-V_j-E)^2-m_i^2}\,.\end{aligned} \tag{2.1}$$

In comparison to the general expression (1.34), the shape factor $S(E)$ is set to $S(E) = 1$ since the tritium β transition is super-allowed. The calculation of the nuclear matrix element yields an energy-independent factor $|M_\mathrm{nucl}|^2 = 5.55$ [RK88]. For allowed transitions in general, the Fermi function can be approximated by [Hol92]

$$F(E,Z') \approx \frac{2\pi\eta}{1-\exp(-2\pi\eta)}\,, \tag{2.2}$$

with the Sommerfeld parameter $\eta = \alpha Z'/\beta$. Near the endpoint, the Fermi function is approximately constant with $F(E_0, 2) \approx 1.187$. If the source consists of gaseous molecular tritium, as in the KATRIN experiment, the spectrum needs to be summed over the electronic and rotational-vibrational final states of the daughter molecules as in (2.1). That means that the total spectrum is a superposition of a spectra with different final states, where P_j is the probability to decay to a state with excitation energy V_j [SJF00; Dos+06; DT08], for which energy from the decay needs to be provided. [OW08]. The final states distribution of KATRIN (fig. 2.1) consists of two components. The first component corresponds the electronic ground state with a population probability of 57 %. However, due to the nuclear recoil, a number of rotational-vibrational states with a mean excitation energy equal to the recoil energy, $E_\mathrm{R} \approx 1.7\,\mathrm{eV}$, is populated [BPR15].[1] The second component consists of the electronic excited states, where the first one has an excitation energy of 27 eV.

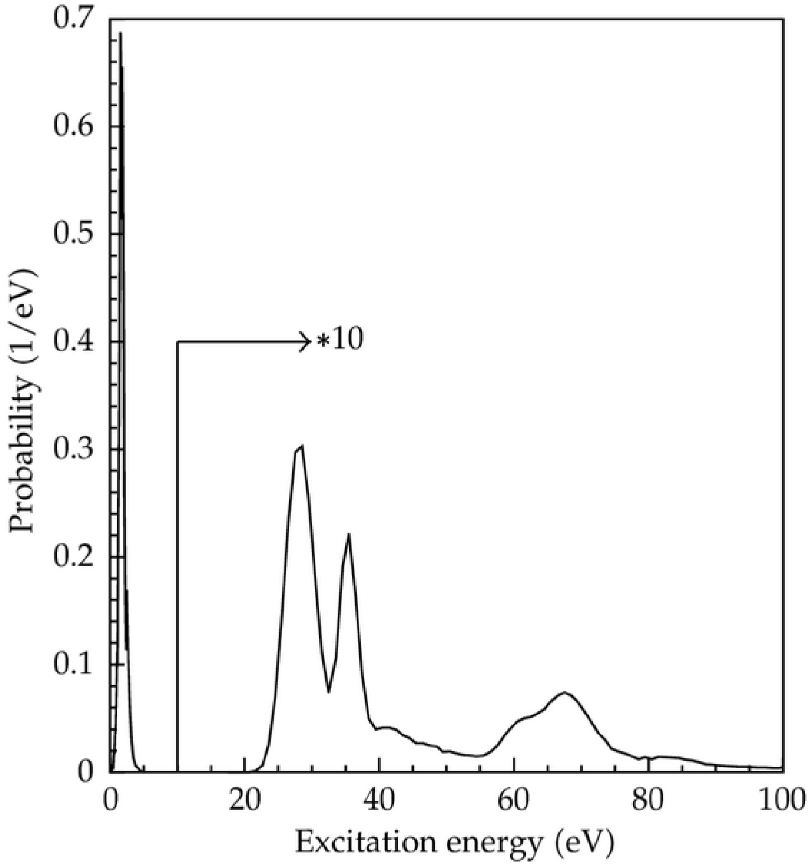

Figure 2.1: Final state distribution of the daughter molecule $^3\mathrm{HeT}^+$ as calculated by [SJF00]. Figure from [Dre+13].

Since the target sensitivity of KATRIN is still within the quasi-degenerate region, the mass eigenstates m_1, m_2 and m_3 are not distinguishable by KATRIN. Hence, the β-spectrum (2.1) can be simplified by effectively defining an average mass of the electron neutrino, which is an incoherent sum of the mass eigenstates:

$$m_{\nu_\mathrm{e}}^2 \equiv \sum_{i=1}^{3} |U_{\mathrm{e}i}|^2 m_i^2 \,. \tag{2.3}$$

With the additional abbreviation $C_\beta := G_\mathrm{F}^2/2\pi^3\ \cos^2(\theta_C)\ |M_\mathrm{nucl}|^2$, the β-spectrum (2.1) can then be written in simplified form as

[1]The recoil energy of molecular tritium and mean rotational-vibrational energy is given by half of the recoil energy of atomic tritium, each [OW08].

$$\frac{\mathrm{d}\Gamma}{\mathrm{d}E}(E) = N \cdot C_\beta \cdot F(E, Z') \cdot p \cdot (E + m_e) \cdot \sum_j P_j \cdot (E_0 - V_j - E) \cdot \sqrt{(E_0 - V_j - E)^2 - m^2_{\nu_e}} \; . \tag{2.4}$$

Figure 2.2 shows the endpoint region of the β-spectrum (2.4). In can be seen that the region where a massive neutrino leads to a significant reduction of the phase space is only a small fraction of the whole spectrum. E.g., the last 1 eV of the spectrum is only responsible for a relative fraction of $\sim 2 \times 10^{-13}$ of the decay rate. Therefore, any tritium β experiment which aims for a sub-eV sensitivity needs not only a precise energy resolution of ~ eV but also a high source activity.

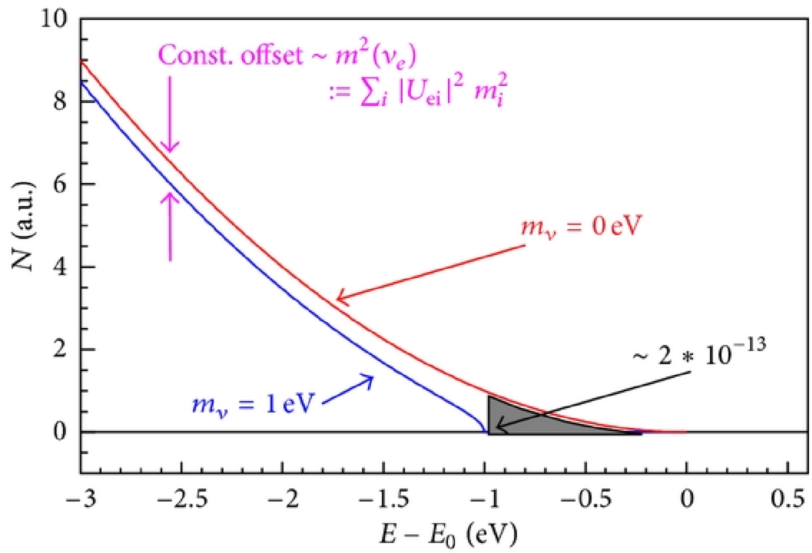

Figure 2.2: Endpoint region of differential β-spectrum (2.4) for massless neutrino (red) and neutrino with $m_{\nu_e} = 1$ eV (blue). Figure from [Dre+13].

2.1.2 MAC-E-Filter

In a classic tritium neutrino experiment the β-spectrum (2.4) is scanned with a high pass filter using different threshold energies by applying electrostatic potentials qU. For a mono-energetic electron beam with fixed starting angle, the transmission condition is given by

$$E_{||} > qU \; . \tag{2.5}$$

As the emission from the tritium source is isotropic, the principle of a *Magnetic Adiabatic Collimation with an Electrostatic Filter* (MAC-E-Filter) [Pic+92] is applied in order to align the electron momenta to a preferred direction. The isotropic electron motion at the source is converted into longitudinal motion in the *analyzing plane*, where the retarding potential qU is responsible for the high-pass filtering of the electrons. The transformation is performed by applying high magnetic fields B_S at the source and B_D at the detector, and a low field B_{min} in the analyzing plane. Under adiabatic conditions, the magnetic moment μ times the relativistic factor γ is conserved,

$$\gamma\mu = \frac{p_\perp^2}{B} = const, \tag{2.6}$$

meaning that the momentum component transverse to the B field lines $p_\perp$ is converted into parallel momentum in low magnetic field regions (Fig. 2.3). This guarantees a sharp energy resolution of the high-pass filter.

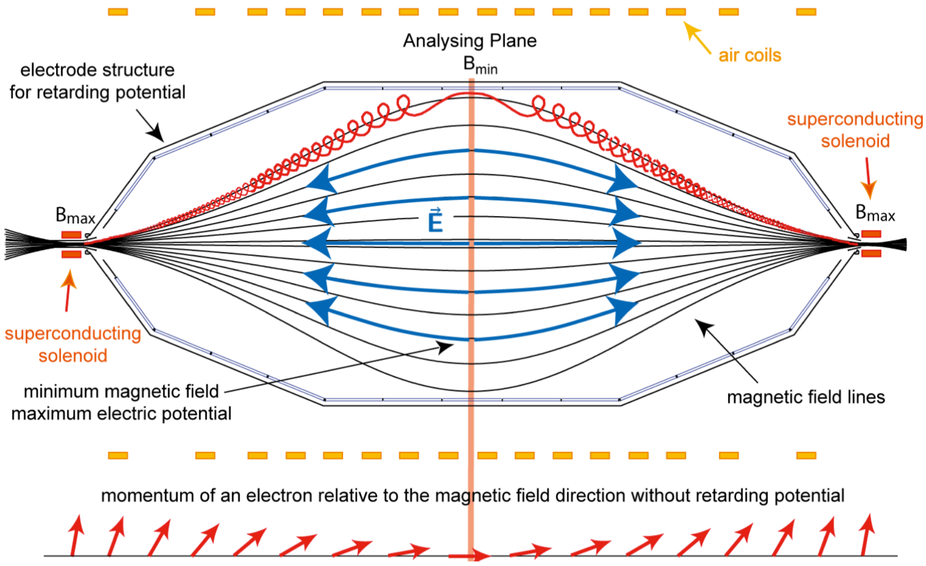

Figure 2.3: Principle of the MAC-E-Filter. The transverse momentum is transformed adiabatically into longitudinal momentum. The electron energy is then analysed by an electrostatic filter. Figure from [Bok13] .

The beam of electrons with parallel momentum is energetically analyzed by applying the retarding potential qU in the center of the analyzing plane. The relative sharpness of this energy high-pass filter depends only on the ratio of the minimum magnetic field B_{min} reached at the electrostatic barrier in the analyzing plane and the maximum magnetic field B_{max} between β-electron source and detector, where E is the starting energy of the electron from an isotropically emitting source:

$$\frac{\Delta E}{E} = \frac{B_{\text{min}}}{B_{\text{max}}} \, . \tag{2.7}$$

Since the center of motion of the electrons follows the magnetic field lines (*guided center motion*), the ratio of minimum and maximum B field and thus the energy resolution of the MAC-E-Filter is limited by the size of the flux tube A, with the conserved magnetic flux given by

$$\Phi = \int B \mathrm{d}A \, . \tag{2.8}$$

In addition, it is beneficial to place the electron source in a magnetic field B_{S} somewhat lower than B_{max}. Thus, the magnetic-mirror effect based on the adiabatic invariant (2.6) prevents electrons with large starting angles at the source, and therefore long flight paths inside the source, from entering the MAC-E-Filter. That is necessary to limit the impact of inelastic scattering of electrons in the tritium gas in the source, which leads to energy loss (see section 2.3) and contributes to the systematic uncertainty.[2] Only electrons having

[2]The scattering cross-section depends on the column density which can not be perfectly constrained.

starting angles ϑ_S at B_S of

$$\sin^2(\vartheta_S) \leq \sin^2(\vartheta_{max}) = \frac{B_S}{B_{max}} \tag{2.9}$$

are able to pass the maximum field B_{max}. The transmission probability $T(E, U)$ of the MAC-E-Filter for an isotropic emitting electron source of energy E can be analytically calculated. Normalized to unity at full transmission it reads:

$$T(E,U) = \begin{cases} 0 & \text{for } E \leq qU \\ \frac{1-\sqrt{1-\frac{E-qU}{E}\cdot\frac{B_S}{B_{min}}}}{1-\sqrt{1-\frac{B_S}{B_{max}}}} & \text{for } qU < E < qU + \Delta E \\ 1 & \text{for } E \geq qU + \Delta E \end{cases} \tag{2.10}$$

The observable of KATRIN is then the count-rate as a function the retarding potential $R(qU)$, which is the integral of the β-spectrum (2.4) above the threshold qU times an experimental response function $T'(E, U)$. The latter is the convolution of the transmission function (2.10) with certain experimental loss functions, where the dominant effect is inelastic scattering in the tritium source (section 2.3). With an additional energy-independent background rate b, the integral β-spectrum is defined by

$$R(qU) = \epsilon \cdot \frac{\Delta\Omega}{4\pi} \left(\int_{qU}^{E_0} \mathrm{d}E \, \frac{\mathrm{d}\Gamma}{\mathrm{d}E}(E) \cdot T'(E,U) \right) + b \; . \tag{2.11}$$

Additionally, $\frac{\Delta\Omega}{4\pi} = (1 - \cos\vartheta_{max})/2$ describes the accepted solid angle in the forward hemisphere, while a factor ϵ accounts for various approximately energy-independent losses, such as, e.g., a limited detector efficiency.

2.2 KATRIN Design and Setup

The aim of KATRIN is to reach a sensitivity on m_{ν_e} of 0.2 eV at 90 % C.L. for three years net measurement time [KAT04]. This aim has been the results of a careful optimization of the design parameters with respect to technical feasibility. An overview of the components is shown in fig. 2.5.

The electromagnetic design scheme is guided by the following arguments. The maximum magnetic field can be set to a value of $B_{max} = 6$ T by means of a superconducting pinch magnet at the spectrometer exit. In order to limit inelastic scattering inside the source, the source field is set to a somewhat lower value of $B_S = 3.6$ T, resulting in a maximum starting angle of $\vartheta_{max} = 50.77°$ according to (2.9). As the energy resolution is given by the ratio of maximum and minimum magnetic field (2.7), it is desirable to lower the field at the analyzing plane as much as possible, which is limited by the maximum radius of the flux-tube. The main spectrometer of KATRIN has a maximum flux tube radius of $D_A = 9$ m, allowing a minimum field of $B_{min} = B_A = 0.3$ mT with a conserved magnetic flux of $\Phi = 191\,\mathrm{Tcm}^{-2}$. According to (2.7), this corresponds to a transmission function with an energy resolution of $\Delta E = 0.93$ eV at the endpoint (see fig. 2.4)

To account for sufficient statistics, a high tritium decay rate of 10^{11} Bq is required. As shown in section 2.1.1, the endpoint region constitutes only a small fraction of the spectrum, which e.g. leads to a decay rate of ~ 2 cps within the last 10 eV of the spectrum. Therefore, KATRIN needs to be optimized for a low background of < 10 mcps, which is achieved by an ultra high vacuum (UHV) of $< 10^{-11}$ mbar inside the components [Are+16] and background

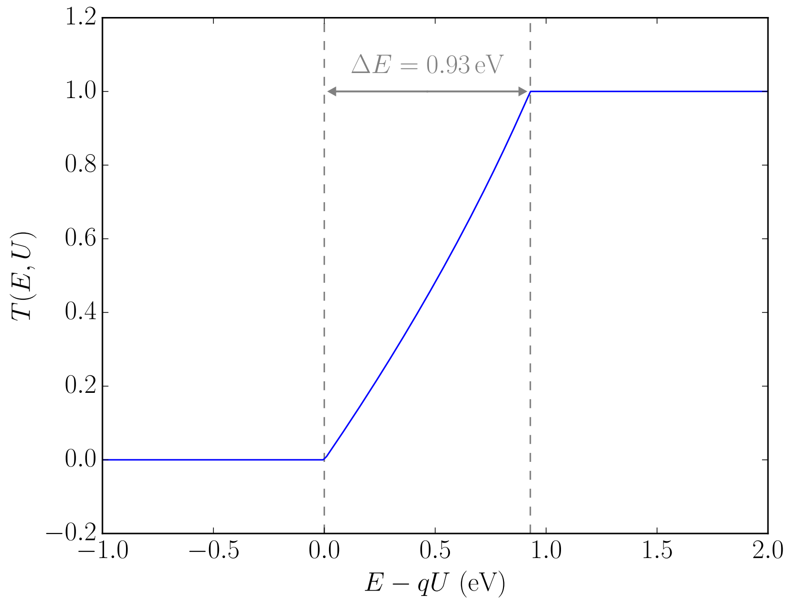

Figure 2.4: Transmission function of the KATRIN main spectrometer as function of the surplus energy $E - qU$ for an isotropic source near the endpoint $E = 18.6\,\mathrm{kV}$. The width of the transmission function is given by the energy resolution ΔE.

suppression methods such as particularly a wire electrode to shield the main spectrometer from cosmic muons (section 2.2.2) [Val10].

In the following part, a brief overview of the main components of KATRIN is given.

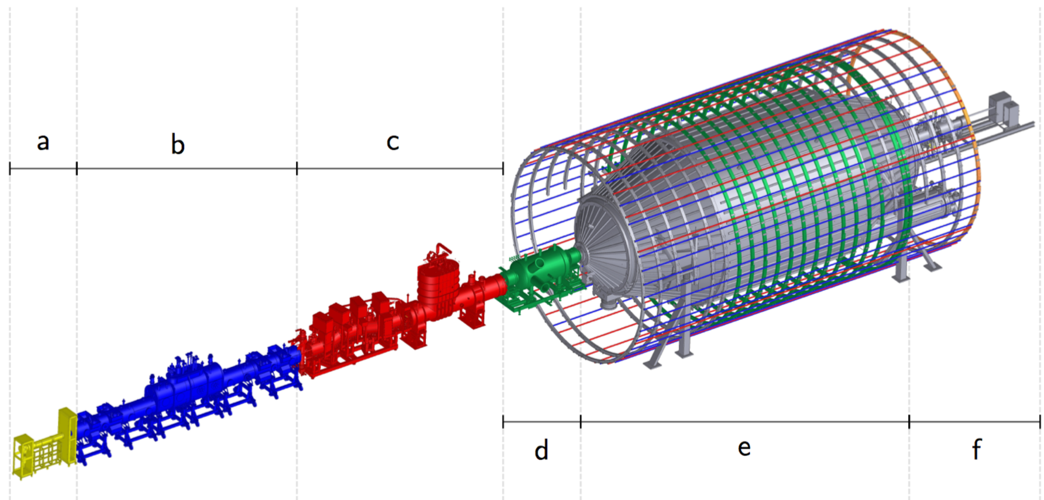

Figure 2.5: Set-up of KATRIN with main components. a) rear section and source monitoring, b) windowless gaseous tritium source (WGTS), c) transport and pumping section, d) pre-spectrometer, e) main spectrometer, f) focal plane detector (FPD).

2.2.1 Source and Transport section

The β-decay takes place in the *Windowless Gaseous Tritium Source* (WGTS, fig. 2.5, b) [Bab+12]. The desired tritium activity of $A_T = 10^{11}$ Bq (forward and backward hemispheres) is provided by a tritium column density of $\rho d = 5 \times 10^{17}$ molecules/cm^2 within a diameter of $D_S = 90$ mm and with a gas purity of $\epsilon_A = 0.95$ at a temperature of 27 K. The tritium is injected in the middle of a 10 m long tube and exhausted at the ends with turbomolecular pumps (DPS1-R and DPS1-F) where it is re-purified and returned to the cycle [Luk+12]. Since the knowledge of the column density is one of the main contributions to the systematic uncertainty of KATRIN, it is important to hold the pressure and other parameters in the source constant and monitor them precisely.

To prevent residual tritium molecules from getting into the spectrometers and causing background, the remaining tritium has to be removed. The transport section (fig. 2.5, c) consists of two units, which are a differential pumping section (DPS) and a cryogenic pumping section (CPS). The pumping at DPS-2 is performed by four turbo-molecular pumps along a slightly bended beam line, where the electrons follow the magnetic flux-tube while the neutral tritium molecules make contact with the walls where they are pumped.[3] The remaining molecules are trapped within the CPS using Argon frost at a temperature of 3 K on the inner walls along a similarly bended beam line. The tritium flow is reduced by all pumping parts DPS1, DPS2 and CPS by a total factor of $\sim 10^{14}$.

2.2.2 Spectrometer Section

The spectrometer section consists of a pre-spectrometer (fig. 2.5, d) for a coarse pre-filtering of low-energetic electrons and the main spectrometer (fig. 2.5, e), which is responsible for the energy analysis.

The pre-spectrometer is a MAC-E-Filter which operates with a retarding potential in the range of $qU \sim 18.3$ keV and with an energy resolution of $\Delta E \approx 75$ eV. Two superconducting solenoids (PS1 and PS2) at the entrance and the exit with 4.5 T each provide a high field gradient. This procedure blocks all electrons except those within the last ~ 300 eV of the spectrum. Since the electrons below that threshold carry no substantial neutrino mass information, this is an effective means of reducing the electron flux, thereby minimizing background from inelastic scattering on gas molecules inside the vessel. The shortcoming of this set-up is a trap between pre- and main spectrometer, which however can be solved by active methods of emptying the trap such as magnetic pulses [Frä+14; Beh16] or a sweeping wire scanner [Bec+10].

The main spectrometer is the central component which carries out the analysis of the electron energies near the endpoint by the MAC-E-Filter principle. It is a tank with a length of 23.3 m and a diameter of about 10 m in which the electron energies are analyzed. The field at the entrance and the exit of the main-spectrometer is provided by the PS2 magnet with 4.5 T, shared with the pre-spectrometer, and the Pinch magnet with 6 T, respectively. The magnetic field in the analyzing plane of $B_{\mathrm{min}} = 0.3$ mT is maintained by the low field compensation system / earth magnetic field compensation system (LFCS/EMCS) consisting of 14 air coils plus two wire loops [Glü+13].

The high voltage (HV) system of KATRIN [Kra16; Res17] elevates the vessel hull on a negative potential to act as a Faraday cage while the precise retarding potential qU is provided by a two-layer wire electrode system inside the main spectrometer, mounted closely to the vessel hull (fig. 2.6). The wire electrode, which is on a slightly more negative potential than the vessel hull, especially allows a reflection of background electrons from collisions of cosmic muons with the vessel hull [Val10]. Furthermore, the wire electrode shields the potential in the main spectrometer from electric inhomogeneities in the vessel hull. A two-stage set-up with two wire layers of different thickness has shown to be most efficient for

[3] Additional charged tritium ions are removed by an electric dipole system.

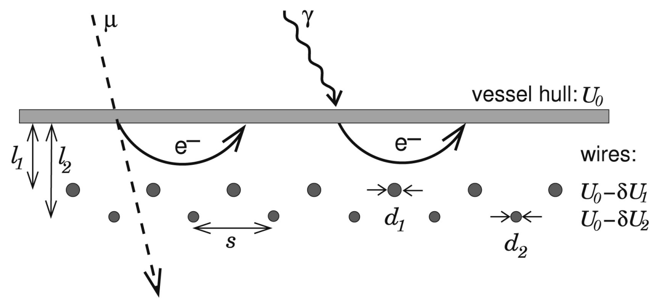

Figure 2.6: Principle of the main spectrometer wire electrode. Background electrons from the vessel hull are reflected by a slightly more negative potential. Figure from [Val10].

both purposes.

To minimize systematics, it is crucial that the HV is well calibrated and the stability monitored with a precision of 3 ppm over at least two months. This is on one hand performed by direct measurements using a high precision voltage divider [Bau+13]. On the other hand, the spectrometer from the previous Mainz experiment is used as a monitor spectrometer parallel to the beam line [Erh+14]. The latter calibrates the HV by measuring the mono-energetic electron capture from ^{83}Kr.

2.2.3 Detector Section

At the end of the beam line, the focal plane detector (FPD, fig. 2.5, f) is used to measure the number of transmitted electrons [Ams+15]. It consists of a multi-pixel silicon PIN (positive-intrinsic-negative) diode array, divided into 148 pixels in a dart-board geometry (fig. 2.7). The multi-pixel layout allows to reconstruct the flight path of the electron through the main spectrometer which is important to resolve electromagnetic inhomogeneities in the analyzing plane such as a potential depression and a magnetic field increase. The FPD is able achieve an efficiency of ~ 95 %, an energy resolution of 1.5 keV near the endpoint and a time resolution of up to 50 ns, fulfilling the requirements for additional time-of-flight measurements (chapter 3). A post-acceleration electrode provides further background reduction by shifting the electron energy by up to 10 keV behind the spectrometer.

2.3 Response and Data Analysis

As mentioned in section 2.1.2, the KATRIN observable is the square neutrino mass $m^2_{\nu_e}$, fitted from the integral β-spectrum (2.11), where the *response function* $T'(E,U)$ describes the probability of electrons with starting energy E to be counted at the detector, given a retarding potential qU. It is defined by

$$T'(E,U) := T(E,U) \otimes f_{\text{loss}}(E) \,, \tag{2.12}$$

where $T(E-qU)$ is the analytic transmission function (2.10) of width 0.93 eV for isotropic electrons, and $f_{\text{loss}}(E)$ the energy loss spectrum by inelastic scattering in the source [Ase+00; Han+17]. The response function (2.12) for qU close to the endpoint $E_0 \approx 18.6$ keV is shown in fig. 2.8.

The integral β-spectrum (2.11) is then measured by determining the count-rate per retarding energy qU. Fig. 2.9 shows the spectrum for different neutrino masses. The data are subject to a fit, using

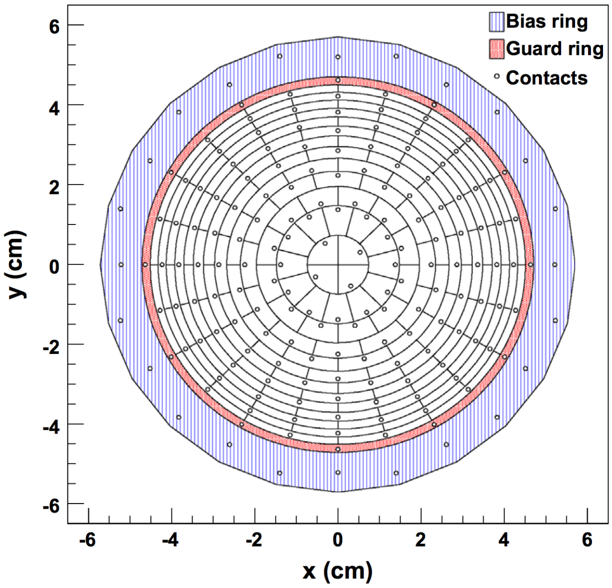

Figure 2.7: Pixel layout of the KATRIN focal plane detector (FPD). Figure from [Ams+15].

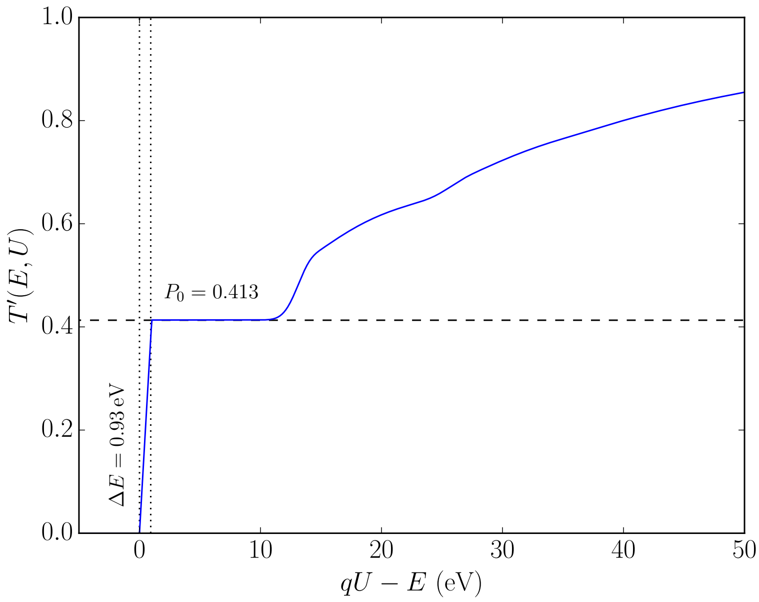

Figure 2.8: Response function of the KATRIN experiment for isotropically emitted electrons (2.12) close to the endpoint $E_0 \approx 18.6$ keV, assuming a source column density of $\rho d = 5 \times 10^{17}$ cm^{-2}. The first ~ 10 eV are described by the transmission function $T(E, U)$ (2.10) of width 0.93 eV, leading into a plateau given by the fraction of electrons of $\sim 41\%$ that have undergone no inelastic scattering process.

- the squared electron neutrino mass $m^2_{\nu_e}$,
- the β-spectrum endpoint E_0,
- the signal amplitude S or the number of tritium atoms N, respectively, and
- the background rate b,

as free parameters. For an optimum sensitivity, the measurement time distribution as a function of the retarding energy $t_{\text{meas}}(qU)$ needs to be optimized [Kle14]. In general, all optimization strategies point toward a combination of measurements at three regions, where

a) measurements above E_0 are sensitive to the background rate b,

b) measurements between E_0 and a few eV below E_0 are especially sensitive to the squared electron neutrino mass $m^2_{\nu_e}$ and

c) measurements of $\sim 10 - 30$ eV below E_0 provide the highest count-rate and are sensitive to E_0 and the signal amplitude S.

Since E_0 and some sources of systematics are not precisely known, it is not sufficient to pick singular points from these regions but to spread the choice of retarding potentials over a certain range with individual weights.

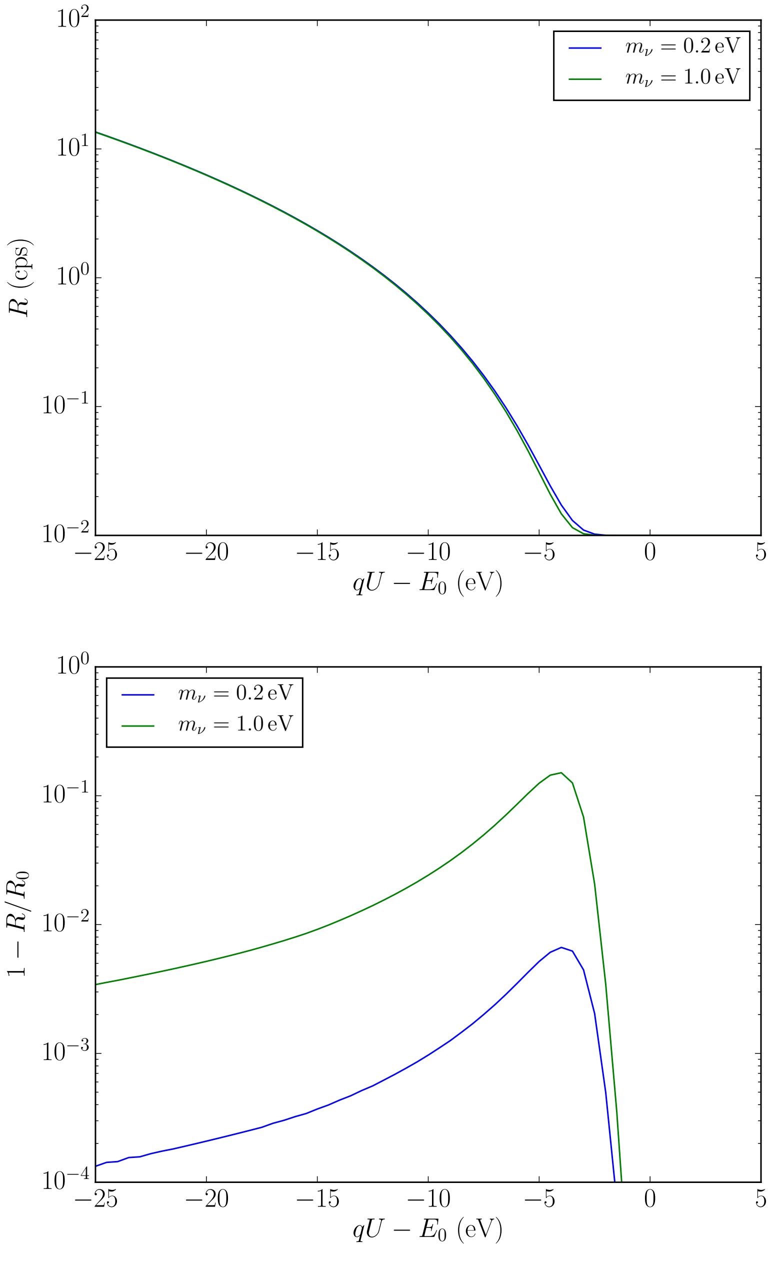

Figure 2.9: Upper figure: integral β-spectrum $R(qU)$ of KATRIN (2.11) for different neutrino masses m_{ν_e}. Lower figure: normalized ratio $1 - R(qU)/R_0(qU)$ for different neutrino masses, where $R_0(qU)$ stands for the integral β-spectrum with $m_{\nu_e} = 0$, illustrating the specific imprint of a non-vanishing neutrino mass.

Chapter 3

MAC-E-Time-of-Flight Spectroscopy

The results of this chapter have been published in the New Journal of Physics (NJP) in 2013 [Ste+13]. The chapter is based on the original draft for this publication, written by myself and edited by the co-authors of the paper. In comparison to the published version, some notations have been modified to guarantee consistency throughout the thesis. This chapter does not include the original section about electron tagging from the thesis, which was mainly composed by my collaborators in Seattle. Instead, it was replaced by a more general overview, written by myself. In addition, this chapter contains the results of experimental tests of the time-of-flight model used for the analysis (section 3.4), which have been conducted during the commissioning measurement phases SDS I and SDS II at the KATRIN experiment in 2013 and 2014/2015, respectively.

It was outlined in section 1.4 that a precise knowledge of the neutrino mass is important on one hand due to its role in cosmology regarding relic density and structure formation and on the other hand to find out which mass generation mechanism is responsible for the neutrino sector. An an especially important experimental distinction to be made is whether the mass states are hierarchical or quasi-degenerate, which has significant implications to constrain possible mass generation models. The current KATRIN sensitivity of 0.2 eV at 90 % C.L. [KAT04] is still within the quasi-degenerate region but close to the transition to the hierarchical region.

As argued in chapter 2, the sensitivity of KATRIN is principally constrained by the diameter of its spectrometer and its tritium source, which influence the energy resolution and the signal rate, respectively. Since KATRIN reaches the technical limits regarding these parameters, extending the sensitivity would require complementary methods.

In this chapter, the idea of a new measurement principle is presented. It can be performed at a suitable MAC-E-Filter setup like the main spectrometer of KATRIN. Instead of the classic integrating mode, where the count rate is scanned as a function of the retarding potential, the time-of-flight (TOF) of every electron passing through the spectrometer is measured, providing information about the electron energy. Since the endpoint region of the decay spectrum of tritium is a function of m_{ν_e}, the distribution of flight times depends as well on the neutrino mass. The MAC-E-Filter TOF mode (MAC-E-TOF) is expected to improve the sensitivity on m_{ν_e}. Since for each retarding potential not only a count rate but a full TOF spectrum is measured, the number of potential steps can be reduced without sensitivity loss. The measurement time which is gained that way can be invested in obtaining more statistics.

3.1 Principles of MAC-E-TOF Spectroscopy

3.1.1 General Idea

An alternative idea is to use *MAC-E-Filter time-of-flight (MAC-E-TOF) spectroscopy* to measure the neutrino mass. The time-of-flight (TOF) of a β-decay electron through a MAC-E-Filter like the main spectrometer of KATRIN is a function of the kinetic energy and the emission angle. The distribution of the kinetic energies is in first order governed by the β-spectrum (2.1) which contains the neutrino mass. By measuring the time of flight distribution (TOF spectrum) of the electrons, one can reconstruct the parameters determining the beta spectrum, including $m^2_{\nu_e}$. Such a method would feature mainly two intrinsic advantages.

On the one hand, the MAC-E-Filter slows down the electrons near the retarding energy. While the relative velocity differences between raw beta decay electrons near the endpoint are tiny, a TOF measurement of β electrons passing through a MAC-E-Filter will be very sensitive to subtle energy differences just above the retarding energy. It can be seen (Fig. 3.1) that, in principle, electron energy differences even below the resolution of the MAC-E-Filter, which is $\Delta E = 0.93\,\mathrm{eV}$ for 18.5 keV electrons in case of KATRIN, can be resolved, given a sufficient time resolution.

On the other hand, the standard MAC-E mode measures only the count rate for each retarding energy, as described above. In contrast, the TOF spectroscopy mode measures the TOF for each decay electron. Thus, a full TOF spectrum, sensitive to $m^2_{\nu_e}$, is obtained for each retarding energy. For suitable measurement conditions, this gain of information improves the statistics.

The combination of these advantages allows useful optimizations. In principle, it would be sufficient to measure only at a single retarding energy near the beta endpoint, though a small number of selected retarding energies might be more sensitive. Since the systematic uncertainty on $m^2_{\nu_e}$ grows as the retarding energy is decreased, the goal is to minimize the amount of measurements far from the β endpoint. The TOF method could in principle provide this and concentrate the measurement on a few retarding energies near the endpoint, each of them delivering a full TOF spectrum from which $m^2_{\nu_e}$ can be disentangled.

3.1.2 Mathematical Model

The aim is to determine the TOF spectrum as a function of certain fit parameters. These comprise the β endpoint E_0 and the square of the neutrino mass $m^2_{\nu_e}$, as well as the relative signal amplitude S which depends on several factors. In principle, E_0 is known from the ^{3}He-T mass difference measurements in Penning traps to 0.1 eV precision [Mye+15]. However, this is not precise enough to fix it ab initio. Futhermore, the Q value does not translate directly into the endpoint, since molecular effects and nuclear recoil have to be taken into account [BPR15], as well as the work function and the depression of the retarding potential of the KATRIN main spectrometer. Improvements on the β endpoint precision, aiming for $\sim 30\,\mathrm{meV}$, are on the way [Str+14]. For a full study, also a constant background rate b needs to be fitted, which is however dependent on the implementation of the measurement method. In order to obtain an expression for the TOF spectrum, the TOF has to be known as a function of the kinetic energy E and the starting angle ϑ first and then has to be weighted by the corresponding distributions given by the windowless gaseous tritium source.

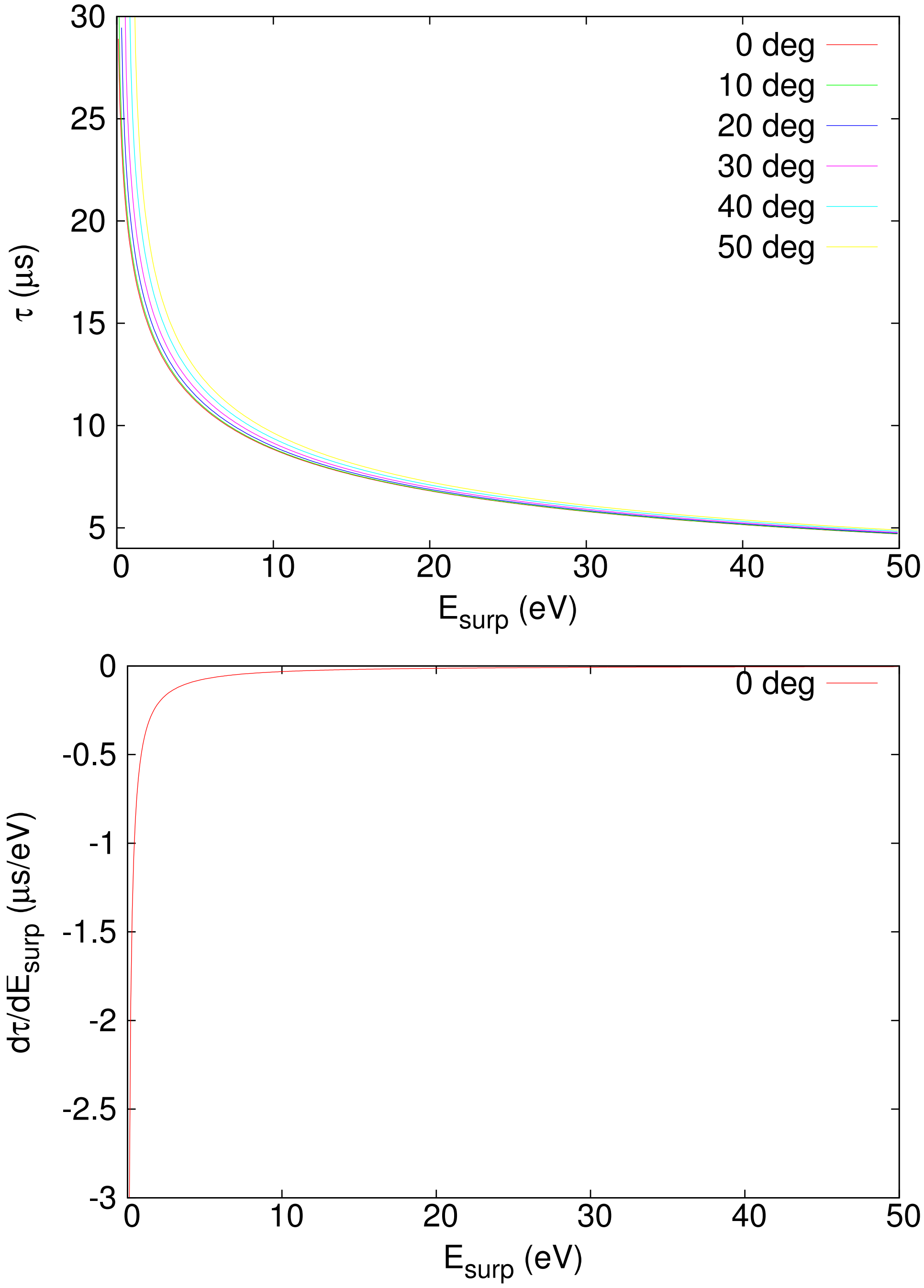

Figure 3.1: Time-of-flight for different starting angles (top) and first derivative for $\theta = 0°$ (bottom) as a function of the surplus energy $E_{\text{surp}} = E - qU$ for a central detector pixel. The starting angle is limited to 50.77 ° due to the KATRIN field design. The first derivative reflects the sensitivity on energy differences and is especially large for energies close to the retarding energy qU, i.e. $E_{\text{surp}} \longrightarrow 0$.

TOF as Function of E and ϑ

Within the main spectrometer, the principle of adiabatic motion, where the magnetic moment is constant (2.6), is valid to good approximation. Using a simplified geometry, only the field on the z axis is taken into account and magnetron drifts neglected. The B field then is only a function of the z coordinate. Hence, the transverse momentum of an electron can be derived from equation (2.6) as a function of z,

$$p_\perp^2(z) = p^2(z_0) \cdot \sin^2\theta(z_0) \cdot \frac{B(z)}{B(z_0)}, \tag{3.1}$$

where $p(z_0)$, $\theta(z_0)$ and $B(z_0)$ are the electron momentum, its emission angle and the total magnetic field at the electron starting position z_0, where it leaves the tritium source. The fraction accounts for the adiabatic magnetic field geometry of the MAC-E-filter: as the field $B(z)$ decreases, the transverse momentum is converted continuously into longitudinal momentum. The relativistic energy of the electron is given by the energy-momentum-relation:

$$E_{\mathrm{rel}}^2(z) = p_\parallel^2(z) + p_\perp^2(z) + m_\mathrm{e}^2. \tag{3.2}$$

Since the total energy $E_{\mathrm{tot}} = E_{\mathrm{rel}} + E_{\mathrm{pot}} = E_{\mathrm{kin}} + m_\mathrm{e}c^2 + E_{\mathrm{pot}}$ is conserved, the relativistic energy can be expressed as a function of z:

$$\begin{aligned} E_{\mathrm{rel}}(z) &= E_{\mathrm{rel}}(z_0) - E_{\mathrm{pot}}(z) + E_{\mathrm{pot}}(z_0) \\ &= E_{\mathrm{kin}}(z_0) + m_\mathrm{e} - q\Delta U(z), \end{aligned} \tag{3.3}$$

where $\Delta U(z)$ is the difference of the retarding voltage at the source and at z,

$$\Delta U(z) = |U(z) - U(z_0)|\,, \tag{3.4}$$

and q is the magnitude of the electron charge. Combining eqs. (3.1), (3.2) and (3.3), one can derive an expression for the longitudinal momentum as a function of z only in terms of the field B and the potential difference ΔU:

$$\begin{aligned} p_\parallel^2(z)c^2 = &\left(E^2 + 2E\, m_\mathrm{e}\right)\left(1 - \sin^2\vartheta \cdot \frac{B(z)}{B(z_0)}\right) \\ &+\ q^2\Delta U^2(z) - 2q\Delta U(z) \cdot (E + m_\mathrm{e})\,, \end{aligned}$$

where $E := E(z_0)$ and $\vartheta := \vartheta(z_0)$ denote the energy and angle with which the electron leaves the tritium source, respectively. The TOF $\mathcal{T}(E, \vartheta)$ is determined by integrating the reciprocal parallel velocity $1/v_\parallel = \gamma m/p_\parallel = E_{\mathrm{rel}}/p_\parallel$ over the measurement path,

$$\mathcal{T}(E, \vartheta) = \int \mathrm{d}z\, \frac{1}{v_\parallel} = \int_{z_{\mathrm{start}}}^{z_{\mathrm{stop}}} \mathrm{d}z\, \frac{E + m_\mathrm{e}c^2 - q\Delta U(z)}{\sqrt{p_\parallel^2(z)}}\,. \tag{3.5}$$

The lower bound z_{start} of the integration interval depends on where the start signal time is measured[1] while z_{stop} corresponds to the z-position of the detector. As the adiabatic approximation (2.6) is valid through the whole transport section, this position is arbitrary.

[1]This should preferably be at the entrance of the MAC-E-Filter, which in case of KATRIN at the entrance of the main spectrometer.

The starting angle $\vartheta = \vartheta(z_0)$ is automatically transformed to its correct value at the start position $\vartheta(z_{\text{start}})$ via (3.5), since only the ratio of local and source magnetic field $B(z)/B(z_0)$ is relevant but not the field variations between $B(z_0)$ and $B(z_{\text{start}})$.

The integral (3.5) is only correct for electrons emitted in the center of the fluxtube, $r = 0$, since the integration path is identical with the z axis. As shown in fig. 2.3, the electrons perform a cyclotron motion around the B field lines, where for the flight-times only the velocity component parallel to the B field lines $v_{\|}$ needs to be considered. Electrons emitted at $r \neq 0$ take a path different from the z axis. This is, however, not a real shortcoming of this method because at KATRIN the starting position can be reconstructed by the point of arrival on the multipixel detector. Therefore, significant changes in sensitivity depending on the electron emission radius are not expected. For this principle study of the statistical sensitivity it is considered to be sufficient to use the central electron tracks only.

3.1.3 TOF Spectrum

Equation (3.5) presumes a fixed kinetic starting energy and starting angle as arguments. For a real source, these parameters are not fixed but follow physical distributions. The TOF spectrum can formally be derived from the double differential event rate $\frac{\mathrm{d}^2N}{\mathrm{d}\vartheta\ \mathrm{d}E}$ as function of the starting energy E and starting angle ϑ, using the transformation theorem for densities [Gil83], giving

$$\frac{\mathrm{d}N}{\mathrm{d}\tau} = \int_0^{\vartheta_{\max}} \int_{qU}^{E_0} \mathrm{d}\vartheta\ \mathrm{d}E\ \frac{\mathrm{d}^2N}{\mathrm{d}\vartheta\ \mathrm{d}E} \delta\big(\tau - \mathcal{T}(E,\vartheta)\big). \tag{3.6}$$

In order to be calculated numerically, the differential TOF spectrum $\mathrm{d}N/\mathrm{d}\tau$ is discretized into bins of constant length $\Delta\tau$ and integrated over each bin j, leading to a binned spectrum:

$$F(\tau_j) := \int\limits_{\tau_j}^{\tau_{j+1}=\tau_j+\Delta\tau} \mathrm{d}\tau\ \frac{\mathrm{d}N}{\mathrm{d}\tau}\ . \tag{3.7}$$

The number of events in a certain TOF bin depends on the distribution of starting energies and angles E and ϑ:

$$\begin{aligned} F(\tau_j) &= \iint\limits_{(E,\,\vartheta) \text{ with } \tau_j \leq \mathcal{T}(E,\vartheta) \leq \tau_{j+1}} \frac{\mathrm{d}^2N}{\mathrm{d}\vartheta\ \mathrm{d}E}\ \mathrm{d}\vartheta\ \mathrm{d}E \\ &= \int\limits_0^{\vartheta_{\max}} \int\limits_{E_j(\vartheta)}^{E_{j+1}(\vartheta)} \frac{\mathrm{d}^2N}{\mathrm{d}\vartheta\ \mathrm{d}E}\ \mathrm{d}\vartheta\ \mathrm{d}E\ . \end{aligned} \tag{3.8}$$

The integral limits $E_j(\vartheta)$ and $E_{j+1}(\vartheta)$ are defined in such way that $\mathcal{T}(E_j,\vartheta) = \tau_j$ and $\mathcal{T}(E_{j+1},\vartheta) = t_{j+1}$, respectively. At first order, $\frac{\mathrm{d}^2N}{\mathrm{d}\vartheta\ \mathrm{d}E}$ is given by the double differential decay rate $\frac{\mathrm{d}^2\Gamma}{\mathrm{d}\vartheta\ \mathrm{d}E}$ into the accepted solid angle $\frac{\Delta\Omega}{4\pi}$,

$$\frac{\mathrm{d}^2N}{\mathrm{d}\vartheta\ \mathrm{d}E} \approx \frac{\mathrm{d}^2\Gamma}{\mathrm{d}\vartheta\ \mathrm{d}E}\ . \tag{3.9}$$

As the double differential is proportional to the joint probability distribution of emitting an electron with energy E at a polar angle of ϑ and, furthermore, the angle and the energy are uncorrelated in case of a non-oriented radioactive source, the quantity can be separated into a product of the single differential decay rate $\frac{\mathrm{d}\Gamma}{\mathrm{d}E}$, as given by the β-spectrum (2.1), and the angular probability distribution $g(\vartheta)$ [Cow98],

$$\frac{\mathrm{d}^2\Gamma}{\mathrm{d}\vartheta\ \mathrm{d}E} = \frac{\mathrm{d}\Gamma}{\mathrm{d}E} \cdot g(\vartheta)\ . \tag{3.10}$$

In case of an isotropic tritium source, a sine law applies for the angular distribution,

$$g(\vartheta) = \frac{1}{2} \sin\vartheta\ . \tag{3.11}$$

This angular distribution function is normalized to unity over the full solid angle 4π. Since for KATRIN the polar angle is restricted to $\vartheta_{\mathrm{max}} = 50.77°$, the signal rate is implicitly reduced by a factor

$$\int_0^{\vartheta_{\mathrm{max}}} d\theta\ g(\vartheta) = \frac{\Delta\Omega}{4\pi} = \frac{(1-\cos\vartheta_{\mathrm{max}})}{2} \tag{3.12}$$

which is enforced by the upper integral bound ϑ_{max} in (3.8).

The approximation (3.9) is only valid in case of an ideal tritium source. However, quite a few electrons lose energy in elastic and inelastic scattering processes with the tritium molecules. These losses are dependent on the emission angle, since the path through the tritium source increases with $1/\cos\vartheta$. Thus, for the differential rate of events which are actually analysed in the main spectrometer, given by $\frac{\mathrm{d}^2N}{\mathrm{d}\vartheta\ \mathrm{d}E}$ in (3.8), starting energies and angles become correlated. Additionally, the signal rate decreases due to several losses inside the experiment. A factor $\epsilon_{\mathrm{flux}} \approx 0.83$ applies since the flux tube transported through the whole system corresponds to a diameter of 82 mm w.r.t to the beam tube diameter of 90 mm, meaning that only a part of the WGTS tube is imaged onto the detector. Furthermore, the detector efficiency gives an additional factor which is conservatively estimated to be $\epsilon_{\mathrm{det}} \approx 0.9$.

In total, the true event rate can be calculated by by applying the correction factors and convoluting the β-spectrum with an energy loss function, which gives

$$\begin{aligned}\frac{\mathrm{d}^2N}{\mathrm{d}\vartheta\ \mathrm{d}E} &= \epsilon_{\mathrm{flux}} \cdot \epsilon_{\mathrm{det}} \cdot g(\vartheta) \cdot \frac{\mathrm{d}\Gamma}{\mathrm{d}E} \otimes f_{\mathrm{loss}}(\Delta E|\vartheta) \\ &= \epsilon_{\mathrm{flux}} \cdot \epsilon_{\mathrm{det}} \cdot g(\vartheta) \cdot \left(p_0(\vartheta) \cdot \frac{\mathrm{d}\Gamma}{\mathrm{d}E} + \sum_{n=1}^{\infty} p_n(\vartheta) \cdot \frac{\mathrm{d}\Gamma}{\mathrm{d}E} \otimes f_n(\Delta E) \right),\end{aligned} \tag{3.13}$$

where the f_n is the energy loss function of scattering order n which is defined recursively through the single scattering energy loss function f_1 as

$$f_n = f_{n-1} \otimes f_1 \qquad (n > 1)\ . \tag{3.14}$$

The function $f_1(\Delta E)$ is the probability density of losing the energy ΔE in a singular scattering event [Ase+00]. The functions of f_n can then correspondingly be interpreted as the same for n-fold scattering. In this equation, all changes of the angle of the electron during scattering are neglected. p_n is the probability that an electron is scattered n times. If, again, changes of the angle are neglected, it is a function of the emission angle θ and given by a Poisson law

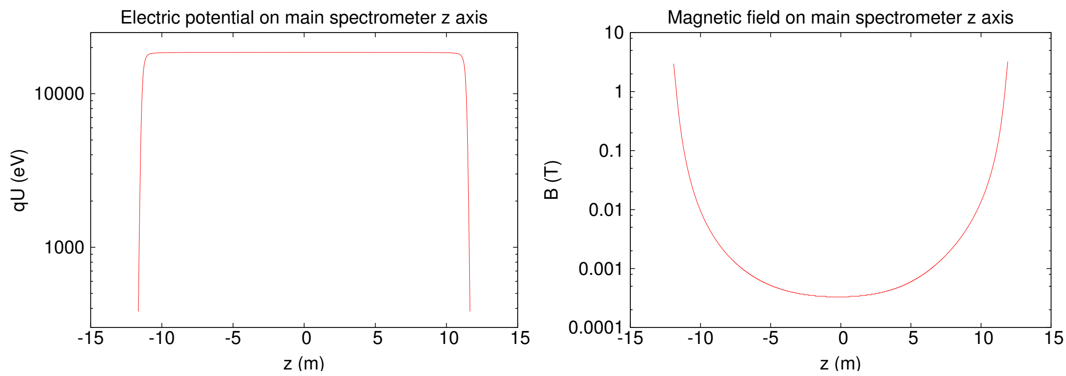

Figure 3.2: Electric potential (a) and magnetic field (b) along the inner axis of the KATRIN main spectrometer generated by simulation. The scaling of the electric potential depends on the retarding energy qU.

$$p_n(\theta) = \frac{\lambda^n(\theta)}{n!} e^{-\lambda(\theta)} . \tag{3.15}$$

Here, the expectation value λ is given in terms of the column density ρd, the mean free column density ρd_{free} and the scattering cross section σ_{scat} as

$$\lambda(\theta) = \int_0^1 \mathrm{d}x \, \frac{\rho d \cdot x}{\rho d_{\text{free}} \cdot \cos\theta} = \int_0^1 \mathrm{d}x \, \frac{\rho d \cdot x \cdot \sigma_{\text{scat}}}{\cos\theta} , \tag{3.16}$$

where the integration factor x accounts for the fact that the starting position of the electron inside the WGTS is statistically distributed.

3.2 Simulation of an Ideal TOF Mode

3.2.1 Study of TOF Spectra

To calculate the TOF spectrum according to (3.8), the input parameters have to be obtained. A model for the one-dimensional field maps $\Delta U(z)$ and $B(z)$ in (3.5) has been determined by the KATRIN simulation tools *magfield* and *elcd3_2* [Val09], using a modestly simplified geometry that contains the most important coils and electrodes in the main spectrometer (Fig. 3.2). A model for the energy loss function (3.14) has been determined in the past by electron scattering experiments on hydrogen [Ase+00] and refined by using excitation and ionisation data from hydrogen molecules [Glü]. The final-state excitation spectrum of the daughter molecules has been used from reference [SJF00].

A typical set of simulated TOF spectra for different neutrino mass squares is shown in Fig. 3.3. The following details and parameter-dependent behaviour can be observed:

- For each spectrum, there exists a minimal TOF τ_{min}. This corresponds to the maximum kinetic emission energy that an electron can have, given by $E_{\text{max}} = E_0 - m_{\nu_e}$.

- From τ_{min} on, a steep slope begins, leading soon to a maximum somewhat above τ_{min}, followed again by a long, slow fall. The maximum can be explained by the fact that the higher the energy becomes, the lower the number of electrons is, due to the shape of the end of the β-spectrum, whereas the "TOF energy density", i.e. the interval size of the energy that corresponds to a certain TOF bin, increases. These effects balance each other, leading to a maximum somewhere in the middle.

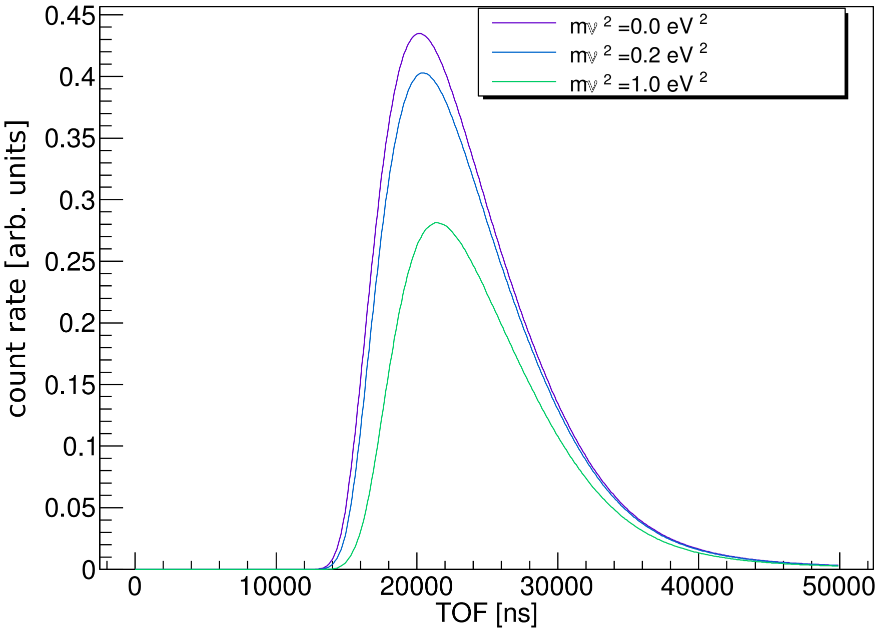

Figure 3.3: Effects on the TOF spectrum for different neutrino masses at a high retarding potential (18570 eV) with endpoint $E_0 = 18\,574.0$ eV. The scaling of the y-axis is arbitrary. Figure first published in [Ste+13].

- There is no maximal TOF. The closer the energy of an electron is to the retarding energy, the slower it will be. That means that electrons with an energy infinitesimally above the retarding energy will have an infinite TOF.
- If the neutrino mass square $m^2_{\nu_e}$ is changed, the main signature is a change in countrate and a change of the shape especially at the short-time end of the spectrum (Fig. 3.3).
- A higher retarding energy qU leads to a clearer distinction between spectra for different neutrino masses. The reason is that the neutrino mass is mainly visible in the last few eV of the beta spectrum. Therefore, it seems optimal for the TOF mode to measure with retarding energies near the endpoint. However, due to the lower count rate and the difficult decorrelation of neutrino mass square and endpoint, measurements from lower retarding energies should be added to the data.

3.2.2 Neutrino Mass Fits

In order to study the statistical uncertainty, the spectra have been used to fit Monte Carlo (MC) data. The MC data have been obtained by creating Poisson distributed random numbers based on the predictions from (3.8), where certain choices of the parameters $m^2_{\nu_e}$ and E_0, as well as the retarding energy qU and the measurement time have been assumed. The data are fitted in this self-consistent method by the models (3.8) using a χ^2 minimization method. If multiple measurements with different qU are assumed, they can be fitted with a common χ^2 function by adding the individual χ^2 functions from each run. If the fit is performed correctly, the chosen parameters $m^2_{\nu_e}$ and E_0 are reproduced. Additionally, estimates for the parameter errors can be determined as

$$\chi^2(\phi_0 \pm \Delta\phi_\pm) = \chi^2(\phi_0) + 1 \,, \tag{3.17}$$

Table 3.1: Average statistical uncertainty $\left\langle \sigma_{\text{stat}}(m^2_{\nu_e}) \right\rangle = \left\langle \frac{1}{2}(|\Delta m^2_{\nu_e-}| + |\Delta m^2_{\nu_e+}|) \right\rangle$ (arithmetic mean of positive and negative error of 10 simulations and fits), average fit parameters $\left\langle \bar{E}_0 \right\rangle$ and $\left\langle m^2_{\nu_e} \right\rangle$, as well as average Pearson's correlation coefficient $\left\langle R(E_0, m^2_{\nu_e}) \right\rangle$ between endpoint and squared neutrino mass of uniform and optimized distributions and the KATRIN standard mode. The total assumed measurement time is the KATRIN standard of three years [KAT04], distributed among four retarding energies qU =18550 eV, 18555 eV, 18560 eV and 18565 eV as well as for single retarding potentials for $m^2_{\nu_e} = 0$, $E_0 = 18\,575$ eV and $b = 0$. The choice of retarding potentials for the TOF mode is motivated by the idea that a choice of a few potentials close to the endpoint will likely improve the systematics additionally to the statistical uncertainty. Results first published in [Ste+13].

measurement time distribution $(\cdot\ 3\ \text{y})$	distribution type	lowest retarding potential (eV)	$\left\langle \sigma_{\text{stat}}(m^2_{\nu_e}) \right\rangle$ (eV^2)	$\langle E_0 \rangle$ (eV)	$\left\langle m^2_{\nu_e} \right\rangle$ (eV^2)	$\langle R \rangle$
$(\frac{3}{12}, \frac{3}{12}, \frac{3}{12}, \frac{3}{12})$	uniform	18550	0.0033	18574.9997	0.0004	0.65
$(\frac{1}{12}, \frac{0}{12}, \frac{3}{12}, \frac{8}{12})$	optimized	18550	0.0032	18575.0002	0.0013	0.70
$(0, \frac{4}{12}, \frac{4}{12}, \frac{4}{12})$	uniform	18555	0.0034	18575.0002	0.0015	0.73
$(0, \frac{2}{12}, \frac{1}{12}, \frac{9}{12})$	optimized	18555	0.0034	18575.0002	0.0006	0.72
$(0, 0, \frac{6}{12}, \frac{6}{12})$	uniform	18560	0.0036	18575.0002	0.0014	0.74
$(0, 0, \frac{4}{12}, \frac{8}{12})$	optimized	18560	0.0035	18575.0007	0.0034	0.76
$(1, 0, 0, 0)$	single	18550	0.0035	18575.0000	0.0004	0.82
$(0, 1, 0, 0)$	single	18555	0.0036	18575.0000	0.0003	0.88
$(0, 0, 1, 0)$	single	18560	0.0038	18574.9999	-0.0015	0.79
$(0, 0, 0, 1)$	single	18565	0.0039	18574.9998	0.0007	0.66
-	standard mode	18555	0.020			
-	standard mode	18550	0.019			
-	standard mode	18545	0.018			

where ϕ_0 is a parameter estimate and $\Delta\phi_\pm$ are the requested, not necessarily symmetric parameter error bars [Cow98]. To obtain a symmetric χ^2 parabola for neutrino masses near zero, there must also be an extension for a negative $m^2_{\nu_e}$ that joins smoothly with the physical spectrum for $m^2_{\nu_e} > 0$. To accomplish this, to each term in the sum of the beta spectrum (2.1) a factor

$$f_i = \left(1 + \frac{m_{\text{eff}}}{\epsilon_i} e^{-(1+\epsilon_i/m_{\text{eff}})}\right) \tag{3.18}$$

is applied in case of $m^2_{\nu_e} < 0$ and $\epsilon_i + m_{\text{eff}} > 0$. In this expression, the abbreviations $\epsilon_i = E_0 - V_i - E$ and $m_{\text{eff}} = \sqrt{-m^2_{\nu_e}}$ have been used [Wei+93]. This method allows a simple but realistic prediction of the statistical uncertainty of $m^2_{\nu_e}$.

Results

In order to determine the improvement potential by the TOF mode, an optimal choice of the measurement times of the runs with different retarding energies qU has to be made. For KATRIN a total data taking time of three years is planned, which has to be distributed among the retarding energies. A simple algorithm has been used where the retarding potentials and the measurement time have been discretized and the statistical uncertainty with the method above for all possible permutations has been determined. The results are shown in table 3.1. At the MC data creation, a neutrino mass of zero has been assumed. In this case, the average of the fit uncertainties $m^2_{\nu_e}$, as given by (3.17), describes the sensitivity on the neutrino mass squared.

The comparison shows that it is in principle sufficient to measure at only one retarding energy. If this single retarding energy is close to the endpoint, the correlation between the parameters E_0 and $m^2_{\nu_e}$ becomes weaker at the cost of losing count-rate. It turns out that it is beneficial to combine measurements at more than one retarding energy, where this relation between lowest retarding energy and correlation coefficient does not neccessarily hold true (see table 3.1) In almost all tested cases using multiple retarding potentials, a solid de-correlation has been possible without suffering from a too small count-rate.

The results in Table 3.1 correspond to an optimum case where background, time uncertainty and other limitations have been neglected. They reflect the maximal improvement potential that can be achieved with a TOF mode. The motivation to neglect the background in the optimum case is based on the idea that a sensitive TOF measurement method may be able to reduce the background as well, depending on the implementation of the measurement. It can be shown that, compared with the statistical sensitivity for the reference configuration of KATRIN, $\sigma_{\text{stat}}(m^2_{\nu_e}) = 0.018\,\text{eV}^2$, an improvement of up to a factor ~ 5-6 by TOF spectroscopy is possible. The actual improvement factor, however, depends on the method by which the time-of-flight determination is implemented.

Furthermore, one can conclude that even a reduction of the systematic uncertainty might be possible with the TOF mode, since the systematic uncertainty at KATRIN depends heavily on the measurement interval at which the spectrum is scanned [KAT04]. That is mainly caused by the uncertainty of the parameters of the electron energy loss, which becomes more relevant at lower retarding energies. An ideal TOF mode, in contrast, would allow to measure solely at higher retarding energies.

For further analyses, the optimal distribution for the case of a lowest retarding energy of 18560 eV has been used, which is likely a good compromise between statistical and systematic uncertainty. An example for a fit, based on this particular measurement time distribution, is shown in fig. 3.4.

3.3 Measurement Methods

In the last section, an ideal measurement of TOF with infinite time resolution and no background was assumed. However, the problem of finding a sufficiently sensitive and realizable method of measuring TOF spectra is by no means trivial and still subject of research. Depending on the method, further corrections that manifest in the shape of the TOF spectrum (3.8) can apply additionally. In this section, two methods and their implications for the measured TOF spectrum will be discussed. The first is a hypothetical method of detecting electrons, entering the main spectrometer, with sufficient time resolution and with minimal interference with their energy, called *electron tagging*. The second method, called *gated filtering*, periodically blocks the electron beam at the entrance of the main spectrometer, e.g., by pulsing the pre-spectrometer retarding potential, in order to obtain an arrival time spectrum at the detector which approximately corresponds to the TOF spectrum.

3.3.1 Generic Parameters

At first, the performance of a TOF system shall be evaluated under generic assumptions. Several parameters apply to most methods, chiefly the background rate, the time resolution and the efficiency. The dependence of the statistical uncertainty on the efficiency ϵ, i.e. the ratio of events whose TOF is correctly measured, follows a $1/\sqrt{\epsilon}$ law. This behavior is theoretically predicted and has been verified by simulations. The dependence on the background rate and the time resolution found in the simulations is shown in Fig. 3.5.

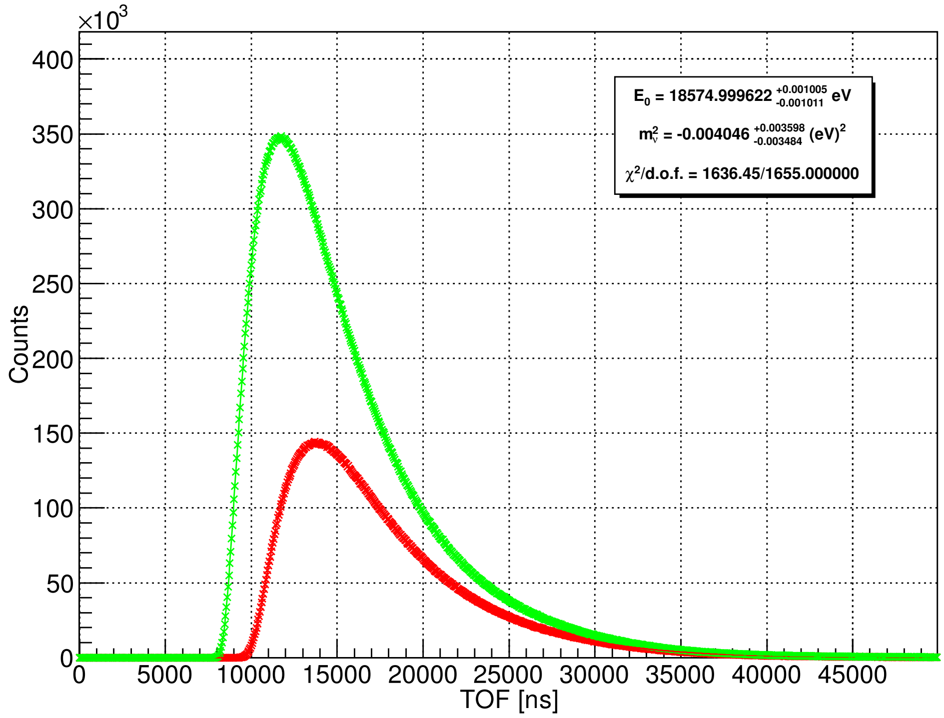

Figure 3.4: Example of simulated data and fit of a TOF spectrum for the optimal case of no background and no time uncertainty. For the fit, a measurement time of 3 years was assigned 2/3 to 18565 eV (red points online, smaller amplitude) and 1/3 to 18560 eV (green points online, larger amplitude). These correspond to the optimum distribution for lowest retarding energy of 18560 eV in Table 3.1). Figure first published in [Ste+13].

For the time resolution, a Gaussian uncertainty has been assumed, which is imposed on the TOF spectrum via convolution with a normal distribution,

$$\left(\frac{\mathrm{d}N}{\mathrm{d}\tau}\right)_{\sigma_t} = \left(\frac{\mathrm{d}N}{\mathrm{d}\tau}\right) \otimes N(0, \sigma_t) \; . \tag{3.19}$$

Fig. 3.5 shows that the timing is uncritical for resolutions within the order of magnitude of the KATRIN detector. For resolutions in the range up to 200 ns, the error increases by about 20 %. The scale of this behaviour is plausible insofar as the scale of the neutrino-mass-sensitive part of the TOF spectrum is mainly contained in the first few μs after the onset (see Fig. 3.3) and becomes washed out if the time resolution of the TOF measurement method exceeds some 100 ns.

Assuming the background level in the TOF mode is the same as in the standard mode, where it is specified for KATRIN as $b < 10\,\mathrm{mcps}$, it can be shown that the improvement by the TOF mode is still up to a factor 3 in terms of $m^2_{\nu_e}$. The behaviour follows a power law with approximately $\sigma_{\mathrm{stat}}(m^2_{\nu_e}) = 0.006\ \mathrm{eV}^2 \cdot (b/\mathrm{cps})^{1/2.0} + 0.004\ \mathrm{eV}^2$.[2] In comparison, in the standard mode the background dependence can be determined to be approximately $\sigma_{\mathrm{stat}}(m^2_{\nu_e}) = 0.019\ \mathrm{eV}^2 \cdot (b/\mathrm{mcps})^{1/1.7} + 0.009\ \mathrm{eV}^2$ [Mer+13], in reasonable agreement with the analytically approximated formula of $\sigma_{\mathrm{stat}}(m^2_{\nu_e}) \propto b^{1/3}$ [OW08].

[2]Here, no correlation between background and starting signal as in the tagger case has been assumed.

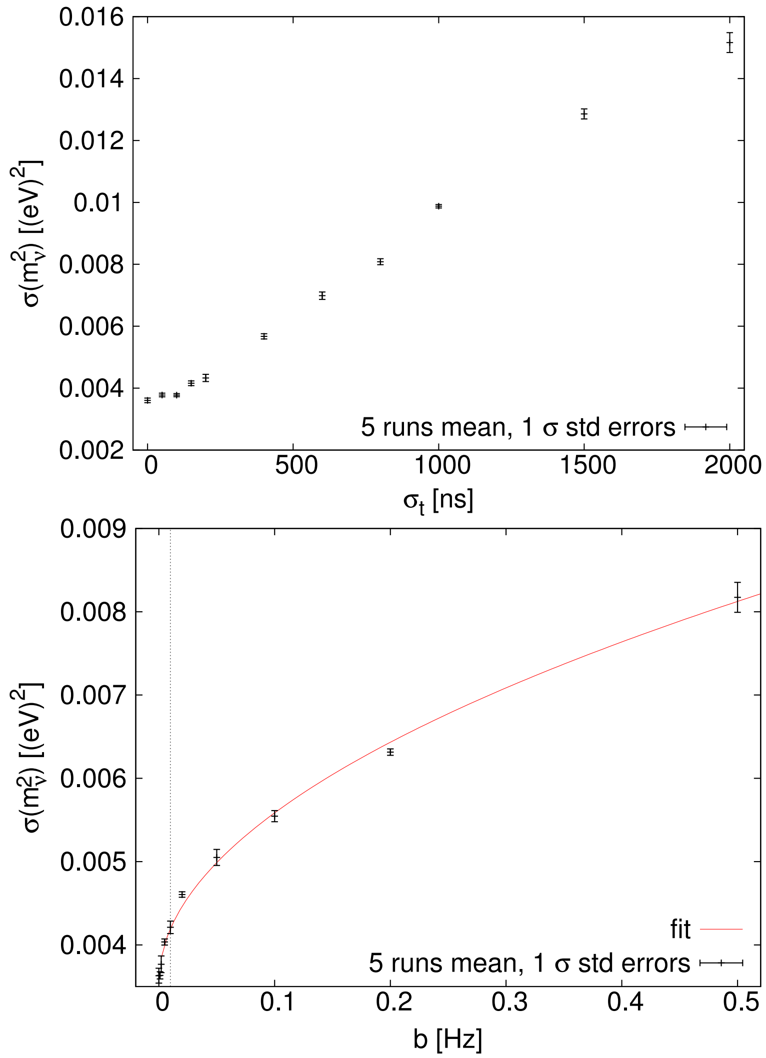

Figure 3.5: Statistical uncertainty of $m^2_{\nu_e}$ as a function of time resolution σ_t (a) and background rate b (b). The results are based on a measurement time distribution of 2/3 and 1/3 of three years in total, assigned to 18565 eV and 18560 eV, respectively (optimum distribution for 18560 eV lowest retarding energy in Table 3.1). In both plots the results from 5 simulation runs with identical parameters and different random numbers have been averaged. The dashed line in (b) corresponds to the KATRIN standard mode design goal of b = 10 mcps. The solid line in (b) represents the best fit by an inverse power law of the form $\sigma(x) = \sigma_0 + x^{1/a}$. Figures first published in [Ste+13].

3.3.2 Electron Tagging

In the hypothetical scenario of electron tagging, it is assumed that there are technical means of detecting electrons entering the main spectrometer with minimal interference, meaning that the electron momentum and direction would be preserved with sufficient accuracy. If such a start signal could be obtained with sufficient time resolution, the TOF for each individual electron could be measured via coincidence with a stop signal from the focal plane detector.

While there has been no breakthrough in implementing electron tagging yet, several ideas are subject of ongoing study. These comprise, e.g., work done by electrons passing through a microwave cavity, image charges induced in a Schottky pickup or measurement of the cyclotron radiation emitted by the electron when passing a region of a high magnetic field (c.f. [Asn+15]). The general challenge is to extract a minimal amount of energy from the electron, which is well below the energy resolution of the main spectrometer, but still distinguishable from thermal noise, $\Delta E \gtrsim k_{\mathrm{B}}T$. For a detailed discussion, see [Ste+13], section 5.

In addition to a sensitive start signal for a TOF measurement, such a method would intrinsically reduce the background strongly. The background suppression is based on the principle that stop signals may only be accepted in case of a prior start signal within a certain time window of width t_o. By that, most background events can be differentiated from real β-decay events. Neglecting pile-up, random coincidence would result in a background reduction of a factor k with

$$\frac{1}{k} = 1 - e^{t_o \cdot r_s} \ , \tag{3.20}$$

given a sufficiently low expected rate of start signals r_s. A too high rate of start signals, either due to a high flux of electrons or to a high noise level, would impair the measurement. However, in a dual-spectrometer setup like KATRIN, the flux can be reduced by the pre-spectrometer down to $\mathcal{O}(10^3$ cps). On the other hand, electrons stored between the pre- and main spectrometer could as well give rise to a high number of start signals and may compromise a TOF measurement. Trapped electrons, however, could be reduced by an active measure such as a scanning wire [Bec+10] or magnetic pulses [Beh16]. In fig. 3.6 the neutrino mass sensitivity as a function of the rate at the tagger is plotted. It can be seen that rates below $\sim$ 10 kcps do not cause a significant loss of sensitivity.

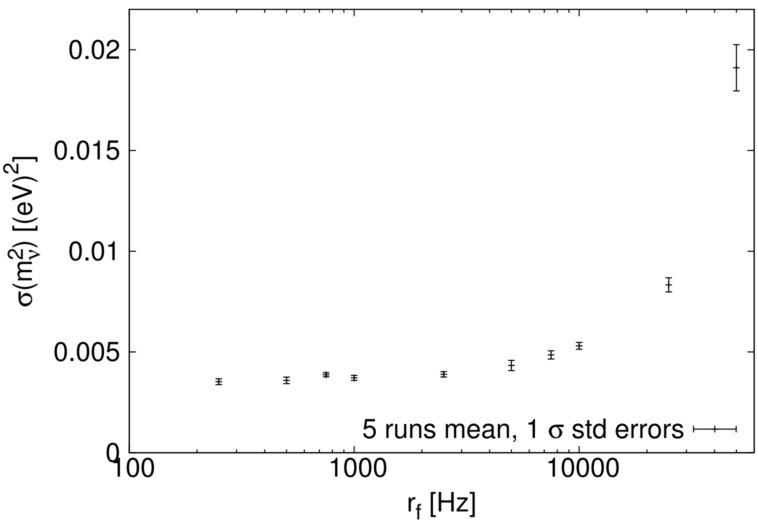

Figure 3.6: Statistical uncertainty of $m^2_{\nu_e}$ as a function of electron random trigger rate r_s. The results are based on a measurement time distribution of 2/3 and 1/3 of three years in total, assigned to 18565 eV and 18560 eV, respectively (optimum distribution for 18560 eV lowest retarding energy in Table 3.1). For each point the results from five simulation runs with identical parameters and different random numbers have been averaged. Other sources of background and time resolution have been neglected. Figure first published in [Ste+13].

3.3.3 Gated Filtering Technique

A method that has been discussed and successfully applied for TOF in the past is to periodically cut off the electron flux [Bon+99]. While it has been used previously as a band-pass filter, where all signals with a TOF outside a certain time window have been rejected and a classic, non-integrated beta spectrum has been measured, this technique might as well be applied for TOF spectroscopy. In the case of KATRIN, periodic filtering could be achieved by a high-frequency modulation of the source or the pre-spectrometer potential.

The principle in this case is to switch between two settings. In the first setting, a pre-spectrometer potential $q(U_{\mathrm{pre}} + \Delta U_{\mathrm{pre}}) > E_0$ is chosen to completely block the flux of β-electrons. In the other setting, the retarding potential of the pre-spectrometer is set to $qU_{\mathrm{pre}} < E_0 - \Delta E_{\mathrm{i}}$, leading to the full transmission of all electrons from the interesting energy region $[E_0 - \Delta E_{\mathrm{i}}, E_0]$, thus allowing to perform TOF spectroscopy (see fig. 3.7). The region of interest, which has a width ΔE_{i} of a few 10 eV, requires moderate switching voltages $\Delta U_{\mathrm{pre}} \approx -200$ V, taking into account the energy resolution of the pre-spectrometer of about 100 eV. While in [Bon+99] the source potential has been pulsed, in a dual spectrometer set-up like KATRIN it is thus more convenient to vary the retarding potential of the pre-spectrometer. This has the advantage that, in contrast to pulsing at the source, the potential setting which guarantees full transmission ("on", fig. 3.7) does not need to be set precisely but only significantly below the retarding energy of the main spectrometer minus the energy width of the pre-spectrometer.

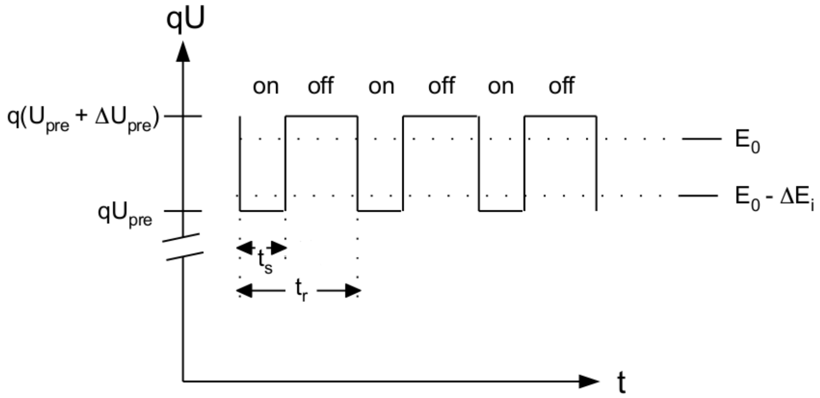

Figure 3.7: Timing parameters of the gated filter. X axis: time. Y axis: pre-spectrometer retarding potential. At the lower filter setting all electrons of the interesting region of width ΔE_{i} below the endpoint E_0 are transmitted while at the higher setting all electrons are blocked. Figure first published in [Ste+13].

Timing Parameters

A periodically gated flux can in the simplest case be described by two timing parameters. The first one is the period t_r with which the flux is gated. The second one is the time t_s in which the gate is open in each period. The ratio of t_s and t_r gives the duty cycle

$$\xi = \frac{t_s}{t_r}. \tag{3.21}$$

The arrival time spectrum with respect to the opening trigger of the gate is then measured at the focal plane detector and summed for all gating periods, giving the measured TOF spectrum. This method uses no direct measurement of the starting times but restricts them to certain intervals of length t_s. That is equivalent to knowing the starting time with an uncertainty of order t_s. Thus, for $t_s \longrightarrow 0$ and sufficient period lengths t_r, infinitesimally sharp starting times are obtained, but with infinitesimally low luminosity. If t_s is extended, the luminosity increases and the time uncertainty grows. The uncertainty is given by a uniform probability distribution in the interval $[0; t_s]$. The measured TOF spectrum is then given by the convolution with the detection time and the starting time distribution,

$$\left(\frac{\mathrm{d}N}{\mathrm{d}\tau}\right)_{t_s} = \frac{\mathrm{d}N}{\mathrm{d}\tau} \otimes N(\sigma_d) \otimes U(0, t_s), \tag{3.22}$$

where $N(\sigma_d)$ is the Gaussian uncertainty profile of the detection time at the detector and $U(0, t_s)$ the uniform uncertainty due to the gate. Since the measured TOF spectrum is the sum of all arrival time spectra for each individual gating period, all electrons with flight times longer than the period length, $\tau > t_r$, are measured at the detector in a later period. This results in a certain kind of pile-up, where these events give rise a non-isochronous background in the measured TOF spectrum. To account for these contributions, the measured TOF spectrum is given by a superposition of all contributing time distributions (3.22), shifted by multiples of t_r and cut off at 0 and t_r:

$$\left(\frac{\mathrm{d}N}{\mathrm{d}\tau}\right)_{t_s, t_r}(\tau) = \begin{cases} 0 & \tau < 0 \\ \sum_{n=0}^{\infty} \left(\frac{\mathrm{d}N}{\mathrm{d}\tau}\right)_{t_s}(\tau + n \cdot t_r) & 0 \leq \tau \leq t_r \\ 0 & \tau > t_r \end{cases} . \tag{3.23}$$

As $> 99.5\%$ of the flight times lie within $\lesssim 50\,\mu\mathrm{s}$ [3], all contributions with $n \cdot t_r \gtrsim t_s + 50\,\mu\mathrm{s}$ can be neglected.

Illustrative TOF spectra of simulated measurement data according to (3.23) are shown in fig. 3.8. The effects of the timing parameters t_r and t_s can be clearly seen. The uniform start time distribution within $[0, t_s]$, imposed on the spectrum by the uniform uncertainty (3.22), leads to a clear broadening of the shape. Since, in general, the opening time t_s is longer than the expected time resolution of an electron tagger, the broadening is more pronounced than in the tagger case. In addition, the convolution with the step function $U(0, t_s)$ leads to steeper edges than for a Gaussian uncertainty. The effects of pile-up for electrons with flight times $\tau > t_r$ can be seen as non-isochronous background tails in the beginning of the spectra. The effects of the timing parameters on the spectral shape allow some preliminary predictions with respect to the sensitivity:

- For constant t_s, reducing t_r will increase the duty cycle. However, more pile-up events from former gating periods enter the spectrum. Duty cycle and residual contributions need to be balanced.

- For constant t_r, reducing t_s will reduce the time uncertainty. In contrast, the duty cycle will be reduced, resulting in a lower count-rate. Here, the timing and the duty cycle need to be balanced.

Due to the trade-off between timing, duty cycle and residual background, the timing parameters need to be optimized. A global optimization of t_r and t_s has only shown a significant change in $\sigma_{\mathrm{stat}}(m^2_{\nu_e})$ for extreme input values. However, an combined optimization of t_s with the measurement time contribution for each retarding energy, given a fixed t_r, is reasonable. That is because the count-rate becomes lower at higher retarding potentials, while the neutrino mass information increases, which in general requires a larger duty cycle. Since the gated filter is less sensitive than a tagger, a higher number of retarding energies, covering a wider energy range, are necessary.

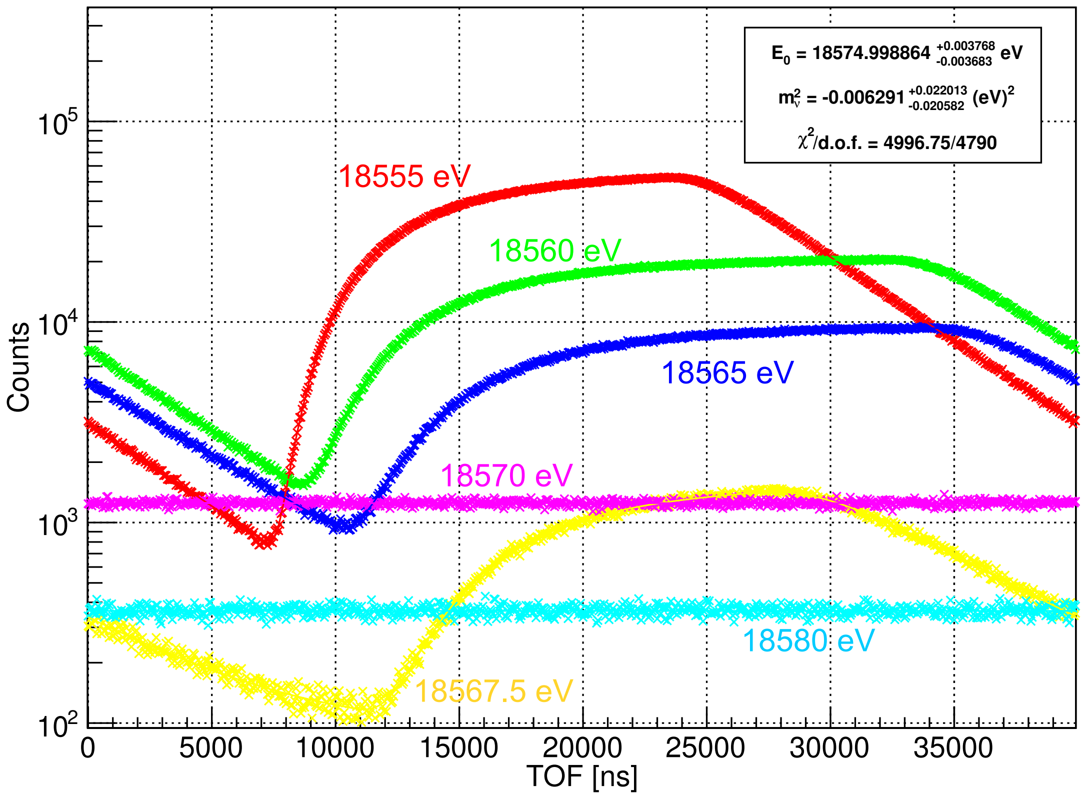

Figure 3.8: Example of simulated data of a TOF spectrum with a gated filter and fit. The colours correspond to the main spectrometer retarding energies. t_r is held constant at 40 μs while t_s and the measurement times per potential step have been chosen to match the optimal distribution stated in table 3.2. A total measurement time of three years has been assumed. On the left side of the spectrum the residuals from earlier cycles can be seen which emerge continuously from the end of the spectrum. The peaks exhibit effects of the convolution with the uniform start time distribution. For retarding energies of 18570 eV and 18580 eV the gated filter was always open ($t_s = t_r$) yielding time-independent count numbers. The other parameters in the simulation were $b_0 = 10^{-2}$/s, $E_0 = 18\,575.0$ eV and $m^2_{\nu_e} = 0$. Figure first published in [Ste+13].

Table 3.2: Average statistical uncertainty $\langle \sigma_{\mathrm{stat}}(m^2_{\nu_e}) \rangle = \langle \frac{1}{2}(|\Delta m^2_{\nu_{e-}}| + |\Delta m^2_{\nu_{e+}}|) \rangle$ (arithmetic mean of positive and negative error of 10 simulations and fits), average fit parameters $\langle E_0 \rangle$ and $\langle m^2_{\nu_e} \rangle$, as well as average Pearson's correlation coefficient $\langle R(E_0, m^2_{\nu_e}) \rangle$ between endpoint and squared neutrino mass for uniform and optimized distribution of a gated filter setup. Assumed are three years measurement time with $m^2_{\nu_e} = 0$, $E_0 = 18\,575.0$ eV and $qU = 18555$ eV as lowest retarding energy. The pulse period t_r was held constant at 40 μs. Results first published in [Ste+13].

(duty cycle t_s/t_r, measurement time fraction) at qU =						$\sigma_{\mathrm{stat}}(m^2_{\nu_e})$	$\langle E_0 \rangle$	$\langle m^2_{\nu_e} \rangle$	$\langle R \rangle$
18555 V	18560 V	18565 V	18567.5 V	18570 V	18580 V	(eV^2)	(eV^2)	(eV)	
(0.5, $\frac{1}{6}$)	(0.5, $\frac{1}{6}$)	(0.5, $\frac{1}{6}$)	(0.5, $\frac{1}{6}$)	(0.5, $\frac{1}{6}$)	(0.5, $\frac{1}{6}$)	0.025	18574.9983	-0.0056	0.9230
(0.4, $\frac{1}{13}$)	(0.6, $\frac{1}{13}$)	(0.6, $\frac{2}{13}$)	(0.4, $\frac{1}{13}$)	(1.0, $\frac{4}{13}$)	(1.0, $\frac{4}{13}$)	0.021	18575.0006	0.0049	0.8914

Results

The results of a rough optimization run with 6 retarding potentials, giving 12 free parameters, are shown in table 3.2. The highest retarding energy has been chosen to be above E_0 and is thus sensitive to the background level. Starting with $\xi = 0.5$ and a uniform distribution, each parameter has been scanned successively and set to the position of the local minimum. This has been repeated until the improvements per iteration are sufficiently small. The optimum has been found after 5 iterations. It can be seen that the optimization of duty cycles and measurement times provides an improvement of $\sim 20\ \%$ compared to the uniform distribution with $\xi = 0.5$. The obtained result of $\sigma_{\mathrm{stat}}(m^2_{\nu_e}) = 0.021\,\mathrm{eV}^2$ is nearly identical with the standard KATRIN value of $\sigma_{\mathrm{stat}}(m^2_{\nu_e}) = 0.020\,\mathrm{eV}^2$ for the case of 20 eV difference between endpoint and lowest retarding energy. It remains open if a more detailed parameter optimization is able to increase the sensitivity.

3.4 Experimental Tests of the TOF Model

The TOF model as described by eq. (3.5) has been put to test experimentally during the KATRIN commissioning measurement phases SDS I and SDS II [Beh16; Gro15]. While the basic equation is analytical, the model is based on some assumptions, foremost the adiabatic motion of the electrons, and uses simulated field maps for $U(z)$ and $B(z)$ on basis of a simplified geometry. Furthermore, it is useful to have some kind of preliminary test of TOF under experimental conditions in order to find out and eliminate some possible error sources that could be problematic under a later electron tagger or gated filter setup.

In order to have a defined calibration source, a pulsed, angular selective and mono-energetic electron source (e-gun) [Beh+17][4] has been used. The setup is illustrated in figure 3.9. The e-gun consists of two stainless steel plates with a distance $d = 10\,\mathrm{mm}$, mounted in a Faraday cage with an aperture in forward-beam direction. The photocathode is located at the emission spot p_e on the back plate. It consists of a thin gold or silver layer which is back-illuminated with UV light using a $\varnothing = 200\,\mathrm{mm}$ optical fiber. If the wavelength of the UV light exceeds the effective work function of the photocathode, photoelectrons are emitted. They have a small initial kinetic energy of $< 0.1\,\mathrm{eV}$ and are accelerated to their full kinetic energy by the negative potential of the backplate U_{egun}. A second acceleration is locally induced by front plate, which is on a more positive potential $U_{\mathrm{egun}} + U_{\mathrm{acc}}$ and has an aperture of radius $r_{\mathrm{afp}} = 3\,\mathrm{mm}$, in order to create a defined starting angle. The setup is mounted upstream in front of the spectrometer entrance magnet. A non-zero starting angle can be imposed on the electrons by tilting the cage against the z axis with an angle α_{p} due to the non-adiabatic acceleration of the electrons by the front plate, whose momentum is then tilted against the magnetic field lines.

The UV light is provided by two possible light sources. The first option is a frequency coupled Nd:YVO_4 laser, which emits UV light at a wavelength of 266 nm with 1 nm FWHM and provides a high output power of 10 mW at maximum. The laser is operated in pulsed mode, where the frequency can be set between 40 kHz and 100 kHz. Nominally, it has a pulse width of $< 20\,\mathrm{ns}$, which provides sharp starting times for TOF measurements. The combined width of the laser pulse and the detector time resolution has been measured during the commissioning phase with a result of $\sim 80\,\mathrm{ns}$. The second option uses an array of six UV LEDs with peak wavelengths between 265 nm and 315 nm. Via an UV monochromator

[3] under the condition that the retarding potential is at least some eV below the endpoint

[4] For previous developments, see [Bec+14; Val+11].

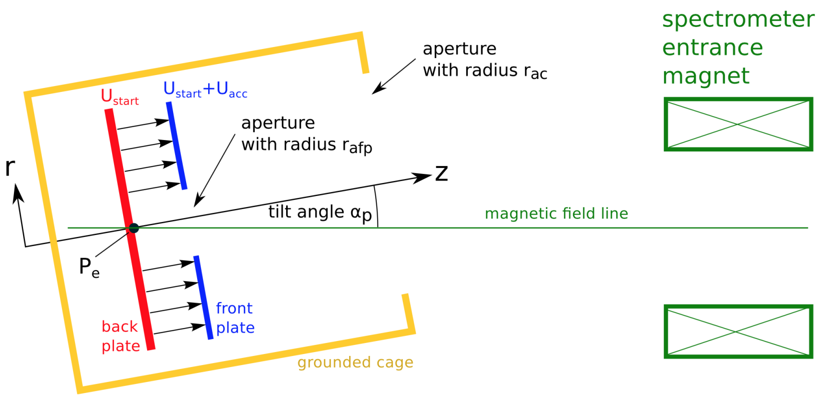

Figure 3.9: Schematic view of the e-gun. Electrons are created via the photoelectric effect at the emission spot p_e and accelerated towards the main spectrometer by a positive potential $U_{\text{start}} + U_{\text{acc}}$ on the front plate. The e-gun can be tilted against the magnetic field lines, giving the photoelectrons a defined starting angle. Figure from [Beh+17].

with 4 nm FWHM a sharp line width is achieved. The LED can be pulsed using a function generator to achieve pulse lengths > 100 ns for TOF measurements. For a synchronization of the start pulses and the detector clock, the sync output of the pulser was connected to the DAQ of the detector using a 60 m BNC cable, a pre-scaler and a TTL-OPT converter. Each of these components impose an additional delay, where the cable contributes with ~ 350 ns, the pre-scaler with ~ 450 ns, the TTL-OPT converter with ~ 100 ns and the shaping time offset amounts to ~ 400 ns. This gives a total latency of ~ 1.3 µs.

To test the TOF model (3.5), various measurements have been conducted with the aim of measuring the peak TOF as a function of the surplus energy of the e-gun $q(U_{\text{egun}} - U_{\text{IE}})$, where U_{IE} denotes the potential at the inner electrode. The energy spectrum emitted by the e-gun is not perfectly monochromatic, but follows the photoelectric distribution derived by Fowler [Fow31] with a width of ~ 300 meV [Beh+17]. Therefore, the arrival time distribution measured by the FPD is not perfectly sharp, but has a certain width and asymmetry which both become smaller with increasing surplus energy, since TOF differences are generally smaller for higher kinetic energies. Furthermore, the pulse width of the LED and the laser, respectively, and the detector time resolution of ~ 50 ns lead to a further broadening of the arrival time distribution. In order to compare the measurements to the prediction by (3.5), the arrival time spectra have been fitted by a Gaussian, where the mean gives the peak arrival time (figure 3.10). This is a simplified approach and has some shortcomings, especially since the arrival time distribution is asymmetric. For a correct analysis, the TOF spectrum of the photoelectrons would have to be numerically calculated via (3.8), given the Fowler energy distribution. However, for the principle study of the TOF model, this simple approach is sufficient, since we are only interested if the model describes the functional dependency between TOF and energy correctly within the limits defined by the energy spread of the e-gun, the time width of the pulsed UV source and the FPD, respectively. Since the pulse frequency is 100 kHz for all measurements, a detector trigger event is received every $t_r = 10$ µs, simultaneously with each e-gun pulse. Thus, the difference between trigger event and measured arrival time corresponds to the TOF modulo the trigger repetition time t_r, yielding a periodic arrival time spectrum. In order to reconstruct the mean TOF from the peak arrival time, a cycle correction has been applied, where for each fitted peak TOF at a given surplus energy $q(U_{\text{egun}} - U_{\text{IE}})$ a certain multiple of the trigger repetition time, $n \cdot t_r$ with

$n \in \mathbb{N}^0$, has been added in such a way that the resulting curve is continuous. The Gaussian fits and cycle correction have been automated via the analysis software BEANS [Eno].

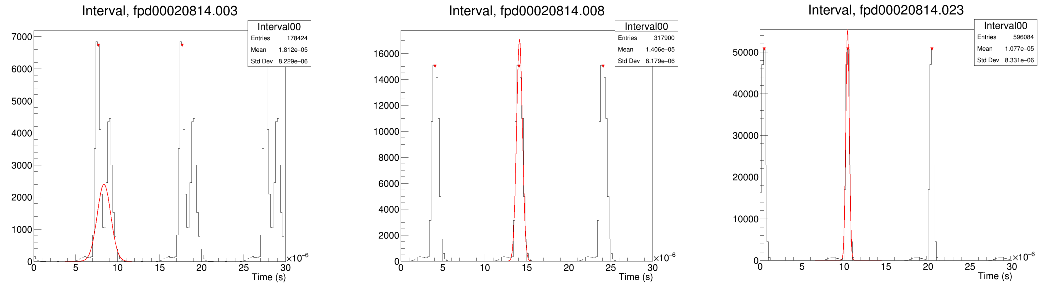

Figure 3.10: Gaussian fit example of measured arrival time spectra of run no. 20814 at surplus energies $q(U_{\text{egun}} - U_{\text{IE}})$ of 10 eV (left), 20 eV (middle) and 50 eV (right). The arrival time spectrum modulo the trigger repetition time of $t_\text{r} = 10\,\mu\text{s}$ has been duplicated two times to have at least one continuous peak in every case. To each fitted mean, a multiple of the trigger repetition time, $n \cdot t_\text{r}$, has been added in such a way that resulting functional dependency between measured TOF and surplus energy is continuous. For increasing surplus energy, the peak width and the asymmetry become smaller. At lower retarding energies, a double peak structure of unknown origin can be seen (left).

The resulting data points, given by the cycle corrected peak arrival time as a function of the surplus energy, have been fitted by (3.5), where both a TOF offset, $\Delta\mathcal{T}$, and an energy offset, ΔE have been set as free parameters. This is necessary since both the absolute energy and the absolute arrival time are not perfectly calibrated. In case of the energy, three major effects contribute to a fit offset:

- The backplate of the e-gun is connected to the high voltage of the main spectrometer with a small difference voltage which is given by a power supply operating from 0 kV to −1.25 kV plus a battery with a positive voltage of ∼ 90 V [Beh+17]. This setup allows to cancel high voltage fluctuations, since only the stability of the difference voltage is significant for the precision of the surplus energy. The battery offset shifts over a longer period of time, which can amount a deviation of some V from the nominal value. This bias is the dominating contribution to ΔE. Since for e-gun measurements the absolute energy calibration is not relevant but rather the energy difference with respect to the transmission edge, this is no real disadvantage.

- The retarding potential in the analyzing plane is defined by the potential of the inner electrode (IE) at outer radii, but is slightly more positive towards the central axis. This potential depression ΔU_{ana} amounts to a few eV at maximum.

- The average initial energy of the photoelectrons after leaving the photocathode is given by the difference between the photon energy $2\pi/\lambda$ and the effective work function of the material Φ.[5] The effective work function has been determined in [Beh+17], stating $\Phi = 3.78(4)$ eV. For the available UV sources of the e-gun, this amounts to a maximum average initial energy of ∼ 0.9 eV at 266 nm.

For the arrival time offset, contributions are possibly given by the calibration of the trigger delay and small differences between the simulation geometry and the measurement

[5]Note that natural units have been used, otherwise the photon energy is defined by hc/λ.

geometry. Furthermore, as the e-gun is not perfectly monochromatic and since the dependency between energy and TOF is non-linear (3.5), the fitted peak arrival time does not necessarily correspond exactly to the actual surplus energy, but only within those limits given by the energy distribution. This can possibly also result in a global contribution to the fitted offsets $\Delta\mathcal{T}$ and ΔE.

The y axis error bars in the plots of arrival time versus surplus energy have been defined by

$$\delta\tau = \sqrt{\delta\tau_0^2 + \delta\tau_1^2 + \delta\mathcal{T}^2(\delta\epsilon)}\,, \tag{3.24}$$

where $\delta\tau_0$ is given by the Gaussian fit uncertainties of the arrival time distributions, $\delta\tau_1$ is a fixed systematic uncertainty and $\delta\mathcal{T}(\delta\epsilon)$ an energy-dependent uncertainty, given by the TOF difference corresponding to a systematic uncertainty of the surplus energy $\delta\epsilon$ as

$$\delta\mathcal{T}(\delta\epsilon) = \mathcal{T}(\epsilon) - \mathcal{T}(\epsilon - \delta\epsilon)\,, \tag{3.25}$$

where $\epsilon = q(U_{\mathrm{IE}} - U_{\mathrm{egun}} - \Delta E)$ stands for the corrected surplus energy. The energy dependent error component has been introduced, since, at lower surplus energies, small energy differences lead to higher TOF differences. There is no satisfying way of fixing $\delta\tau_1$ and $\delta\epsilon$ a priori. However, the choices $\delta\tau_1 = 20$ ns and $\delta\epsilon = 20$ meV have shown to fit the data well. These choices are plausible insofar as the LED pulse rise and fall times are 20 ns each and the nominal pulse width of the laser is < 20 ns, respectively. While global shifts of the arrival time are accounted for by the free parameter $\Delta\mathcal{T}$, it makes sense to assume that there are still local shifts in that order of magnitude in addition to the random fluctuations that define the Gaussian fit uncertainty $\delta\tau_0$. The error of the surplus energy has been estimated to be ~ 60 meV in [Beh+17], however since global shifts of the surplus energy are absorbed in the fitted offset ΔE, a remaining value of $\delta\epsilon = 20$ meV can well correspond to a random uncertainty of the surplus energy setting.

Results

Figures 3.11 – 3.15 show the fit results of data from five different runs. While there have been taken TOF data for every measurement with a pulsed e-gun, only these measurements have been suitable for a fit by the model (3.5), due to insufficient data quality and a low number of measurement points at higher surplus energies. The parameters for each run can be found in table 3.3. Within these runs, a lower fit interval has been defined in a way that the data points selected for a fit by (3.5) meet the following conditions:

- The surplus energy has to be sufficient that at the measured electron rate is at least 50 % of the nominal rate in full transmission. Otherwise the arrival time peaks are overly broad, which leads to pile-up and failure of peak identification.
- The Gaussian fit of the peak arrival time has to be successful in that it returns finite parameter errors.
- Some of the measured TOF spectra show a double-peak structure mostly at surplus energies of $\sim 5 - 20$ eV (e.g., see figure 3.10, left). The source of the behavior is unclear. Since the transmission function is flat in the affected region for all runs, additional components in the energy distribution can be excluded. The most likely explanation would be that parts of the beam undergo some early retardation inside or after leaving the e-gun. However, it is beyond the scope of this analysis to determine the exact

Table 3.3: Run parameters for all runs in figures 3.11 – 3.15.

measurement phase	run number	light source	pulse width	α_p	U_{IE}	U_{acc}	air-coil setting
SDS I	5839	laser (266 nm)	< 20 ns	0°	−200 V	50 V	5 G
SDS I	6123	LED (290 nm)	100 ns	0°	−200 V	50 V	9 G
SDS I	6157	LED (290 nm)	100 ns	0°	−200 V	50 V	3.8 G
SDS II	20814	LED (275 nm)	500 ns	0°	−200 V	100 V	3.8 G
SDS II	20815	LED (275 nm)	500 ns	15°	−200 V	100 V	3.8 G

source. Therefore, only data sets without any hints of a double peak-structure have been selected for the fit.

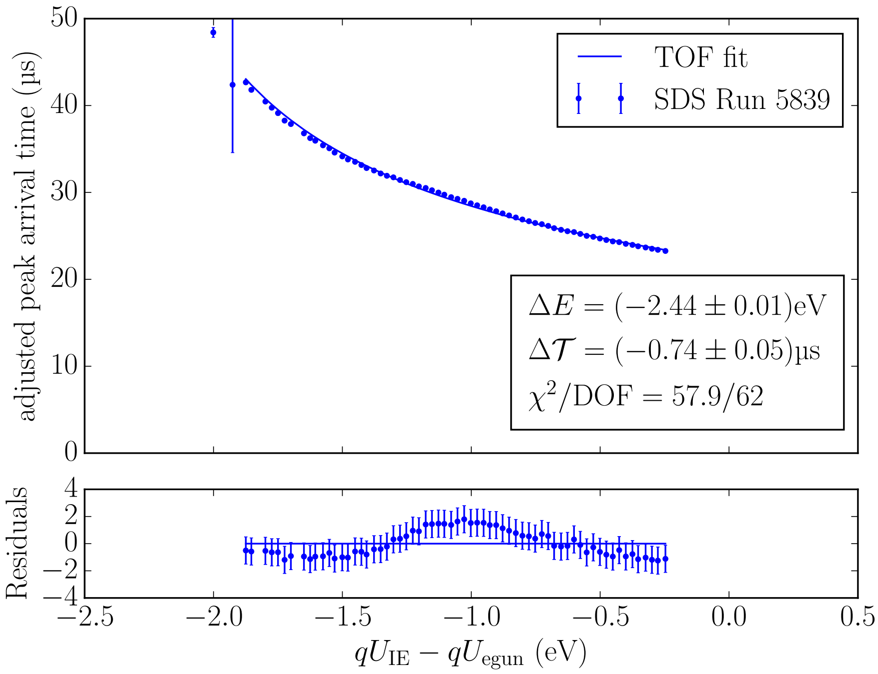

Figure 3.11: Fit of time-of-flight data of run no. 5839 (SDS I) with the model (3.5). The data have been taken at low surplus energies. Deviations between data and fit can most likely be explained by the asymmetry of the arrival time spectra and medium-scale fluctuations of the surplus energy. Full run parameters can be found in table 3.3.

Under these quality criteria, all data can be reproduced considerably well by (3.5). However, it can be seen from in figures 3.11 – 3.15 that the agreement is not perfect insofar as certain trends are present in the residuals. Some explanations are possible. Most likely, some deviations arise from the energy distribution of the e-gun, leading to an arrival time distribution which becomes broader and more asymmetric at lower surplus energies, which gives rise to a larger deviation between theoretical TOF and fitted peak value. This can only partly be mitigated by the free parameters ΔE and $\Delta\mathcal{T}$ on small scales (see, e.g., run 5839, fig. 3.11, where the fit reproduces the data largely well on a small energy interval at low surplus energy). A further source of discrepancy could be the observed double-peak structure in some arrival time distributions. Although the lowest fit interval has been defined in such a way that all data sets where this feature is visible have been rejected, it is possible that there are still subtle contributions in a few data sets above that threshold. This offers a likely

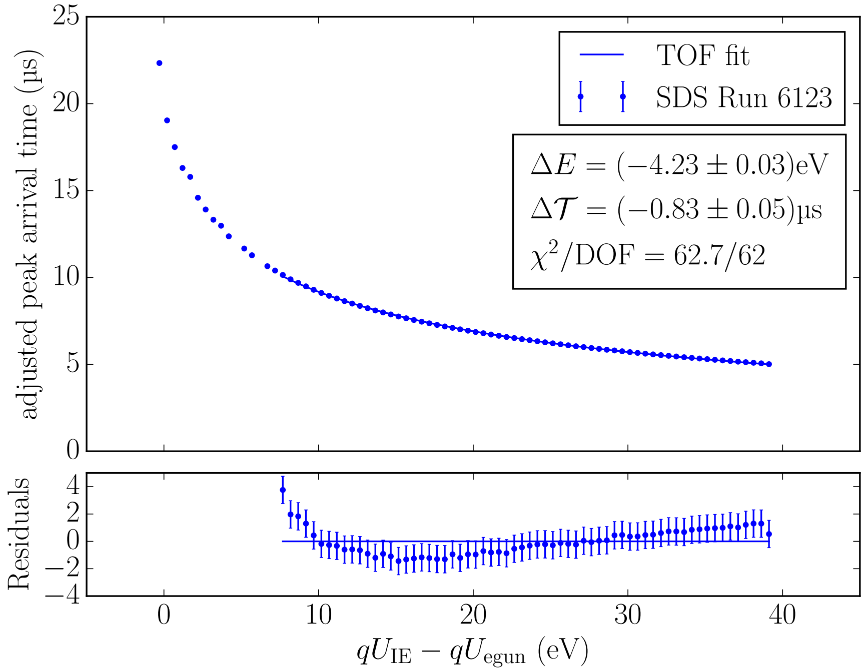

Figure 3.12: Fit of time-of-flight data of run no. 6123 (SDS I) with the model (3.5). Data have been taken at higher surplus energies. Deviations between data and fit increase with lower retarding potential most likely due to a higher asymmetry and unexplained double-peak structure of the arrival time spectra. Full run parameters can be found in table 3.3.

explanation especially for the deviations near the low surplus energies in runs 6123 and 6157 (figures 3.12 and 3.13) but also in runs 20814 and 20815 (figures 3.14 and 3.15), where the fit interval has been restricted due to visible double-peak structures. At lower surplus energies, deviations could be caused by correlated fluctuations of the surplus an energy scale of order $\sim$ eV, as for instance in run 5839 (figure 3.11). Therefore, neighboring points are correlated and the fluctuations can not be accounted for by the random surplus energy uncertainty δE. Such a structure can also be seen in the residuals from run 6157 (figure 3.13), which has been performed with a high density of data points, but due to higher surplus energies the fluctuations are smaller than the error bars. In addition, it can be observed in some of the runs that the data point with the highest surplus energy shows a slightly shifted peak arrival time. The reason for that behavior is unclear, but it can possibly be attributed to a bug in the ORCA run script.

The fitted TOF offsets $\Delta\mathcal{T}$ are below 1 µs for all runs (table 3.4). It can be seen that the remaining offset is between ~ -0.75 and -0.85 µs for the SDS I runs, as well as ~ -0.75 and -0.85 µs for the SDS II runs. In general, the delay of the trigger system has been corrected in the data. In run SDS I, there has been a calibration error of the triggering system amounting to an offset of $\sim$ 5 µs. This has been corrected in the data as well. However, including this correction, it might be possible that the total correction does not fit the data precisely, leading to a different offset compared with the later runs from phase SDS II. Additional sources for the remaining offset can be, e.g., a small mismatch of simulation and measurement geometry, uncertainty in the calibration or a global uncertainty of the method due to the energy distribution of the e-gun.

The only run with a non-zero e-gun polar angle α_p has been run 20815 with $\alpha_p = 15°$.

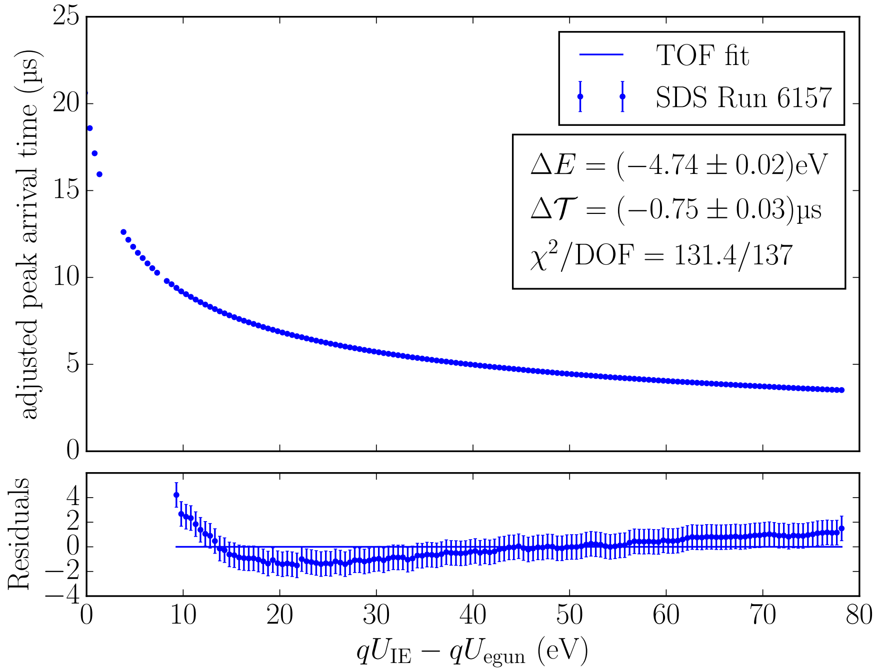

Figure 3.13: Fit of time-of-flight data of run no. 6157 (SDS I) with the model (3.5). The run has been a long-term run with a larger number of data points including particularly high surplus energies. Deviations between data and fit increase with lower retarding potential most likely due to a higher asymmetry and unexplained double-peak structure of the arrival time spectra. Due to the high number of data points, correlated medium-scale fluctuations of the surplus energy can be observed in the residuals, which are, however, small due to the high surplus energies. Full run parameters can be found in table 3.3.

However, the differences to the run 20814 with the same parameters except a polar angle $\alpha_p = 0$ are vanishing, since the runs have been taken with an inner electrode potential of $U_{\mathrm{IE}} = -200$ V, where the energy resolution of the MAC-E-Filter (2.7) is significantly sharper and thus also electrons with larger starting angles have nearly parallel momentum in the analyzing plane. There have been a few runs with a more negative inner electrode potential, however, the data quality was too low for a TOF fit.

3.5 Conclusion and Outlook

A TOF spectroscopy mode could in principle provide significant improvements in the statistical neutrino mass sensitivity compared to a standard MAC-E-Filter mode. The study especially revealed the following information.

- In the standard mode it is necessary to measure at lower retarding potentials, for instance at KATRIN down to 30 eV below the endpoint, with a large number of measurement points.
- Using a TOF mode in contrast, it is sufficient to consider two or more retarding potentials only which may be even more close to the endpoint while improving the statistical uncertainty.

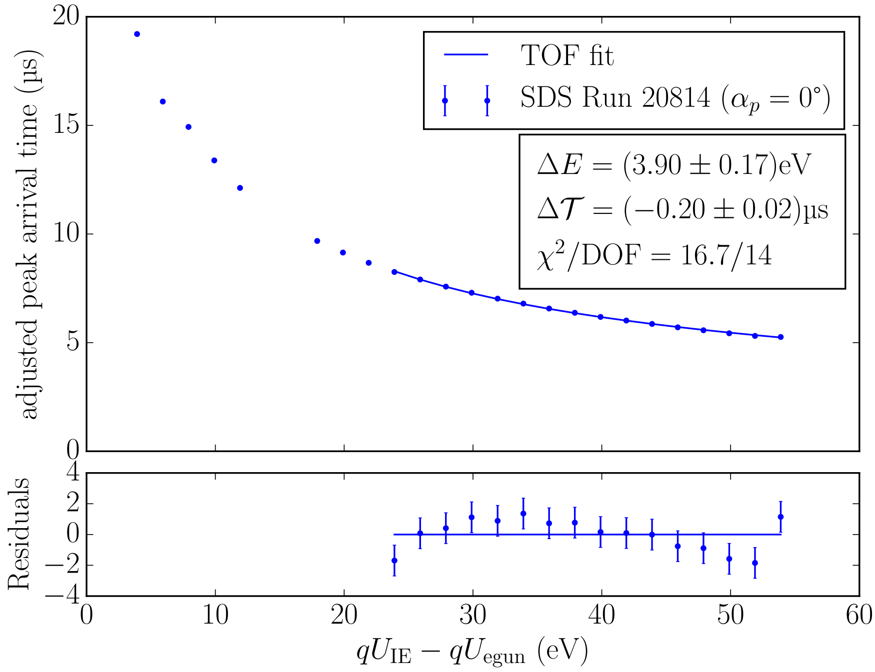

Figure 3.14: Fit of time-of-flight data of run no. 20814 (SDS II) with the model (3.5). Data have been taken at larger surplus energies. Full run parameters can be found in table 3.3.

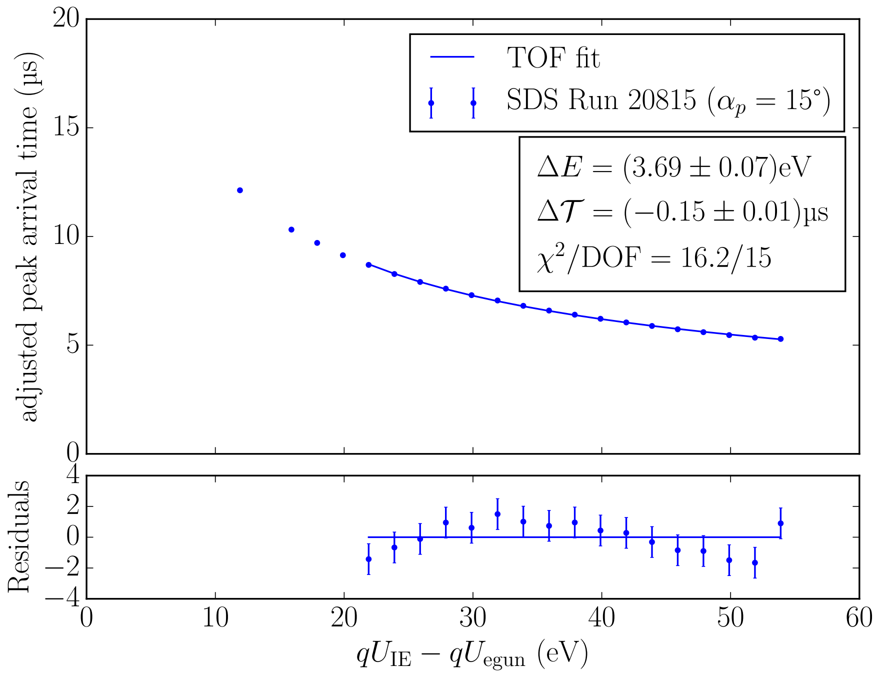

Figure 3.15: Fit of time-of-flight data of run no. 20815 (SDS II) with the model (3.5). Data have been taken at larger surplus energies. The parameters are identical with those of run no. 20814, except an e-gun polar angle of $\alpha_\text{p} = 0°$. Full run parameters can be found in table 3.3.

Table 3.4: Fitted arrival time offsets $\Delta\mathcal{T}$ and fit intervals for all measurements in figures 3.11 – 3.15. The absolute values of the fit interval limits have been corrected by the fitted energy offset ΔE.

measurement phase	run number	min. fitted surplus energy	max. fitted surplus energy	$\Delta\mathcal{T}$
SDS I	5839	~ 0.6 eV	~ 2.8 eV	(-0.74 ± 0.05) µs
SDS I	6123	~ 11.9 eV	~ 43.4 eV	(-0.83 ± 0.05) µs
SDS I	6157	~ 14.0 eV	~ 82.9 eV	(-0.75 ± 0.03) µs
SDS II	20814	~ 20.0 eV	~ 50.0 eV	(-0.20 ± 0.02) µs
SDS II	20815	~ 18.2 eV	~ 50.2 eV	(-0.15 ± 0.01) µs

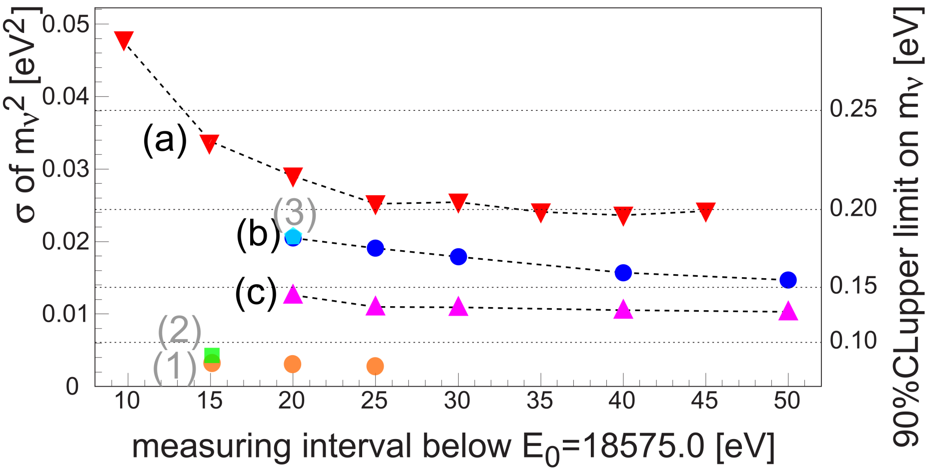

Figure 3.16: Statistical uncertainty $\sigma_{\text{stat}}(m^2_{\nu_e})$ (3 years measurement time) and corresponding 90 % C.L. upper limit on m_{ν_e} as a function of the analyzed interval for different configurations of standard and TOF mode. Standard mode: (a) uniform measurement time; (b) optimized measurement time; (c) optimized measurement time, but background rate $b = 1$ mcps instead of 10 mcps as for (a) and (b). Results (a)-(c) and figure adapted from [KAT04]. TOF spectroscopy (this work): (1) optimized measurement time, no background and infinite time resolution; (2) same as (1) for one examplary measurement interval with a non-zero background rate $b = 10$ mcps; (3) gated filter with optimized measurement time and optimized duty cycle again for one examplary measurement interval. Since it is well-known (e.g. [KAT04]) that the systematic uncertainties increase with increasing measurement interval below the endpoint E_0, the time-of-flight spectroscopy simulations have been concentrated to short measurement intervals, because otherwise any improvement in statistics might be overruled by systematic uncertainties.

- This suggests that even the systematic uncertainty can be reduced with a TOF mode as the systematics grow with lower retarding potentials.

The underlying model has successfully been put to test in the commissioning measurement phases SDS I and SDS II. For a quantitative analysis of the improvement potential of the TOF mode relative to the standard mode one may consider fig. 3.16, where the statistical uncertainty of $m^2_{\nu_e}$ is plotted as a function of the measurement interval below the endpoint E_0 (difference between lowest retarding potential and the endpoint E_0 using $E_0 = 18.575$ keV). Compared with the reference value of KATRIN, $\sigma_{\text{stat}}(m^2_{\nu_e}) = 0.018\,\text{eV}^2$ (see figure 3.16 curve (b) for measurement interval of 30 eV), a statistical improvement of up to a factor 5 is possible in the optimal case (fig. 3.16 (1)), equivalent to a factor of more than 2 in statistical sensitivity of m_{ν_e}. It can be shown (compare the difference in fig. 3.16 between curves (b) and (c) w.r.t. point (2)) that this improvement factor is essentially not caused by neglecting the background but by intrinsic advantages of the method itself. A total improvement factor needs to take the systematics into account, which may only be simulated precisely if the measurement method is sufficiently known. This is especially true since both systematic and statistical uncertainty depend on the choice of retarding potentials, where an optimal trade-off has to be found.

Considering the measurement method, up to now no technique has been demonstrated that would allow a highly precise determination of the time-of-flight of the electrons without disturbing their energy significantly. However, there is no fundamental obstacle to a measurement of this kind, and the main difficulty is one of extracting a sufficient and controlled amount of energy from the electron in flight. If such a method existed, it would have the advantage of being not only a very sensitive implementation of the TOF mode, but also could significantly suppress backgrounds, depending on the total signal rate.

The method of a periodic gate, which has been tested in the context of the Mainz experiment [Bon+99], may be applied to TOF spectroscopy. The simulations, using a rough parameter optimization, show that its sensitivity is comparable with the standard MAC-E mode (fig. 3.16 point (3) and curve (b)). Hence, whether a TOF mode based on gated filtering is an improvement depends mainly on how the systematic uncertainty of that method compares with that of the standard method. In conclusion, future studies of the TOF method should both concentrate on the efforts towards a working electron tagger and a detailed investigation of the systematics with TOF spectroscopy.

Chapter 4

keV Sterile Neutrino Sensitivity

The results of this chapter have been submitted to EPJ C in edited form and are available as e-print [Ste+17a] as of the publication date of this thesis. The chapter is based on the original draft, written by myself.

As a large-scale experiment with high source luminosity and a high energy resolution, it is worthwhile to explore the prospects of setting new limits on models beyond the standard model with KATRIN. A fruitful opportunity is the search for sterile neutrinos (section 1.5) due to their assumed mixing with the electron neutrino. Sterile neutrinos can show a discontinuity in the β-decay spectrum if they have a sufficiently large mixing angle with electron neutrinos. There has been some previous work on sterile neutrinos in general in tritium β-decay. Most publications focus on eV scale sterile neutrinos [FB11; SH11; Kra+13], where KATRIN is able to resolve the full parameter space of the reactor antineutrino anomaly (see section 1.5.2). However, the concept of sterile neutrinos in the keV range as candidates for warm dark matter (section 1.5.3) has received particular attention in the community for some years [Dre+17]. The most stringent limits on the mass and the mixing angle result from astrophysical experiments, mainly satellite-based searches for sterile neutrino X-ray decay lines (e.g., [Boy+06; WLP12]). Tritium β-decay experiments are ideal ground-based experiments for the purpose of testing the sterile neutrino hypothesis in the keV range [Veg+13]. Limits for sterile neutrino masses between $m_h = 0.1$ and $m_h = 2\,\text{eV}$ have recently been published by the Troitsk collaboration [Ase+11]. Upcoming experiments like KATRIN and ECHo have the possibility to increase the current lab-based limits significantly [Mer+15a].

In order to adapt KATRIN, which is optimized for light neutrinos of $m_l \lesssim O(\text{eV})$, for keV sterile neutrinos, different approaches are discussed with the goal of enhancing statistics and managing systematics. Promising ideas are in particular to develop a dedicated detector measuring in differential mode [Mer+15a] and to adapt advanced analysis techniques [Mer+15b]. However, in order to explore various ideas it may also be worthwhile to study the performance of an alternative time-of-flight (TOF) mode, which has already shown promising in theory for active neutrino mass measurements, as shown in the last chapter. In this chapter the sensitivity of a keV scale sterile neutrino search based on TOF spectroscopy with the KATRIN experiment is discussed both for an ideal measurement method as for a gated filter (section 3.3.3) with minimal hardware modifications. Due to high count rates of up to 10^{11} cps when using KATRIN for a measurement of keV scale sterile neutrinos, an alternative Monte Carlo simulation approach based on importance sampling has been developed for a correct and efficient sensitivity estimation (section 4.2). The results of this investigation are prepared for submission [Ste+17a].

4.1 Sterile Neutrino Search with TOF Spectroscopy

4.1.1 Sterile Neutrinos in Tritium β-Decay

A detailed study of the tritium β-spectrum with keV scale sterile neutrinos, including detailed contributions on systematics and theoretical corrections, can be found in refs. [Mer+15a] and [Dre+17]. In this section, the first-order signature of a sterile neutrino in the β-spectrum will be derived and discussed, before proceeding to the specifics of a sterile neutrino search using TOF spectroscopy.

The tritium β-spectrum for a superposition of mass eigenstates m_i is given in eq. (2.1). For the following derivation, the β-spectrum component for a single given mass state m_i is defined as

$$\begin{aligned} \frac{\mathrm{d}\Gamma}{\mathrm{d}E}(m_i) &= N\frac{\mathrm{G}_\mathrm{F}^2}{2\pi^3}\cos^2(\theta_\mathrm{C})|M_\mathrm{nucl}|^2\, F(E,Z')\cdot p\cdot(E+m_\mathrm{e}c^2) \\ &\cdot\sum_j P_j\cdot(E_0-V_j-E)\cdot\sqrt{(E_0-V_j-E)^2-m_i^2\mathrm{c}^4}, \end{aligned} \tag{4.1}$$

where all symbols are defined identically with (2.1).

As outlined in section 2.1.1, the electron neutrino is a superposition of multiple mass eigenstates. Since the flavor eigenstate is the one which defines the interaction, but the mass eigenstate the one which describes the dynamics of the decay, the β-spectrum for the electron neutrino is an incoherent superposition of the contributions for each mass eigenstate,

$$\frac{\mathrm{d}\Gamma}{\mathrm{d}E}(m_{\nu_\mathrm{e}}) = \sum_{i=1}^{3}|U_{\mathrm{e}i}|^2\frac{\mathrm{d}\Gamma}{\mathrm{d}E}(m_i)\,. \tag{4.2}$$

In case of an additional keV scale sterile neutrino, a fourth mass state m_4 is introduced with a significantly lower mixing with the electron neutrino, $|U_{\mathrm{e}4}|^2 \ll |U_{\mathrm{e}i}|^2$ ($i \in 1,2,3$). In the following we define the *heavy* or sterile neutrino mass as $m_h \equiv m_4$ and the *active sterile mixing angle* as $\sin^2\theta \equiv |U_{\mathrm{e}4}|^2 \lesssim 10^{-7}$ [WLP12]. The light mass eigenstates 1, 2, 3, which are not distinguishable by KATRIN, can then be approximated according to (2.3) to define the *light neutrino mass* as $m_l^2 \equiv \sum_{i=1}^{3}|U_{\mathrm{e}i}|^2 m_i^2$. The combined β-spectrum with sterile and active neutrino can then be expressed as

$$\frac{\mathrm{d}\Gamma}{\mathrm{d}E}(m_{\nu_\mathrm{e}}) = \sin^2\theta\frac{\mathrm{d}\Gamma}{\mathrm{d}E}(m_h) + \cos^2\theta\frac{\mathrm{d}\Gamma}{\mathrm{d}E}(m_l)\,. \tag{4.3}$$

A plot with exemplary parameters can be found in figure 4.1.

4.1.2 Sterile Neutrino Search with Time-of-Flight Spectroscopy

In contrast to the standard mode of operation, using TOF spectroscopy one would be able to measure not only the count-rate, but a full TOF spectrum at a given retarding potential qU, as discussed in detail in chapter 3. To recapitulate, the TOF spectrum can be derived by transformation of the double differential event rate $\frac{\mathrm{d}^2N}{\mathrm{d}\vartheta\,\mathrm{d}E}$ as function of the starting energy E and starting angle ϑ, eq. (3.8), where the TOF as function E and ϑ is given by (3.5). The double differential event rate $\frac{\mathrm{d}^2N}{\mathrm{d}\vartheta\,\mathrm{d}E}$ itself can be derived from the β-spectrum $\mathrm{d}\Gamma/\mathrm{d}E$

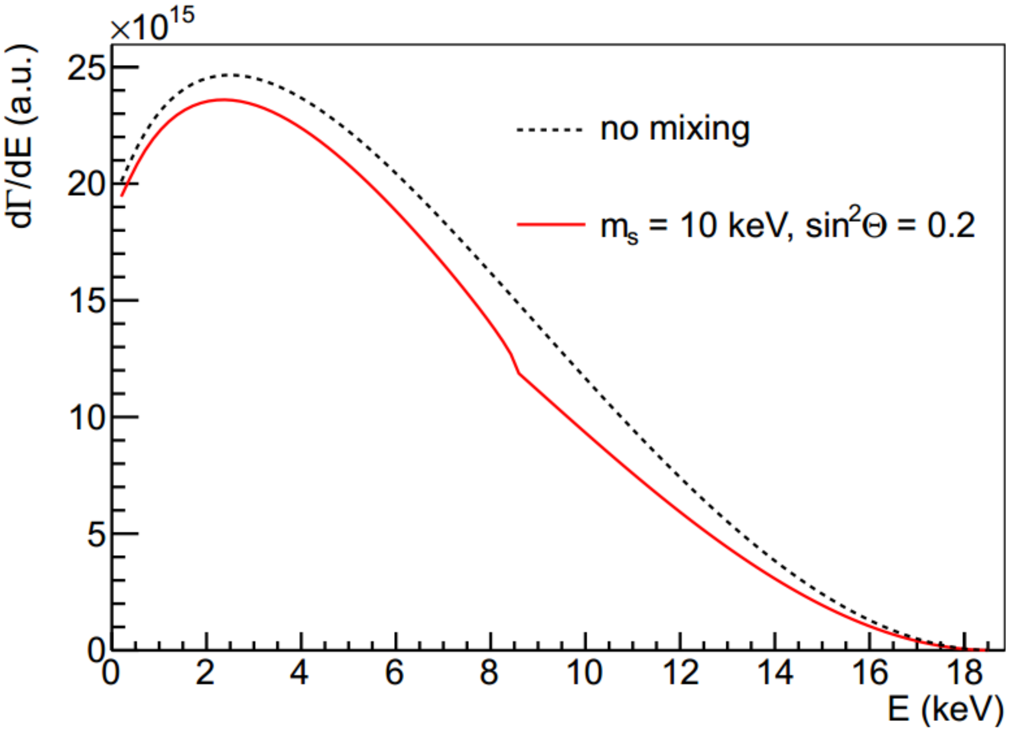

Figure 4.1: Tritium β-decay spectrum without sterile neutrino contribution (dashed) and with exemplary case of exaggerated mixing with $\sin^2\theta = 0.2$ and $m_h = 10\,\mathrm{keV}$ (red solid). Figure reproduced from [Mer+15a].

and the isotropic angular distribution $g(\vartheta)$ by convolution with the energy loss distribution from inelastic scattering f_{loss} as in eq. (3.13). In order to account for sterile neutrinos, the β-spectrum in (3.13) has to be replaced by the corresponding β-spectrum with a sterile neutrino (4.3). Since the TOF spectrum (3.8) is isomorphic to the β-spectrum, the TOF spectrum with sterile neutrinos can thereforealso be expressed as a superposition of two TOF spectra with neutrino masses m_l and m_h, respectively:

$$\frac{\mathrm{d}N}{\mathrm{d}\tau}(m_{\nu_e}) = \sin^2\theta\frac{\mathrm{d}N}{\mathrm{d}\tau}(m_h) + \cos^2\theta\frac{\mathrm{d}N}{\mathrm{d}\tau}(m_l)\,. \tag{4.4}$$

Fig. 4.2 shows the TOF (3.5) as a function of E for different angles and high surplus energy to illustrate the benefits of a TOF measurement for keV scale sterile neutrinos. It can be seen that energy differences up to some $\sim 100\,\mathrm{eV}$ above the retarding potential translate into significant TOF differences. Within these regions, TOF spectroscopy is thus a sensitive *differential* measurement of the energy spectrum. Combining multiple TOF spectra measured at different retarding energies thus allows to measure a differential equivalent of the β-spectrum throughout the whole region of interest. As already outlined in [Mer+15a], a differential measurement has important benefits for a sterile neutrino search. On one hand it enhances the statistical sensitivity, since the sterile neutrino signature can be measured directly without any intrinsic background from higher energies as in the classic integrating mode (section 2.3), which is basically a high-pass filter. On the other hand, it reduces the systematic uncertainty, since it improves the distinction between systematic effects and a real sterile neutrino signature in the spectrum.

The prospects for a TOF measurement method has already been discussed in section 3.3.

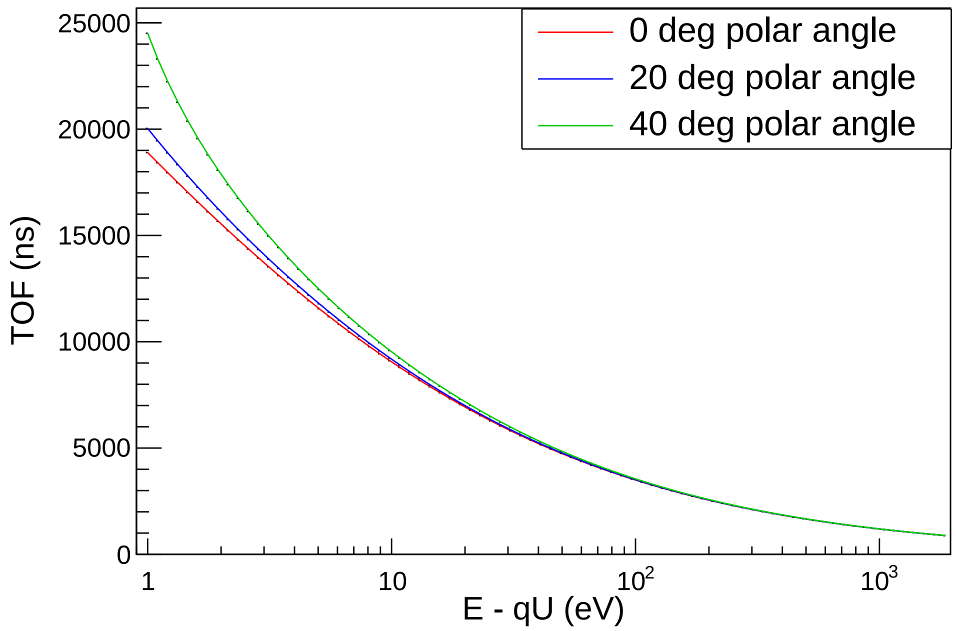

Figure 4.2: TOF as a function of surplus energy $E - qU$. Significant energy differences are detectable up to a few 100 eV above the filter threshold. By combining multiple TOF spectra with different retarding energies, the TOF method will give a differential map of the energy spectrum within the measuring interval.

Regarding electron tagging (section 3.3.2), the difficulties of a technical realization, which lie in extracting a minimal amount of energy from passing electrons, which is still above thermal noise, have already been mentioned. In addition, it seems unlikely that such an approach is also useful for keV sterile neutrino searches, since the high count-rates would lead to massive pile-up. A possible way out could be a form of high-frequency tagging, where the time correlation between start and stop signals could approximate the TOF spectrum. However, this would still require a somewhat moderate rate and without a breakthrough in electron tagging it is not worthwhile to perform a detailed simulation of that idea.

The gated filter (GF) method (section 3.3.3) seems more fruitful for a keV scale sterile neutrino search. In theory, the high signal rate at retarding potentials of several keV below the endpoint can be used in conjunction with a small duty cycle to achieve a sharp time resolution. The main downside of the method is that it sacrifices statistics in order to get time information. However, it would require minimal hardware modifications, since only the capability to pulse the pre-spectrometer potential by some keV would have to be added. Since the focal plane detector of KATRIN is optimized for low rates near the endpoint, the count-rate reduction by small duty cycles could be a welcome by-product. However, in this scenario with small hardware modifications, it is unlikely that the pre-spectrometer potential can be pulsed by more than some keV. Due to the capacity of the pre-spectrometer, there is possibly a non-vanishing ramping time involved, depending on the ramping interval. If electrons arrive within the ramping time, they become either accelerated or retarded, giving rise to non-isochronous background. The problem can be mitigated partly by using a voltage supply with higher power. Alternatively, a mechanical high frequency beam shutter could be used, however, this would require larger modifications of the set-up. This problem shall not be discussed further and just an ideally efficient method of periodically blocking the beam assumed. However, the sensitivity study of the sterile neutrino search with the GF method shall be restricted to a measurement region spanning only a few keV below the endpoint.

4.2 Monte Carlo Sensitivity Estimation

The TOF spectrum (3.8) can not be calculated analytically, since the magnetic field $B(z)$ and electron potential $q\Delta U(z)$ is only known numerically. Furthermore, there is no easy way to evaluate the δ function in the TOF spectrum (3.8). It is possible to calculate it deterministically via numerical integration, as done for the case of the active neutrino mass measurement in chapter 3. However, due to the convolution with the energy loss function in (3.13), this method performs slowly for a large spectral surplus $E_0 - qU$ and lacks flexibility in the treatment of systematics. It is, however, feasible to sample (3.8) via Monte Carlo on a per-event basis. This especially avoids the calculation of the inverse of (3.5) and the convolution with the energy loss function (3.13).

However, it faces the problem that an extreme number of events is needed to create a model that is sufficiently precise to account for both the high count rates and the tiny sterile contribution of $\mathcal{O}(10^{-7})$ or below. KATRIN is designed for measurements with low rates in the order of several cps, which is the case near the endpoint. The measurements for the keV scale sterile neutrino detection have to be performed over a significantly broader region of the β-spectrum if not the whole spectrum itself and thus count rates up to $\sim 10^{10}$ Hz can occur. That poses not only a challenge for any future measurement but for the sensitivity analysis. In the following section, the classic approach to sensitivity analysis, the problems that arise in this special case and an approach to break down the problem into an adequate substitute for a pure sensitivity study will be discussed.

4.2.1 Classic Approach

While there is no coherent definition of the concept of sensitivity [Pun03], we will identify it in the following with the average confidence interval of a parameter of interest μ_i in presence of a null hypothesis H_0 [FC97]. That way, a common frequentist way of sensitivity estimation is performed by generating simulated toy measurement data, fitting them with a probabilistic model and determining the confidence region of μ_i by repeating this procedure multiple times. The model can be expressed as a probability density function over potential data-points x

$$\Phi(x \mid \vec{\mu}) \tag{4.5}$$

with parameters $\vec{\mu} \in \mathbb{R}^d$. It can be analytical (like for instance the tritium β-spectrum) or numerically approximated, e.g. by Monte Carlo (MC) algorithms.

For brevity let us assume in the following that the data are binned. Toy data can be generated randomly from the model. Assuming the probability is constant over time, the number of events n_i in the i-th bin at position $x = x_i$ are then Poisson distributed with the expectation value λ_i given by the model,

$$P(n_i) = \frac{\lambda_i^{n_i}}{n_i!} e^{-\lambda_i}, \qquad \lambda_i = n \cdot \Phi(x_i \mid \vec{\mu}), \tag{4.6}$$

for sufficiently small bin widths, where n is the expected total number of events.

Since the probability to obtain a certain data set depends on the parameters $\vec{\mu}$, a certain choice of their fiducial values has to be met before the data generation. That depends on the scenario which is to be studied. Given the above definition of sensitivity, the most straightforward way is to set the parameters of interests, for which the sensitivity is to be determined, to their respective values given by the null hypothesis H_0.[1] Other parameters can e.g. be set close to the most likely value or a range of values, depending on the experimental scenario. By standard procedure, for the chosen parameter values toy data are generated multiple times (usually > 1000) and fitted by a χ^2 or $-\log L$ minimization. The histogram of best fit values of any parameter of interest μ_i allows then to determine quite robust confidence regions.

Often the main challenge is the construction of a parametrizable model. In many cases that is only feasible by Monte Carlo (MC) methods. The model (4.5) then has an uncertainty $\Delta\Phi$ which depends on the particular simulation method and the MC sample size N with $\Delta\Phi \to 0$ for $N \to \infty$. For a basic sensitivity analysis based on a fit of toy data, the theoretical uncertainty of the prediction has to be much smaller than the measurement uncertainty of the data,

$$\Delta\lambda_i(\vec{\mu}) \ll \Delta n_i \,, \tag{4.7}$$

with $\Delta\lambda_i(\mu) = n \cdot \Delta\Phi(x_i \mid \vec{\mu})$, for all x_i and $\vec{\mu}$. This translates in the case of Poissonian statistics (4.6) into

$$\Delta\lambda_i(\vec{\mu}) \ll \sqrt{n_i} \,. \tag{4.8}$$

Otherwise, the fit statistics function (χ^2 or $\log L$) will become fluctuating and give rise to false extrema and parameter uncertainties. In most physical scenarios, the model for a certain parameter state $\vec{\mu}$ is simulated on a per-event basis with MC sample size N and then scaled, which gives a Poissonian error as well with $\Delta\lambda_i/\lambda_i = 1/\sqrt{N_i}$, where N_i is the MC sub-sample size for bin i. If we further assume that there are no drastic differences between prediction λ_i and data n_i within the allowed parameter region of $\vec{\mu}$, the bins can be summed up and the condition translates, using $\sum_i n_i \approx n$, into

$$N(\vec{\mu}) \gg n \,, \tag{4.9}$$

where $N(\vec{\mu})$ is the MC sample size used to estimate the model at parameter state $(\vec{\mu})$ and n the total number of expected data. A continuous model for the whole parameter space $\vec{\mu}$ is usually obtained by simulating the model for certain discrete grid points in the $\vec{\mu}$ space and interpolating between them. In the following discussion, the error induced by the interpolation, while certainly present, will be neglected. However, it should be noted that, since a set of models with one for each grid point has to be simulated, the total number of required simulation events grows by the number of grid points for each interpolation dimension.

Condition (4.9) effectively limits the order of magnitude of expected data for which a sensitivity analysis can be performed the traditional Monte Carlo way, given limited computer hardware. E.g., in the case of the sterile neutrino search with KATRIN using TOF spectroscopy, as discussed in section 4.1.2, one has for a data taking time $t = 3\,\mathrm{y}$ with a

[1] Correctly, one would have to perform a Feldman Cousins analysis [FC97] or Neyman construction [Ney37] using a range of values for the parameter of interest μ_i. However, if the the statistical band between true value and best fit is sufficiently linear, diagonal and unbiased, the average confidence interval can be approximated by the respective percentiles in the fit value histogram.

maximal count rate of $\Gamma \sim 10^{10}$ a total number of counts up to

$$n = \Gamma \cdot t \sim 10^{18} . \tag{4.10}$$

Hence, one would need at least $\sim 10^{20}$ MC events per TOF spectrum if the theoretical uncertainty of the prediction shall be less than 10 % of the Poissonian uncertainty of the data. This means in general that, for high-statistics scenarios like this, a different simulation strategy has to be applied in order to reduce model variance. One could in principle avoid this issue for most Poissonian scenarios by estimating the sensitivity for lower statistics and scaling it with $1/\sqrt{n}$. However, that requires a strictly Gaussian uncertainty of the parameter of interest and doesn't hold necessarily true for systematic errors.

4.2.2 The Self-Consistent Importance Sampling (SCIS) Technique for Sensitivity Estimation

To solve the issue, it is helpful to borrow a basic idea from importance sampling [RK08]. In importance sampling, in order to estimate a certain statistics, instead of the distribution of interest Φ, a different distribution Φ' is sampled with higher density in regions which have a stronger impact on the statistics. The approach proposed in the following section, called *self-consistent importance sampling* (SCIS) in the following, deviates from classic importance sampling in so far that no fundamentally different distribution will be sampled from, but rather that the distribution will be replaced in part by approximations. However, that will effectively cause the sampled distribution to deviate from the real distribution while still maintaining a correct sensitivity estimate.

Using SCIS, the initial problem can be addressed by expressing the distribution of interest by a linear combination

$$\Phi = c_S \Phi_S + c_B \Phi_B, \tag{4.11}$$

consisting of a *signal* contribution $c_S \Phi_S$, sampled with maximum precision, and an approximated *background* contribution, $c_B \Phi_B$. The distribution of interest is then replaced by a modified distribution

$$\Phi' = c_S \Phi_S + c_B \Phi'_B, \tag{4.12}$$

with $\Phi'_B \sim \Phi_B$, where the background component is either be approximated by an analytic expression or simulated by the same method as Φ_S with a reduced sample size. An example for illustration purposes can be found in fig. 4.3 The definition of the coefficients c_S and c_B is arbitrary, but for the physical problem under investigation (experimental signature of a sterile neutrino in Tritium β-decay) it is natural to take $c_S + c_B = 1$ and $\int \mathrm{d}x\ \Phi_S \approx \int \mathrm{d}x\ \Phi_B$. In this case, the coefficients can roughly be interpreted as relative fraction of signal and background events, respectively.

The distinction of signal and background is dependent on the parameters of interest, i.e. those upon which the sensitivity is to be estimated. There is no generic recipe to separate Φ_S and Φ_B, but a principle condition is that Φ_B is independent of all parameters of interest,

$$\frac{\mathrm{d}\Phi_B}{\mathrm{d}\mu} = 0, \tag{4.13}$$

for all parameters of interest μ and those which are strongly correlated. The approximate model (4.12) can then be used as replacement for the real model in the basic sensitivity analysis scheme described in section 4.2.1. That works in the following way. Firstly, if toy data are generated from (4.12), they are basically inaccurate. However, the whole scheme is self-consistent. The total approximated distribution Φ' is inaccurate but contains all essential information about the sensitivity, since $\Phi' - c_B\Phi'_B = c_S\Phi_S$ holds exactly. If condition (4.13) is met, the width of the χ^2 minimum stays the same as long as the background components are at least approximately correct. The purpose of the latter condition is to preserve the Poissonian uncertainty which enters the log likelihood. A simplified proof can be found in appendix A.

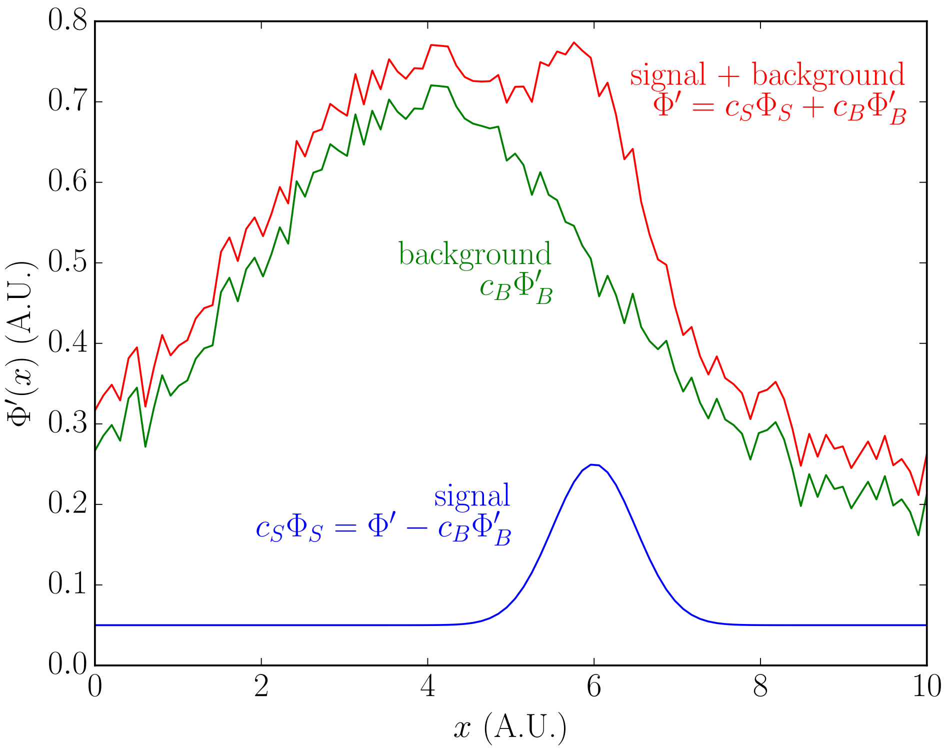

Figure 4.3: Illustration of the SCIS principle. The signal term $c_S\Phi_S$ has been simulated precisely acc. to (4.17), while the background term $c_B\Phi'_B$ has been approximated by a low statistics MC simulation. The total approximated distribution Φ' is then inaccurate but contains all essential information about the sensitivity, because $\Phi' - c_B\Phi'_B = c_S\Phi_S$ holds exactly.

This method is especially effective if the signal is small compared to the background, which is met by the convention above if $c_S \ll c_B$. In this case the necessary sample size is reduced by a factor c_S^2. This kind of variance reduction is the consequence of two aspects. These shall be discussed for the example of a keV sterile neutrino search with KATRIN using TOF spectroscopy, again. It was already shown that the TOF spectrum with sterile neutrinos can also be expressed as a superposition of a sterile and an active component (3.8). The modified distribution (4.12) can, therefore, be established with the sterile-only contribution with $c_S = \sin^2\theta$ as signal and the active-only contribution $c_B = \cos^2\theta$ as background.

The first contribution to the variance reduction is rather self-evident. Since in SCIS the background can be approximated, only the signal part needs to be simulated with high-statistics Monte Carlo. E.g., with a mixing of $\sin^2\theta = 10^{-8}$ one would, according to (4.7), only need a MC sample size of $N \gg n \cdot \sin^2\theta$ with up to

$$n \cdot \sin^2\theta \;\sim\; 10^{18} \cdot 10^{-8} = 10^{10} \tag{4.14}$$

in order to simulate the signal part correctly.

There is, however, a second contribution which is not obvious *prima facie*. It is given by the fact that in an actual experiment the signal is never measured in an isolated manner but always in combination with background. Taken the earlier condition of maximum allowed theoretical uncertainty (4.7), it states therefore that

$$\Delta\lambda_{S_i} \ll \Delta n_i \;, \tag{4.15}$$

where $\Delta\lambda_{S_i}$ is the theoretical uncertainty of the prediction in bin i only for the signal with $\lambda_{S_i} = n \cdot c_S \cdot \Phi_S(x = X_i)$, while n_i still denotes all events in bin i. Using $\Delta\lambda_{S_i}/\lambda_{S_i} = 1/\sqrt{N_i}$ with signal-only MC sub-sample size N_i in bin i, eq. (4.15) gives

$$\frac{1}{\sqrt{N_i}} \ll \frac{\sqrt{n_i}}{\lambda_{S_i}} \iff N_i \gg \frac{\lambda_{S_i}^2}{n_i} \;. \tag{4.16}$$

Summing up the bins as done for (4.9) and using $\sum_i \lambda_{S_i} \approx n_s = n \cdot c_S$, that gives

$$N_S \gg n \cdot c_S^2 \;. \tag{4.17}$$

In the context of the KATRIN example, we have

$$n \cdot c_S^2 = \Gamma \cdot t \cdot \sin^4\theta \;\sim\; 10^{18} \cdot 10^{-16} = 10^2 \;. \tag{4.18}$$

E.g., taking a realistic value for the sample size, such as 10^6 per TOF spectrum, the uncertainty of prediction according to (4.15) would be only 1 % of the measurement uncertainty of the data. This holds as long as self-consistency of toy data and model are guaranteed. The method does, however, not work for real data or toy data simulated by an independent algorithm.

4.3 Implementation

4.3.1 Probabilistic Model: TOF Spectra

As derived above, the electron TOF spectrum (3.8) with added sterile neutrinos can be expressed as a superposition of two TOF spectra with neutrino masses m_l and m_h, respectively. Using the SCIS method (4.11), we identify, as indicated before, the signal with the sterile neutrino component of the TOF spectrum (4.4) and the background with the active neutrino contribution,

$$\Phi_S = \frac{\mathrm{d}N}{\mathrm{d}\tau}(m_h) \qquad \Phi_B = \frac{\mathrm{d}N}{\mathrm{d}\tau}(m_l) \;. \tag{4.19}$$

The coefficients are then given by the active-sterile mixing,

$$c_S = \sin^2\Theta \qquad c_B = \cos^2\Theta \;. \tag{4.20}$$

Using a Monte Carlo algorithm, the TOF spectra given by the transformation (3.8) can be determined in a straightforward way. For each MC sample, initial energy and starting angle is generated. The isotropic angular distribution is given by (3.11). For the initial energy, the electronic excited state is generated from the final state distribution in (4.1) and then the energy is generated from the respective β-spectrum component (4.2). Given the initial energy and the starting angle, the number of inelastic scattering processes in the source is generated from (3.15) and for each process a randomized energy loss is generated from (3.14) and subtracted from the energy.

In order to optimize the SCIS method for a parametrizable heavy neutrino mass, the strategy has been slightly refined. The idea is to split the signal Φ_S into sub-signals Φ_{S_k} which can be added subsequently to obtain the signal for a given sterile neutrino mass m_h. That works as follows: at first a number J of grid points with heavy neutrino masses m_j are chosen. For each grid-point j, the signal spectrum is given as the sum of all sub-signals from j up to J,

$$\Phi_S(m_j) = \sum_{k=j}^{J} \Phi_{S_k} \ . \tag{4.21}$$

The sub-signals Φ_{S_k} constitute the difference of two TOF spectra with adjacent sterile neutrino masses. The total TOF spectrum for the sterile component can then be written as

$$\frac{\mathrm{d}N}{\mathrm{d}\tau}(m_j) = \frac{\mathrm{d}N}{\mathrm{d}\tau}(m_J) + \sum_{k=j}^{J-1} \left(\frac{\mathrm{d}N}{\mathrm{d}\tau}(m_k) - \frac{\mathrm{d}N}{\mathrm{d}\tau}(m_{k+1}) \right) . \tag{4.22}$$

Each sub-component in the sum will be sampled separately. The difference between two TOF spectra can be sampled just like any TOF spectrum, as outlined, by replacing the β-spectrum in (3.8) also with the difference of two β spectra corresponding to the neutrino masses m_k and m_{k+1}. Via (4.22), that gives then the sterile contribution of the TOF spectrum for each mass value m_j on the grid. For sterile neutrino masses between the grid points, the resulting spectrum is then calculated by cubic spline interpolation. The strategy is illustrated in fig. 4.4. The advantage of such a scheme is that by the reuse of sub-components of the spectrum the overall computing time can be saved and thus higher sample sizes for each spectrum can be accomplished. Furthermore, the interpolation will be smoother since also in bins with small statistics, which are possible for high flight times $\gtrsim 40\,\mu\mathrm{s}$, monotony is guaranteed. However, if a sufficient overall sample size is chosen, the latter effect should not matter significantly.

It has been found that a sample size of 10^8 for each sterile sub-component is feasible in finite calculation time and sufficient for an accurate simulation. The active neutrino component, which contains $\sim 1/\sin^2\theta$ more counts than the total sterile component, was approximated with a sample size of 10^9, according to the SCIS technique. The active neutrino mass was set to $m_l = 0$ and the endpoint held constant at $E_0 = 18.575\,\mathrm{keV}$, since there is no correlation to expect with the sterile neutrino. The bin width was chosen to be 250 ns (compared to the FPD time resolution of about 50 ns) for reasons of performance and robustness. However, it is unlikely to expect for any measurement method to achieve a higher resolution. To all spectra a Gaussian time uncertainty of $\Delta\tau = 50\,\mathrm{ns}$ was added to account for the detector time resolution and a isochronous background of $b = 10\,\mathrm{mcps}$.

Figures 4.5 and 4.6 show exemplary simulated TOF spectra for different active-sterile mixings and heavy neutrino masses, respectively. It can be seen that the spectra show a dominating peak within the first 2 µs, which consists of the fast electrons more than some

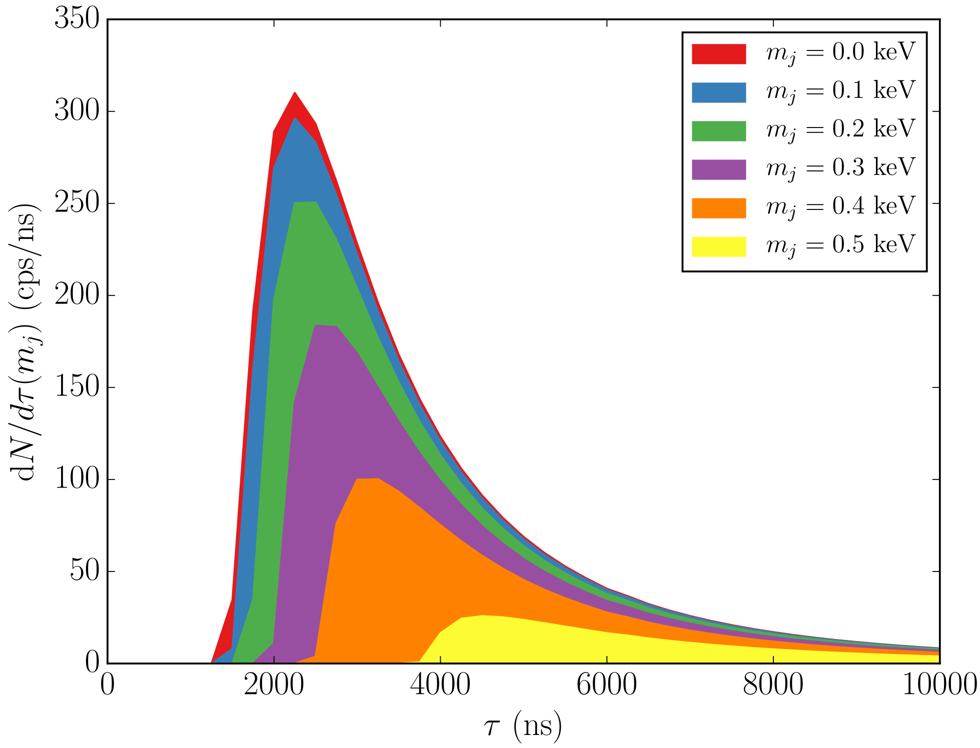

Figure 4.4: Illustration of the calculation of sterile component of the electron TOF spectrum via subsequent addition of sub-components according to (4.22). The figure shows the sterile components of the TOF spectrum (4.4) for different sterile neutrino masses m_j on a grid for a retarding potential of $qU = 18\,\mathrm{kV}$. Each colored area corresponds to a sub-component between two adjacent mass values. The component for any sterile neutrino mass m_j is then given by the sum of all areas below the envelope.

100 eV above the retarding potential. They are, however, followed by a long tail where the electron velocity becomes slower and the TOF difference per given energy difference (see fig 4.2) becomes more significant. In this region the TOF spectrum is to a good extent a differential map of the β-spectrum, while the fast peak region consists only of some bins, thus contributing to the sensitivity more by its integral. If the sterile neutrino mass is some 100 eV smaller than the difference between retarding potential and endpoint, the sterile neutrino signal becomes similar to that one in the tritium β-spectrum. The sterile neutrino contribution appears as a discontinuity in shape of a "kink" at a certain position in the spectrum. Since the relationship between energy and TOF is non-linear, the position of the kink allows no *prima facie* conclusion about the sterile neutrino mass. However, given the retarding potential, the relation in fig. 4.2 can be used for an estimation.

4.3.2 Ideal TOF Mode Sensitivity

The model described in the last chapter was utilized to estimate the sensitivity according to the procedure described in chapter 4.2. The fits have generally been performed by a χ^2 minimizations using MINUIT [JR75] . For statistical sensitivity estimation, the mixing $\sin^2\theta$ and overall amplitude S are free fit parameters, using a range of fixed values for m_h. In those simulations where the uncertainty on m_h is of interest, the squared heavy neutrino mass m_h^2 has also been included as fit parameter. Since each fit incorporates a set of multiple

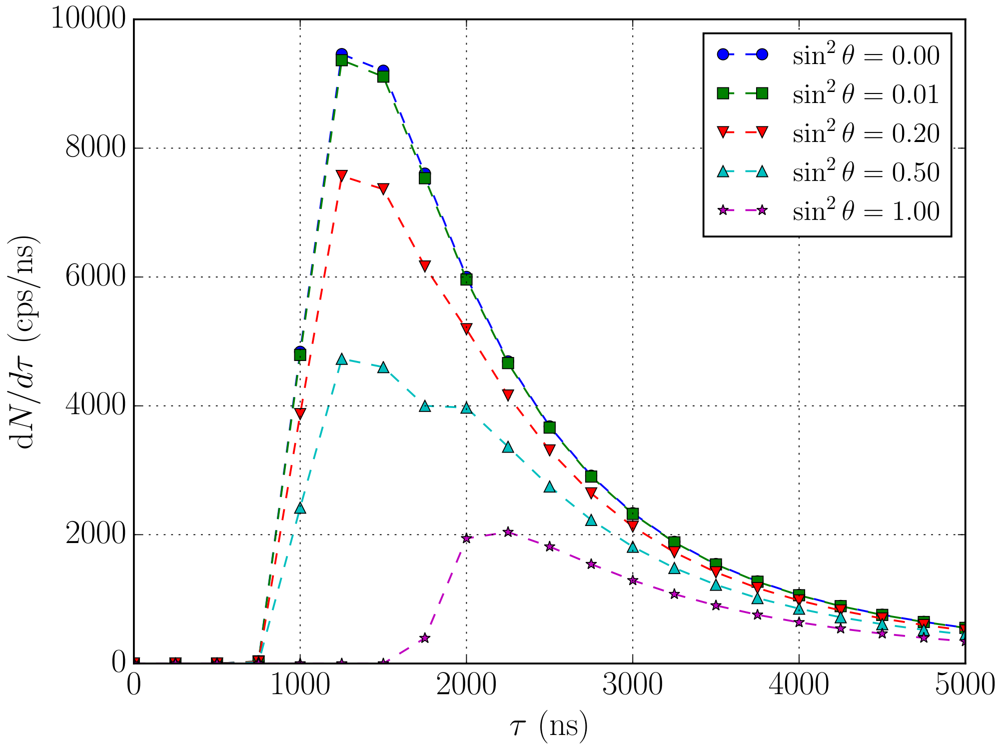

Figure 4.5: Electron TOF spectra for a keV-scale sterile neutrino of $m_h = 1.1$ keV and different mixing angles at a fixed retarding potential of 17 keV. The mixing angles have been exaggerated to enhance the signature and comprise additionally the case of no mixing ($\sin^2\theta = 0$), as well as of pure sterile contribution ($\sin^2\theta = 1$). Similar to the tritium β-decay energy spectrum, the signature of a sterile neutrino is a kink-like discontinuity at a certain point in the TOF spectrum. Figure first published in [Dre+17].

measurements at different retarding potentials, the χ^2 functions of each measurement are added and fitted with global fit parameters. Instead of a pure ensemble approach, the parameter uncertainties have been calculated using MINOS [JR75], averaged over multiple simulations, which gives in case of an approximately quadratic χ^2 near the minimum an identical result.

Exemplary Systematics

In addition to the statistical sensitivity, an exemplary systematic effect has been studied, which is the inelastic scattering cross section due to fluctuation in the column density as described in (3.14). This is one of two main systematics when it comes to keV sterile neutrino search, the other being the final state distribution [SJF00; Dos+06; DT08]. To incorporate the systematics, the χ^2 function has been modified by an additional term:

$$\chi^2 = \chi_0^2 + \frac{(\rho d - \langle \rho d \rangle)^2}{(\Delta \rho d)^2} \,, \tag{4.23}$$

where χ_0^2 is the default binned χ^2 function, ρd the fitted column density, $\langle \rho d \rangle$ its expectation value and $\Delta \rho d$ the systematic uncertainty. In order to be able to have ρd as free fit parameter, the complete model has additionally been separated by number of inelastic

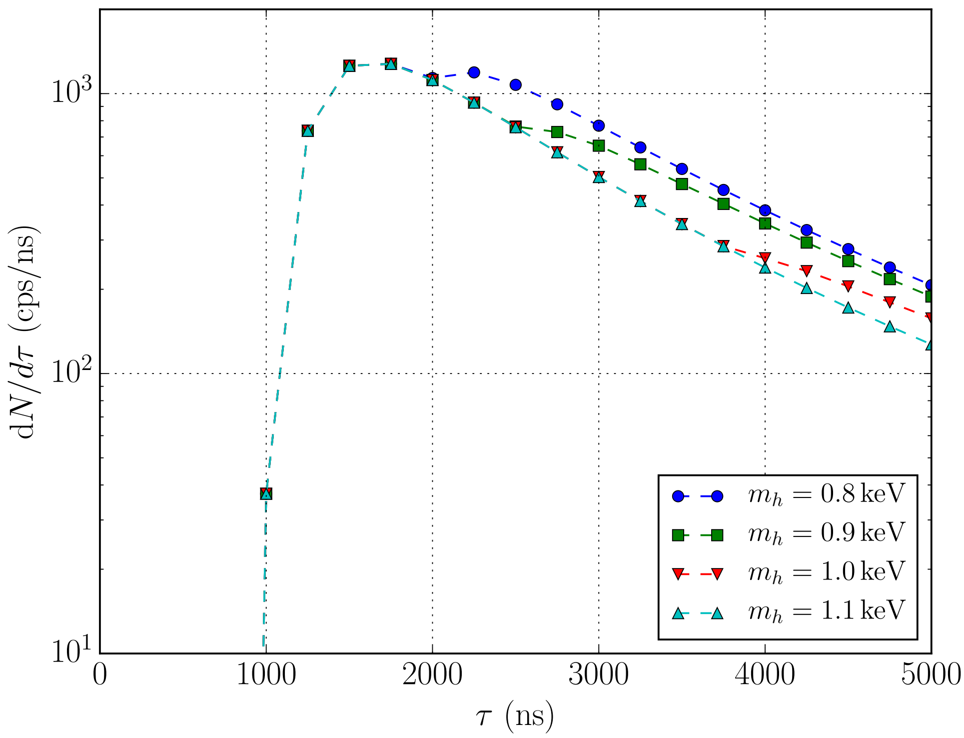

Figure 4.6: Electron TOF spectra for different sterile neutrino masses at a fixed retarding potential of 17 keV. The mixing has been set to $\sin^2\theta = 0.5$ to enhance the signature. The heavy neutrino mass determines the position of the kink on the TOF-axis. The on-set TOF for a certain sterile neutrino mass can be estimated from fig. 4.2.

scattering processes and weighted with the l-fold energy loss probability $p_l(\rho d)$, as given by (3.15), instead of randomly generating the number of inelastic scattering events:

$$\frac{\mathrm{d}N}{\mathrm{d}\tau} = \sum_l p_l(\rho d) \left(\frac{\mathrm{d}N}{\mathrm{d}\tau}\right)_l . \tag{4.24}$$

For the data generation, the column density has been shifted by its uncertainty $\rho d = \langle\rho d\rangle + \Delta\rho d$ while still using the unshifted expectation value $\langle\rho d\rangle$ in (4.23). By this approach, the MINOS error will increase plus a possibly slight bias in average which is then quadratically added to the average error bars.

To illustrate the imprint of the systematic uncertainty of ρd in the TOF spectrum, fig. 4.7 shows the difference between a TOF spectrum with shifted column density, $\Phi(\rho d) = \mathrm{d}N/\mathrm{d}\tau(\rho d)$ and a TOF spectrum with mean column density, $\Phi_0 = \mathrm{d}N/\mathrm{d}\tau(\langle\rho d\rangle)$, weighted by $\sqrt{\Phi_0}$, which is proportional to the expected Poissonian uncertainty of the data. By doing so, the signature becomes visible proportionally to its impact in the χ^2 function. It can be seen that the imprint of a shifted column density is present foremost at lower flight times, which is since the energy loss causes the count-rate near the endpoint to drop. There are fluctuations at higher flight times near the retarding potential arising from the energy loss spectrum (3.14). However, these are weighted minimally, since the differential rate in the TOF spectrum drops with higher flight times (cf. fig. 4.5).

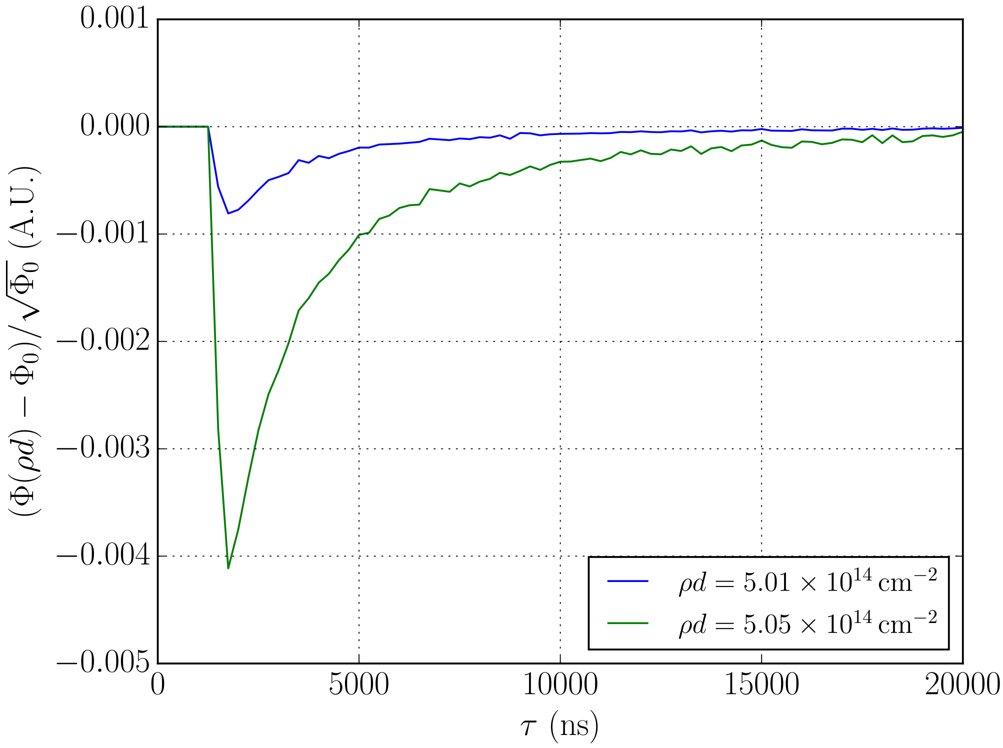

Figure 4.7: Difference between TOF spectra with shifted ρd, $\Phi(\rho d)$ and default value $\langle \rho d \rangle = 5 \times 10^{17}\,\mathrm{cm}^{-2}$, Φ_0, weighted proportionally with the expected Poissonian uncertainty of the data $\propto \sqrt{\Phi_0}$. The imprint of a shifted column density is present foremost at lower flight times, due to missing events near the endpoint because of the energy loss. Fluctuations at higher flight times near the retarding potential are suppressed by a lower differential count rate. The spectra consist only of the active neutrino component, $\sin^2\theta = 0$, and the retarding potential is $qU = 18\,\mathrm{kV}$.

Results

Figure 4.8 shows the sensitivity for an ideal TOF mode. The results are based on three years measurement time, which was distributed uniformly on the retarding potential within an interval of [4; 18.5] keV with steps of 0.5 keV. The setting was chosen in that way that a 7 keV neutrino signal [Bul+14] would roughly lie in the center of the potential distribution. For the exemplary inelastic scattering systematics, an initial uncertainty of $\Delta\rho d/\rho d = 0.002$ has been assumed in accordance with [KAT04]. The statistical sensitivity of the integral mode in this simulation is in good agreement with [Mer+15a]. The statistical sensitivity of the ideal TOF mode is close to that of an ideal differential detector in the aforementioned publication. However, if the uncertainties of the column density are incorporated, the benefit by the TOF mode grows even further, since a shifted column density has a unique imprint in the TOF spectrum (see fig. 4.7), which is not the case in the integral mode. It should be noted, however, that for low retarding potentials, as utilized in fig. 4.8, adiabacity of the electron transport is limited. Yet, that can be maintained by increasing the magnetic field in the main spectrometer. This lowers the energy resolution and thus the transformation of transverse into longitudinal momentum, which would manifest in a stronger angular-dependence of the energy-TOF relation in fig. 4.2. Though, this should have no significant influence on the sensitivity, since the measurement takes place on a keV scale, where the requirements for magnetic adiabatic collimation are more relaxed.

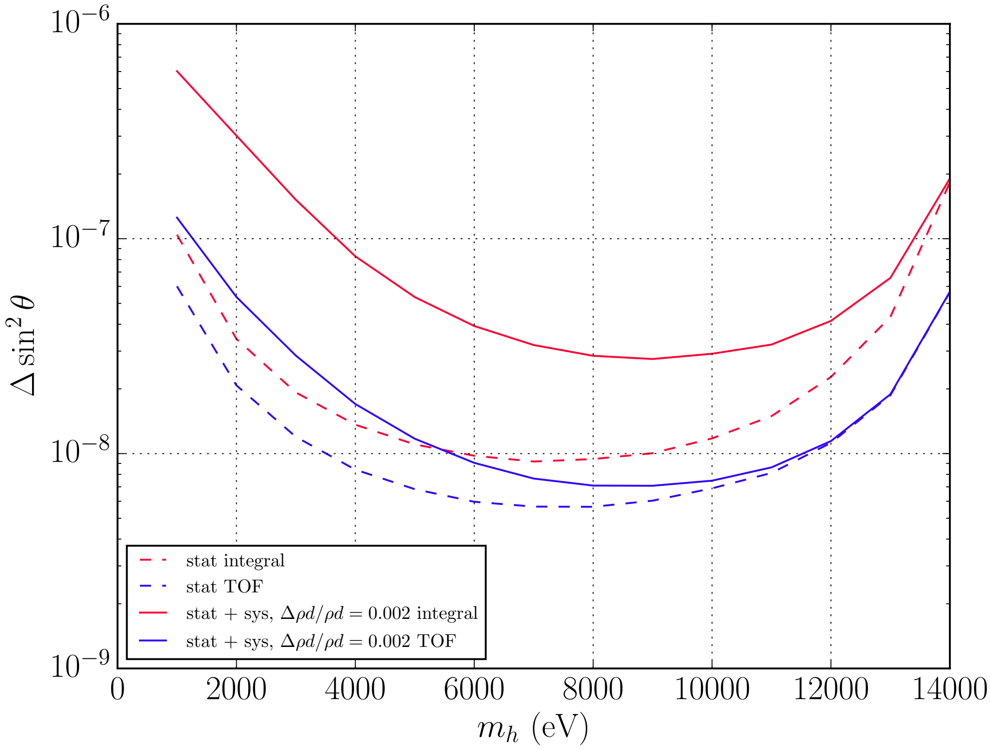

Figure 4.8: Sensitivity (1 σ) of ideal TOF mode (blue) compared with integral mode (red). Both statistical uncertainty (dashed lines) and combined uncertainty with exemplary systematics (full lines) in form of column density uncertainty $\Delta\rho d/\rho d = 0.002$ affecting the inelastic scattering cross section in the WGTS. It can clearly be seen that the sensitivity gain by a TOF mode is especially significant if the uncertainty of the column density is accounted for. The results are based on three years measurement time, distributed uniformly on the retarding potential within an interval of [4; 18.5] keV.

An exemplary fit is shown in fig. 4.9 for sterile neutrino with mass $m_h = 2\,\text{keV}$ and non-realistic mixing $\sin^2\theta = 10^{-6}$, assuming an ideal TOF measurement and using four exemplary retarding potentials of 15, 16, 17 and 18 keV. While it is in principle sufficient to use only one retarding potential closely below the sterile neutrino kink, a larger number of retarding potentials is necessary in practice. This is due to the fact that the mass of the sterile neutrino is unknown and that, at lower retarding potentials, the count rate is significantly increased. In contrast to the pure sterile active mixing sensitivity estimation (fig. 4.8), the heavy neutrino mass has been used as free fit parameter. It shows that the method is capable of a sensitive mass determination as well, in case the mixing angle is large enough. However, since most regions of the sensitive regions of the TOF method are already excluded by X ray satellite measurements [Wat+06], it seems unlikely that a mass fit will be possible.

4.3.3 Optimization and Integrity

SCIS Variance

In order to show that the SCIS method is really working as expected, it has been tested using different Monte Carlo sample sizes. A necessary condition is convergence of the result towards a constant value with growing sample size. Fig. 4.10 shows the ideal TOF mode

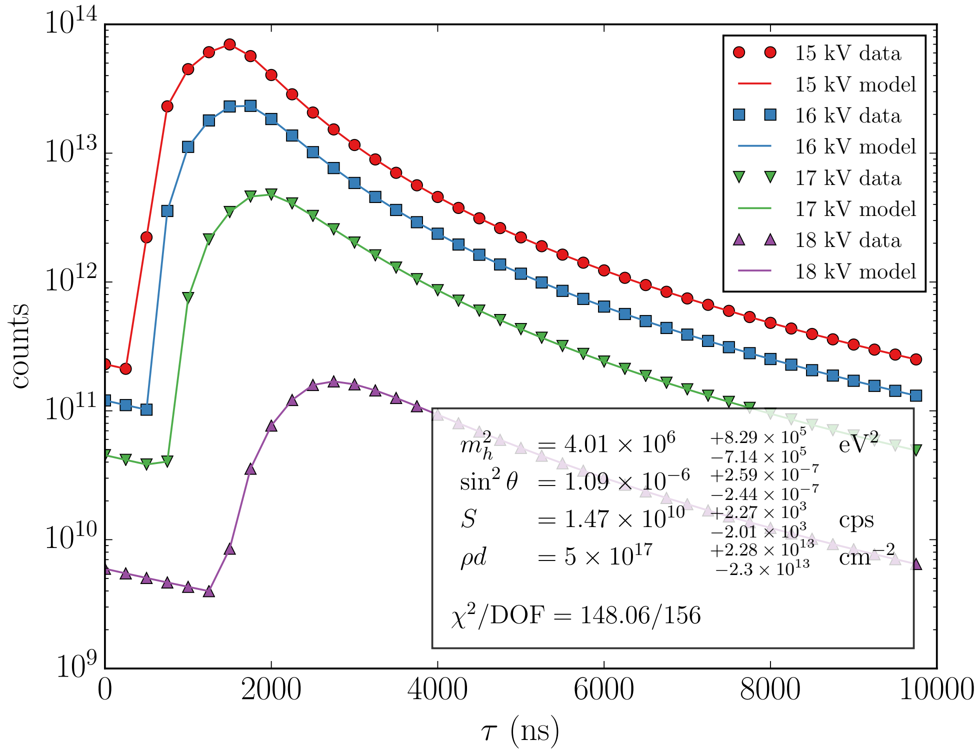

Figure 4.9: Exemplary fit of a sterile neutrino with mass $m_h = 2$ keV and non-realistic mixing $\sin^2\theta = 10^{-6}$ assuming an ideal TOF measurement and using four exemplary retarding potentials of 15, 16, 17 and 18 keV. The fit includes systematic uncertainty of the column density $\delta\rho d/\rho d = 2 \times 10^{-3}$, as well as the sterile neutrino mass as free fit parameters. The overall count rate increases with decreasing retarding potential.

statistical sensitivity for a 2 keV neutrino as a function of the sample size used for each signal component in eq. (4.22). It can be seen that convergence is met and that already low sample sizes such as 10^4 approximate the expected result with less than 1 percent uncertainty.

Measurement Interval

Fig. 4.11 shows the same for a measurement interval of [15; 18.5] keV, roughly centered around a 2 keV neutrino, as favoured in [DVS13]. It can be seen in comparison that there is no benefit of restricting the measurement interval to a narrow region in search for a sterile neutrino with a given energy. This seems counter-intuitive at first, but is has to be kept in mind that the sterile neutrino signal is not localized at the kink, but instead contributes to the whole spectrum below. In contrast to dedicated "kink-search" methods [Mer+15b], all spectral parts contribute to the sensitivity in a χ^2 fit. While the relative difference made by a sterile neutrino signal might be smaller at lower retarding potentials, this drawback is balanced by a larger count-rate at lower potentials. However, as there are further systematics which have not been considered, such as, e.g., the final state distribution at higher excitation energies, it is possible that the restriction of the measurement interval might have a certain effect in the end.

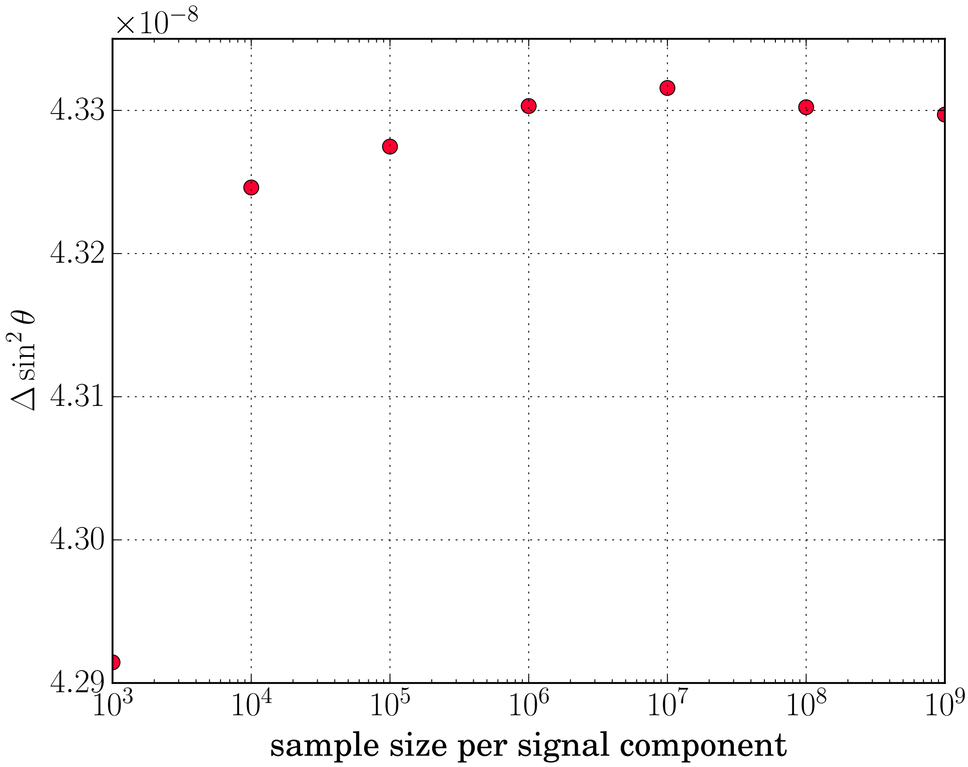

Figure 4.10: Estimated statistical sensitivity with ideal TOF mode for a 2 keV neutrino with $sin^2\theta = 0$ as a function of the MC sample size per signal component (4.22) using a measurement interval of [4; 18.5] keV. The background has been simulated using one 10th of the respective signal sample size.

Measurement step size

Fig. 4.12 shows the statistical sensitivity as a function of the spacing between different measurement points of the retarding potential qU. The simulations show no preference towards any particular value. That appears unintuitive, since one would expect a narrower spacing to have beneficial effects on a distinct kink search. Yet, as mentioned in the last paragraph, the sterile neutrino signal is not localized, but manifests itself in relative count rate differences between the measurement points with a spectral feature as broad as the mass of the sterile neutrino m_h. Therefore, a larger step size does not weaken the sensitivity in principle, because the measurement time is distributed over less points. Anyway, it is in general recommended to use a step size lower then the smallest possible heavy neutrino mass, since otherwise it is possible that there are not enough vital measurement points above the kink.

The benefit of a TOF measurement can be explained in this context as follows: TOF spectra carry extra information about the differential energy distribution closely above each measurement point. That equates to knowledge about the slope of the integral spectrum at these measurement points. This would itself be equivalent to additional measurement points close to the existing ones but *without* removing measurement time from these.

4.3.4 Gated Filter Sensitivity

Figure 4.13 shows exemplary TOF spectra using Gated Filtering (GF, see section 3.3.3). It illustrates how GF works for a keV sterile neutrino search: without the gate (green points), the arrival time spectrum is isochronous. However, with activated gate, a certain portion is

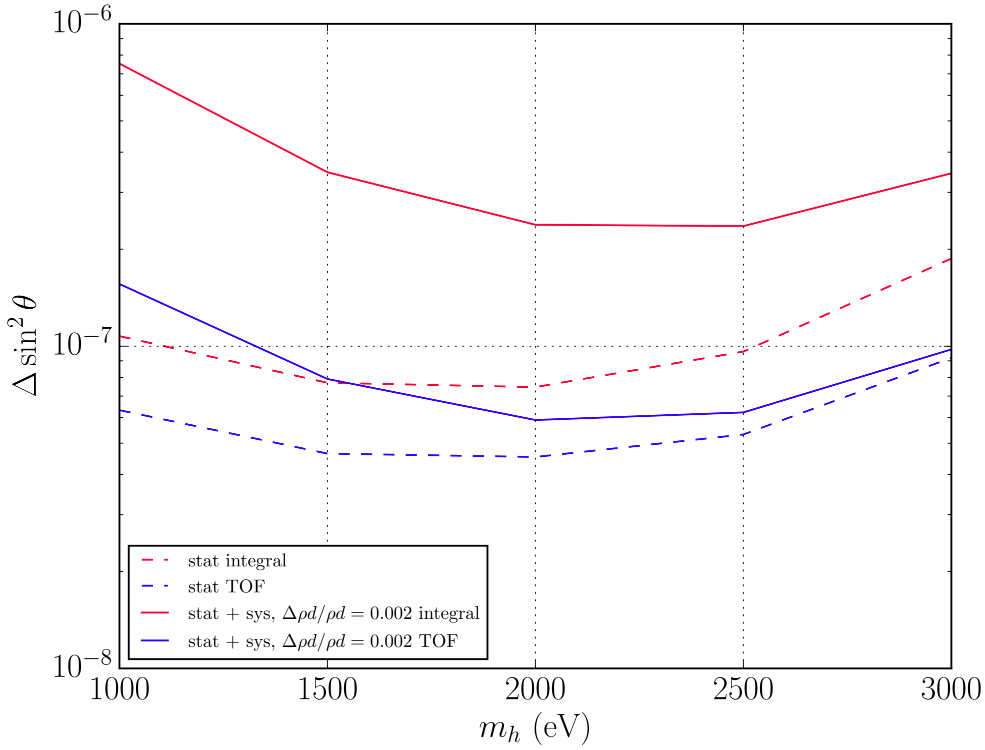

Figure 4.11: Same settings as in fig. 4.8 but with a measurement interval of [15; 18.5] keV. The narrowing of the measurement interval shows no benefit even if the sterile neutrino kink is within the interval.

cut away from the isochronous spectrum. For a given repetition time t_r and duty cycle ξ, the duration in which the gate is open is given by $t_r \cdot \eta$. The GF arrival time filter thus is smeared with a step function when compared to the raw TOF spectrum. Reducing the duty cycle ξ makes the arrival time spectrum approximate the TOF spectrum of fig. 4.9, however with a loss of overall rate. Electrons with a TOF greater than the repetition time t_r lead to pile-up, which can be seen in the first few bins. However, since TOF spectra at several keV below the endpoint are rather sharp, the effect of pile-up is small for repetition times of $\sim 10\,\mu$s.

Figure 4.14 shows the sensitivity for two exemplary gated filter setups with constant duty cycle. The scenario is based on the assumption that the existing focal plane detector (FPD) of KATRIN is used, which is optimized for a measurement near the endpoint of the β-spectrum and thus can not maintain much higher count-rates. The bottleneck is particularly the per-pixel rate which should not exceed $\sim 10^3$ cps within a window of $\sim \mu s$, because otherwise it would lead to pile-up. In this simulation, an exemplary overall reduction of the signal rate by a factor 10^5 has been chosen. The actual choice of the rate reduction factor will determine the absolute sensitivity, but should not change the relative sensitivity of the gated filter with respect to the integral mode largely. Since the gated filter periodically blocks the flux of electrons, the rate reduction factor can be made somewhat smaller with respect to the integral mode. However, due to the highly focussed nature of the arrival time spectra at lower duty cycles (fig. 4.8), the gain can not be as high as the total loss of events given by the duty cycle. Thus, the signal rates of all three setups in fig. 4.8 have been adjusted in that way, so that the count rate *at maximum* is the same in all settings. This is also indicated in

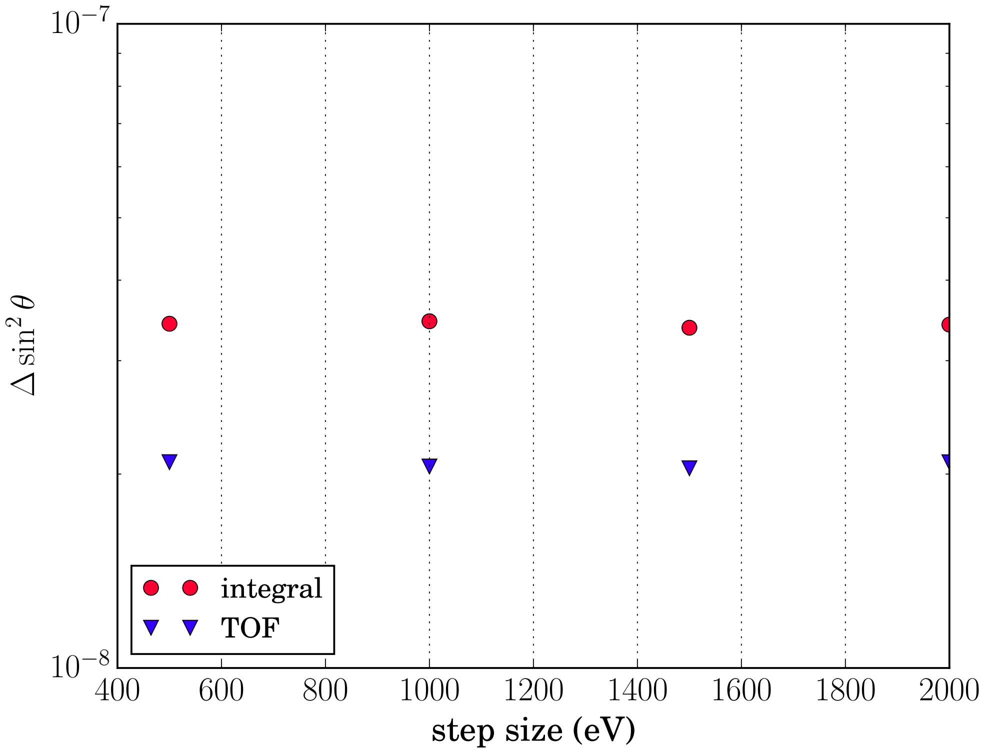

Figure 4.12: Statistical sensitivity as a function of the step size between measurement points of the retarding potential qU for a sterile neutrino with $m_h = 2$ keV. The measurement interval is [4; 18.5] keV for a total measurement time of three years.

fig. 4.13, where additionally the gated filter arrival time spectra for $\xi = 0.1$ and 0.02, scaled to the same maximum rate as the integral mode ($\xi = 1$), are shown (dotted lines). The repetition rate has been fixed at 10 μs, which has shown to be a good compromise between pile-up and signal loss. The measurement interval has been limited to [15; 18.5] keV since it is not believed to be viable to pulse the pre-spectrometer more than several keV.

It can be seen that none of the settings is able to achieve the same sensitivity as the integral mode, despite a slightly smaller difference between pure statistics and statistics plus systematics. It shows that the loss of statistics by the gated filter is simply too high to be compensated by beneficial effects of TOF. Especially fig. 4.13 suggests that, e.g., a duty cycle of 0.1 reduces the rate at maximum only by about one third, since the spectrum is dominated by fast electrons from higher energy regions of the β-spectrum. A further reduction to a duty cycle of 0.02 then leads to the desired reduction of the rate at maximum, manifesting itself in fig. 4.14 in a slightly improved sensitivity, but still not enough to beat the integral mode. However, assumptions about the maximal rate are in the scenario rather simplified and in reality more complex strategies are possible. With a better understanding of the detector response one might optimize the GF timing parameters further. Furthermore, if parts of the data are not significant for keV sterile neutrino search, e.g., such as the fast-electron peaks at the onset of the TOF spectra, an additional inhibit logic would allow to increase the detector base rate further.

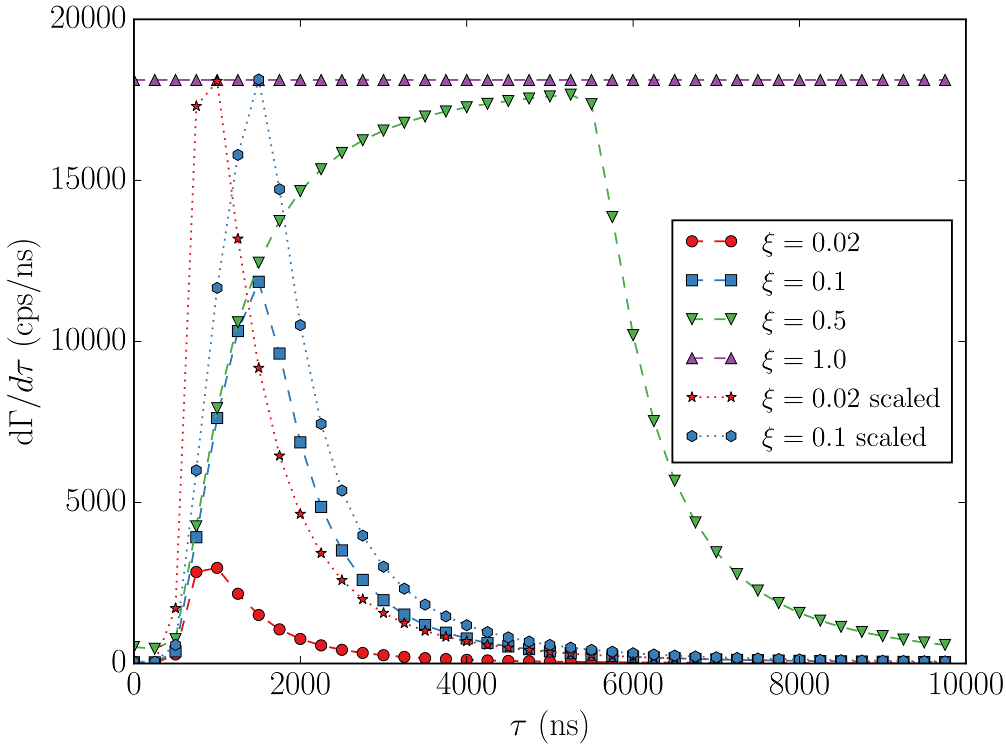

Figure 4.13: Exemplary Gated Filter arrival time spectra for different duty cycles. Retarding energy is $qU = 17\,\mathrm{keV}$ and repetition time $t_r = 10\,\mu\mathrm{s}$. The active-sterile mixing has been set to $\sin^2\theta = 0$. Activating the gate and decreasing the duty cycle cuts away portions of the arrival time spectrum, which is isochronous without gate. If the overall electron rate needs to be decreased in order to limit the maximum rate at the detector, the reduction factor can be smaller in case of the gated filter, which reduces the rate anyway. The plot also shows scaled spectra for $\xi = 0.1$ and 0.02 (dotted lines) with the same maximum rate as the integral mode ($\xi = 1$).

4.4 Summary and Discussion

It has been shown that TOF spectroscopy in a KATRIN context is in principle able to boost the sensitivity of the sterile neutrino search significantly. Fig. 4.11 suggests an improvement of up to half an order in terms of pure statistical uncertainty down to at maximum $\sin^2\theta \sim 5\times10^{-9}$ for a sterile neutrino of $m_h = 7\,\mathrm{keV}$ at one σ. If the exemplary systematic uncertainty of the inelastic scattering cross section is considered, the sensitivity is only mildly decreased in contrast to the integral mode, which is in that case outperformed by the TOF mode by over an order of magnitude. However, the practical realization of a sensitive TOF measurement method is still work in progress. In a simple model, the gated filter method is not able to compensate for its loss of statistics by reducing the maximal electron current for the existing focal plane detector due to a dominating amount of fast electrons (figs. 4.13 and 4.14). However, this issue could be mitigated by adding an inhibit logic to the focal plane detector and could thus make the gated filter method in combination with further optimizations superior to the integral mode. From a long-term point of view, the concept of an upgraded differential detector [Mer+15a] which is capable of extreme rates up to 10^{10} cps is very promising. If there is furthermore success in finding a sensitive TOF measurement method, a beneficial strategy could even be a combined measurement to elim-

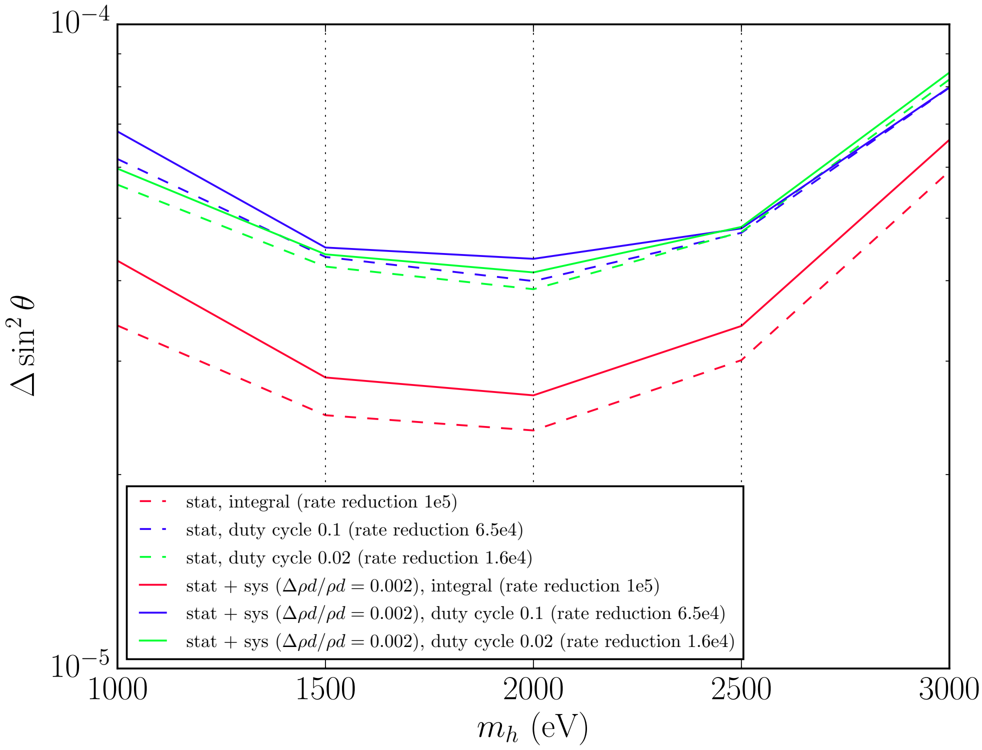

Figure 4.14: Sensitivity (1 σ) of realistic integral mode (red) compared with two gated filter TOF modes with different duty cycles (blue: 0.1, green: 0.02). Both statistical uncertainty (dashed lines) and combined uncertainty with exemplary systematics (full lines, see section 4.3.2) are plotted. The signal amplitude has been modified for each setting in order to keep the count-rate at maximum (within the bin width of 250 ns) constant at a factor of 10^{-5} of the normal count rate. Measurement interval has been [15; 18.5] keV for three years data taking. The repetition time is $t_r = 10\,\mu$s for all retarding potentials.

inate systematics and perform cross-checks by the two rather different differential methods.

Chapter 5

Right-Handed Currents with Sterile Neutrinos

Disclaimer: The results of this chapter have been published in the Journal of Cosmology and Astroparticle Physics (JCAP) [Ste+17b]. The chapter is based on the original draft, written by myself and edited by the co-authors of the paper. The original results of this analysis have been cross-checked and verified by my collaborators from Karlsruhe.

In the last chapter, the sensitivity of KATRIN to sterile neutrinos in the keV range has been discussed with the motivation to test the warm dark matter paradigm. While the interest in this is a rather recent development in the collaboration, there have been in the past already some publications regarding the KATRIN sensitivity to sterile neutrinos on the eV scale [FB11; SH11; EP12], motivated by the short baseline oscillation anomalies (section 1.5.2). Another interesting field where KATRIN might set new limits are neutrino interactions beyond the standard model. Especially the sensitivity to weak non-$V-A$ contributions, e.g. right-handed currents, has been studied in several publications [SGM00; SBN06; Bon+11; SHW11; BHR14]. These can be treated phenomenologically independent from other phenomena, but it is also worthwhile to study models in which some of these arise naturally. One of these is the left-right symmetric model (LRSM) which has already been outlined in section 1.5.5. To recapitulate briefly, the LRSM adds an additional $\mathrm{SU}(2)_\mathrm{R}$ symmetry acting only on right-handed fermion fields, analogous to the left-handed $\mathrm{SU}(2)_\mathrm{L}$ of the standard model, thus restoring parity on high energy scales. The $\mathrm{SU}(2)_\mathrm{R}$ is mediated by right-handed W and Z bosons, where current experimental mass limits on the right-handed W from the LHC approximately give $m_{W_R} \gtrsim 3\,\mathrm{TeV}$ [CMS14; ATL12].

In this chapter, the statistical sensitivity of KATRIN will be determined for a combined scenario of right-handed currents with light sterile neutrinos on the eV scale. On this scale, there are in principle no modifications of the hardware and the data acquisition required, which means that the analysis can be performed just with the data of the primary neutrino mass measurement runs. The scenario is motivated by the LRSM but shall be addressed in a way which is as model-independent as possible. Nevertheless, the results will be discussed with respect to the parameter space of the LRSM which is not yet experimentally excluded. The results have been submitted for publication [Ste+17b].

5.1 Tritium β-Decay with Left-Right-Interference

In the following, the tritium β-decay spectrum of KATRIN (2.1) will be modified to include right-handed currents and eV scale sterile neutrinos, based on the LRSM. The kinematics of the modified β-spectrum will be discussed thereafter.

5.1.1 Tritium β-Decay

The LRSM assumes in most modern formulations three additional sterile neutrinos [BR13]. While naturally the sterile neutrino masses are assumed to be beyond the TeV scale to maintain the seesaw mechanism, it is also possible to have at least one light sterile neutrino [Bor16]. As in the following study the scenario of eV scale sterile neutrinos in conjunction with right-handed currents is investigated, one additional mass state $m_4 \sim \mathcal{O}(\mathrm{eV})$ is included. Again, as done in the last chapter for the keV scale sterile neutrino scenario, the *light neutrino mass* or *electron neutrino mass* can be defined as $m_l^2 \equiv \sum_{i=1}^{3} |U_{\mathrm{e}i}|^2 m_i^2$, since the light mass eigenstates 1, 2, 3 are not distinguishable by KATRIN. The *heavy neutrino mass* or *sterile neutrino mass* is then, again, defined as $m_h \equiv m_4$ and the *active sterile mixing angle* θ as $\sin^2\theta \equiv |U_{\mathrm{e}4}|^2$.

The modified β-spectrum with included right-handed currents based on a left-right symmetry has been derived in [BHR14] for a general case and been adopted for the special case of one sterile neutrino with keV mass. In the following, the same result of the derivation is used and a similar strategy this particular scenario is applied. The three light mass states are approximated by a single state m_l as defined above and only one sterile state m_h is taken into account. Furthermore the possibility of CP-violating phases in the neutrino mixing matrix is ignored. The mixing matrix (1.9) then becomes a plain 2×2 rotation matrix. Additionally, since the measurement takes place on the eV scale, one has to take into the account the contribution of right-handed lepton vertices on the light neutrino, which has been neglected in [BHR14] (eq. 3.10). The β-spectrum then takes the form

$$
\begin{aligned}
w(E) = \sum_j P_j \cdot \Bigg[& w_{h_j}(E) \cdot (a_{\mathrm{LL}}\ \sin^2\theta + a_{\mathrm{RR}}\ \cos^2\theta) \\
& + w_{l_j}(E) \cdot (a_{\mathrm{LL}}\ \cos^2\theta + a_{\mathrm{RR}}\ \sin^2\theta) \\
& + w_{h_j}(E) \cdot \frac{m_h}{E_0 - V_j - E} \cdot \frac{m_\mathrm{e}}{m_\mathrm{e} + E}\, a_{\mathrm{LR}}\ \cos\theta \sin\theta \\
& - w_{l_j}(E) \cdot \frac{m_l}{E_0 - V_j - E} \cdot \frac{m_\mathrm{e}}{m_\mathrm{e} + E}\, a_{\mathrm{LR}}\ \cos\theta \sin\theta \Bigg] ,
\end{aligned}
\tag{5.1}
$$

where the abbreviations $w_{l_j}(E)$ and $w_{h_j}(E)$ denote j-th final state component of the β-spectrum (2.1) with only one light neutrino m_l and one heavy neutrino m_h, respectively. The abbreviation $w(E)$ for the β-spectrum and its components has been introduced for more clarity due to a large number of subscripts and indices. The last two terms originate from interference between left- and right-handed interactions and have a distinct kinetic behavior with the additional factors $m_\nu/E_\nu = m_\nu/(E_0 - V_j - E)$ and $m_\mathrm{e}/E_\mathrm{e} = m_\mathrm{e}/(E + m_\mathrm{e})$. The interference terms for the light neutrino and the heavy neutrino have different signs, respectively, arising from the columns in the 2x2 mixing matrix. The coefficients are defined as

$$a_{\mathrm{LL}} = 1 + 2C \tan\xi \cos\alpha\ , \tag{5.2}$$

$$a_{\mathrm{RR}} = \frac{m_{\mathrm{W_L}}^4}{m_{\mathrm{W_R}}^4} + \tan^2\xi + 2C \frac{m_{\mathrm{W_L}}^2}{m_{\mathrm{W_R}}^2} \tan\xi \cos\alpha\ , \tag{5.3}$$

$$a_{\mathrm{LR}} = -2 \left(\frac{m_{\mathrm{W_L}}^2}{m_{\mathrm{W_R}}^2} + C \tan\xi \cos\alpha \right) \tag{5.4}$$

and

$$C = \frac{g_V^2 - 3g_A^2}{g_V^2 + 3g_A^2} \simeq -0.65 \,, \tag{5.5}$$

where ξ is the mixing angle between left- and right-handed W bosons and α a *CP*-violating phase of the W_L/W_R-mixing. Furthermore, the possibility of complex phases involved in active-sterile mixing will be neglected, so the coefficients for the LR term both for the sterile and the active neutrino differ only by the mass. Regarding the current experimental limits on these coefficients, the key observable is the right handed W_R mass which also sets boundaries on the mixing angle ξ [BR13]. The most robust bound comes from the LHC, which roughly states $m_{W_R} \gtrsim 3$ TeV [ATL12; CMS14]. Since m_{W_R} and $|\xi|$ are connected via the charged boson mixing matrix [LS89], this translates into a bound on the LR mixing angle of about $|\xi| \lesssim 10^{-3}$.

5.1.2 Model-Independent Parametrization

The theoretical spectrum (5.1) has two disadvantages for practical right-handed current searches in tritium β-decay. On one hand it is highly dependent on the underlying left-right symmetrical model. In this scenario a right-handed current contribution can only be present if there is active-sterile mixing, as can be seen in the a_{LR} terms in (5.1). However, on different underlying theoretical considerations there can also be an identical signature without sterile contribution, e.g., by non-trivial scalar, pseudoscalar and tensor couplings [Bon+11; SG98]. On the other hand, the number of parameters in (5.1) is higher than the degrees of freedom, which is problematic for a fit.

Thus, the aim is to transform (5.1) in order to come up with a model-motivated, yet model-independent parametrization. One can then highlight the effective resulting shape of the β-spectrum. That is accomplished by introducing an effective mixing angle θeff through

$$(a_{\mathrm{LL}} + a_{\mathrm{RR}}) \sin^2 \theta_{\mathrm{eff}} = a_{\mathrm{LL}} \sin^2 \theta + a_{\mathrm{RR}} \cos^2 \theta \tag{5.6}$$

$$(a_{\mathrm{LL}} + a_{\mathrm{RR}}) \cos^2 \theta_{\mathrm{eff}} = a_{\mathrm{LL}} \cos^2 \theta + a_{\mathrm{RR}} \sin^2 \theta \,. \tag{5.7}$$

Furthermore, the interference terms in (5.1) can be parametrized by

$$c_{\mathrm{LR}} = \frac{a_{\mathrm{LR}}}{a_{\mathrm{LL}} + a_{\mathrm{RR}}} \cdot \frac{m_{\mathrm{e}}}{m_{\mathrm{e}} + E_0} \cos\theta \sin\theta \,, \tag{5.8}$$

where $m_{\mathrm{e}}/(m_{\mathrm{e}} + E)$ has been approximated by $m_{\mathrm{e}}/(m_{\mathrm{e}} + E_0)$ for a measurement near the endpoint. In the following, c_{LR} denotes the effective left-right interference strength. It can also be negative and acts effectively as a Fierz parameter. Note that while the interference strength is independent of the effective mixing angle as a fit parameter, it is still dependent on the *physical* mixing angle. Since the values for a_{LL} will be close to 1 and for a_{LR} and a_{RR} close to 0, the effective mixing angle will correspond roughly to the physical mixing angle. The resulting shape of the β-spectrum is then

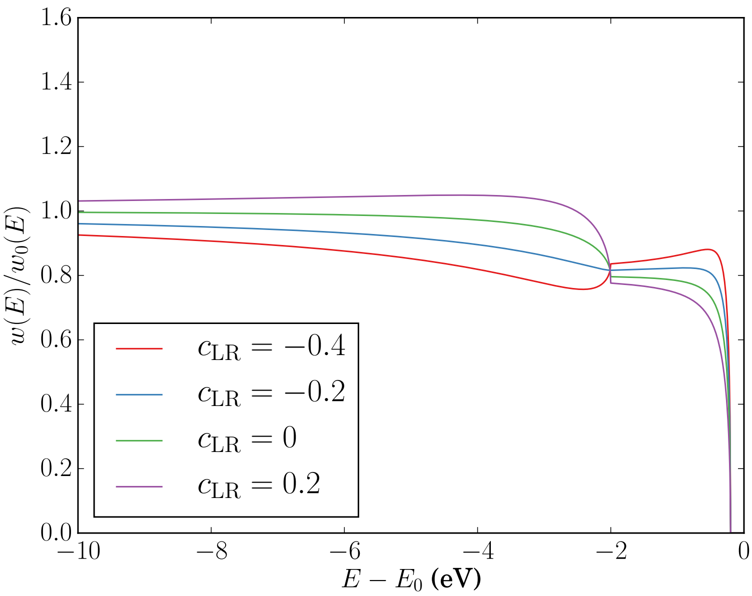

Figure 5.1: β-spectrum ratio $w(E)/w_0(E)$ near the endpoint for different left-right interference strengths c_{LR} for effective mixing angle $\sin^2\theta_{\mathrm{eff}} = 0.2$, sterile neutrino mass $m_h = 2$ eV and light neutrino mass $m_l = 0.2$ eV. For simplicity, only the $V_j = 0$ component of the β-spectrum has been used. Figure first published in [Ste+17b].

$$\begin{aligned} w(E) = \sum_j P_j \Bigg[& w'_{h_j}(E) \cdot \sin^2\theta_{\mathrm{eff}} + w'_{l_j}(E) \cdot \cos^2\theta_{\mathrm{eff}} \\ & + c_{\mathrm{LR}} \cdot \left(w'_{h_j}(E) \cdot \frac{m_h}{E_0 - V_j - E} - w'_{l_j}(E) \cdot \frac{m_l}{E_0 - V_j - E} \right) \Bigg] , \end{aligned} \tag{5.9}$$

where the global factor $(a_{LL} + a_{RR})$ has been absorbed into the decay amplitude

$$w'_{l_j}(E) = (a_{\mathrm{LL}} + a_{\mathrm{RR}}) \cdot w_{l_j}(E) \tag{5.10}$$

$$w'_{h_j}(E) = (a_{\mathrm{LL}} + a_{\mathrm{RR}}) \cdot w_{h_j}(E) \,. \tag{5.11}$$

As outlined in the last section it may be possible that an effect on the β-spectrum with the same shape as the mixed terms in (5.9) might be produced by a mechanism not based on left-right symmetry which can then be independent of the sterile mixing angle. The re-parametrized spectrum is model-agnostic and fits to a complete class of theoretical scenarios which predict the same term $\propto m_\nu/E_\nu$ with the effective Fierz parameter c_{LR} [SGM00].

5.1.3 Discussion of Shape and Parameter Dependencies

Since we are interested in the effective shape of the spectrum with right-handed currents (5.9) in relation to the standard β-spectrum (2.1), the expression $w(E)/w_0(E)$ will be studied, where $w_0(E)$ is the β-spectrum (5.9) with zero neutrino masses $m_l = m_h = 0$. For simplicity, only the electronic ground state $V_i = 0$ in (2.1) has been taken into consideration. It is plotted as a function of the energy for different eff. left-right interference strengths c_{LR} in

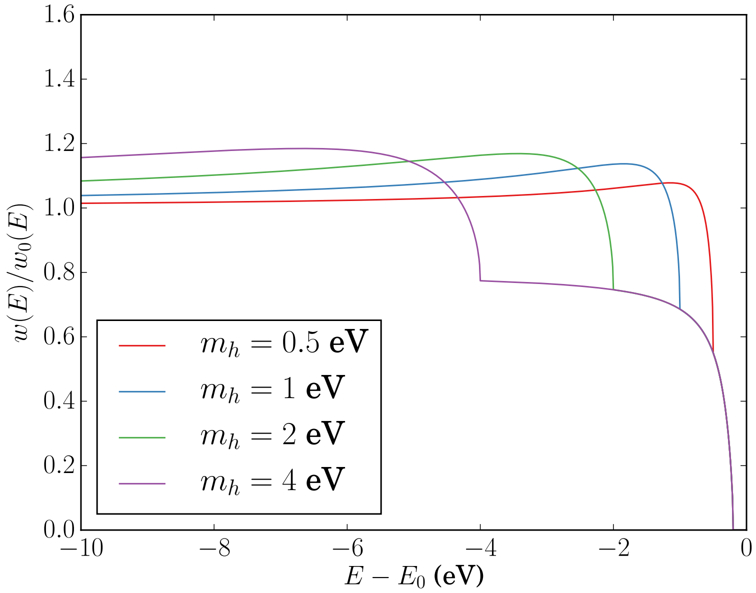

Figure 5.2: β-spectrum ratio $w(E)/w_0(E)$ near the endpoint for effective mixing angle $\sin^2\theta_{\text{eff}} = 0.2$, left-right interference strength $c_{\text{LR}} = 0.5$ and light neutrino mass $m_l = 0.2$ eV. For simplicity, only the $V_j = 0$ component of the β-spectrum has been used. Figure first published in [Ste+17b].

fig. 5.1. For $c_{\text{LR}} = 0$ the plot shows the step-like signatures of the light (active) and sterile neutrino mass, m_l and m_h, respectively. A non-vanishing c_{LR} leads either to a boost or a suppression in the regions close to the endpoint minus the neutrino masses, depending on the sign of c_{LR}. Due to the different sign of active and sterile interference terms (5.9), a boost of the sterile part means a suppression of the active part and vice versa. The effect is slightly more pronounced for the sterile neutrino than for the active one. This is because the terms with c_{LR} are proportional to the mass of the respective neutrino. To demonstrate the mass-dependency, the same expression is plotted in fig. 5.2 for a fixed $c_{\text{LR}} = 0.2$ as a function of the sterile neutrino mass m_h. It can be seen that the magnitude of the boost stays roughly the same at the peak, but becomes approximately proportional to m_h with growing distance to the endpoint. That means also that the boost becomes more spatially extended in the decay spectrum for higher neutrino masses. In reality, the signature is washed out to some extent by the final state distribution in (2.1). Furthermore, in a tritium β-decay experiment using an integrating spectrometer, such as KATRIN, the differential β-decay spectrum is not accessible directly. Instead, the integral β-decay spectrum is measured, where the differential spectrum is convolved with the transmission function of the KATRIN main spectrometer [Pic+92; KAT04]. Together with additional experimental corrections, such as inelastic scattering of electrons in the source, it basically defines the response function of KATRIN, which will be looked at in more detail in the next section.

5.2 KATRIN Sensitivity

In the following section the derived knowledge on the signature of right-handed currents with sterile neutrinos will be applied to the experimental parameters of the KATRIN experiment [KAT04] in order to estimate its sensitivity.

5.2.1 Prerequesites

KATRIN Setup and Response

In contrast to the last two chapters, the KATRIN sensitivity to right-handed currents in conjunction with eV scale sterile neutrinos will not be determined for the TOF mode but only for the integral mode. This particular scenario has not been addressed before and while investigating it in the context of a TOF mode may be interesting, the simulation would be more complicated due to a large number of free parameters. Unless there is success in establishing a working tagger setup, there is not enough motivation yet for such a simulation.

The KATRIN integral β-spectrum with right-handed currents in the presence of sterile neutrinos can be obtained from (2.11), where the classic β-spectrum (2.1) has to be replaced by the expression derived in (5.9), yielding

$$R(qU) = \epsilon \cdot \frac{\Delta\Omega}{4\pi} \left(\int_{qU}^{E_0} \mathrm{d}E \; w(E) \cdot T'(E, U) \right) + b, \tag{5.12}$$

with the accepted solid angle $\frac{\Delta\Omega}{4\pi}$ with $\vartheta_{\mathrm{max}} = 50.77°$ and the background rate b. Again, a factor ϵ is taken into account to model various approximately energy-independent losses, which are in this case the fraction of the transmitted flux tube of the WGTS, $\epsilon_{\mathrm{flux}} \approx 0.83$, and the detector efficiency $\epsilon_{\mathrm{det}} \approx 0.9$. The response function is given by eq. (2.12).

The resulting integral spectrum (5.12) is shown in fig. 5.3 for different sterile neutrino masses and effective left-right interference strengths. The final state distribution has been taken from [SJF00] and the energy loss spectrum from [Ase+00]. Due to integration in combination with these experimental effects, the signature is clearly more washed out than in the differential spectrum (5.9). Nevertheless, for large enough values there is still a distinct effect on the shape, sufficiently large to be detected with the high precision experiment KATRIN. As with in the differential β-spectrum, the existence of right-handed currents is manifest as a boost or suppression in a region close to the endpoint, for a positive or negative c_{LR}, respectively. The strength of the signature increases with the sterile mass m_h as well. Furthermore, the plot suggests that for a lower sterile neutrino mass the boost (or suppression) is more localized than for a higher sterile neutrino mass. In the example with $m_h = 4\,\mathrm{eV}$ in fig. 5.3, the boost region clearly stretches down below the KATRIN default lower measurement interval bound of $qU = E_0 - 25\,\mathrm{eV}$ [KAT04].

Analysis Method

From the integral spectrum (5.12) and consequently the likelihood shape, we want to derive the sensitivity on the left-right interference c_{LR} after the default measurement time period of three effective years (corresponding to five calendar years) with KATRIN. The sensitivity of a parameter is in our context identified with the uncertainty or upper limit of its fit estimate with respect to a fiducial input value, given by the null hypothesis (i.e. $c_{\mathrm{LR}} = 0$). Due to a larger number of fit parameters in the scenario of added light sterile neutrinos and right-handed currents and the possibility of a complex fit parameter distribution with non-Gaussian errors and non-linear correlations, a Bayesian approach has been chosen instead of the common frequentist paradigm. This has been performed using a Markov Chain Monte Carlo (MCMC) analysis with the likelihood function

$$\log L(\theta) = -\frac{1}{2} \sum_{i=1}^{m} \frac{(n_i(\Theta) - n_i(\Theta_0))^2}{n_i(\Theta)} \; , \tag{5.13}$$

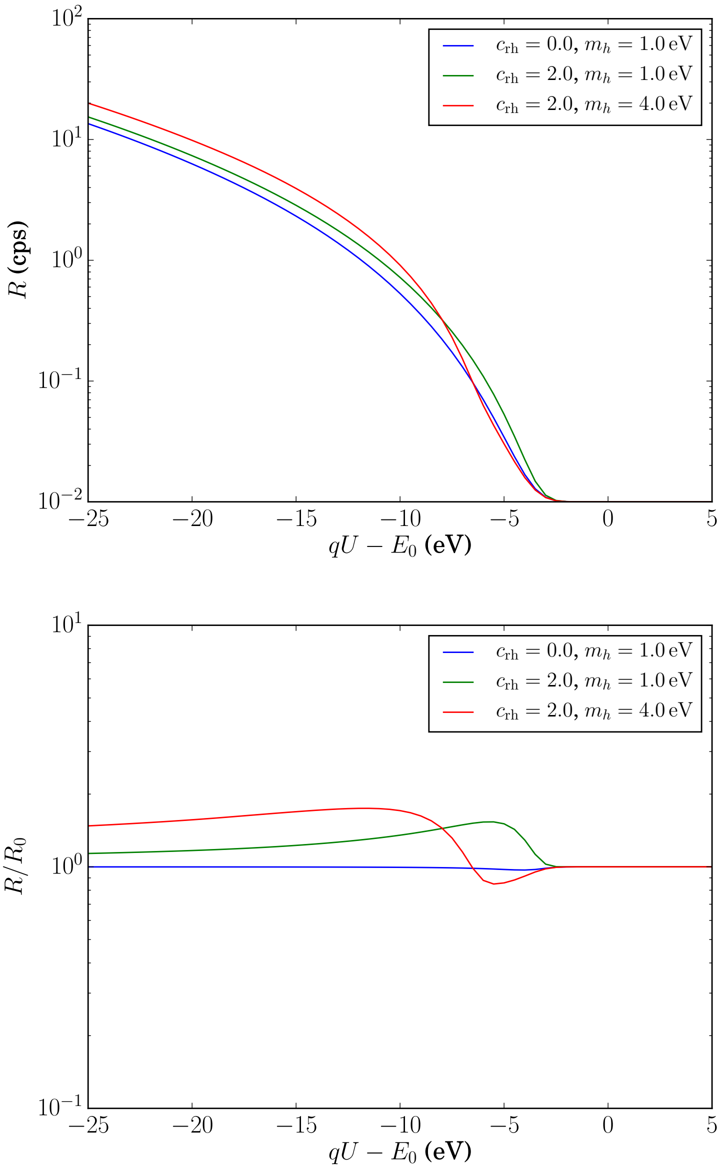

Figure 5.3: Integral spectrum $R(qU - E_0)$ of KATRIN (5.12) (upper plot) for different exemplary scenarii with exaggerated eff. left-right interference strength c_{LR} and different sterile ν masses m_h. The effective mixing is $\sin^2\theta = 0.2$ and the electron neutrino mass $m_l = 0$, plus a uniform background of $b = 10\,\mathrm{mcps}$. The lower plot shows the ratio R/R_0, where R_0 is the integral β-spectrum with $c_{\mathrm{LR}} = 0$ and $m_h = 0$. The endpoint is smeared and effectively lowered due to rotational-vibrational excitations of the daughter molecule with an average energy of 1.7 eV [SJF00]. The effect of a positive c_{LR} can be seen as a boost in a region below the endpoint, where the strength and average stretch of the boost is determined by the sterile mass m_h. The relative suppression at $\sim -5\,\mathrm{eV}$ with the red curve is an effect of $\cos^2\theta\mathrm{eff} < 1$, visible for sufficiently large m_h. Figures first published in [Ste+17b].

with variable parameters Θ and null-hypothesis Θ_0. Such a likelihood function utilizes the null-hypothesis instead of toy data, but effectively approximates the posterior distribution of possible data-sets. The expected counts in each bin n_i are given by the integral β-spectrum (5.12) as

$$n_i = t_i \cdot R(qU_i) \;, \tag{5.14}$$

with a set of m measurement points qU_i with measurement time t_i, respectively. For the measurement time distribution t_i the proposed distribution for in [KAT04] with a lower interval bound of $qU_1 = E_0 - 25\,\text{eV}$ has been used, assuming that the main measurement objective of KATRIN will be the measurement of the active neutrino mass m_l. With the fit function (5.14), the parameters of the model are

- the β-decay spectral endpoint E_0,
- the active neutrino mass m_l,
- the sterile neutrino mass m_h,
- the effective mixing angle $\sin^2\theta_{\text{eff}}$,
- the effective left-right interference strength c_{LR}
- the decay amplitude S and
- the background rate b.

For the simulations the Differential Evolution Markov Chain Monte Carlo (DEMC) algorithm [Ter06] has been used. DEMC is an ensemble-based MCMC method, where instead of a single Markov chain an ensemble of N chains is run. The proposal for each step in chain j at iteration t is generated by adding the difference of two other randomly selected chains, multiplied with a scaling parameter γ,

$$\theta'_{j,t+1} = \theta_{j,t} + \gamma(\theta_{k,t} - \theta_{l,t}) \qquad j \neq k \neq l \;. \tag{5.15}$$

The proposal is then accepted or rejected with the classic Metropolis Hastings criterion [Has70]. This scheme solves two problems with the classic Metropolis algorithm, which is the choice of the scale and the orientation for the proposal distribution. Instead of tuning these by hand, these are here implicitly derived from the ensemble at each iteration. This is especially useful in cases where the posterior distribution shows a high correlation between parameters.

Regarding the scaling parameter, the recommendation by [Ter06] has been used in the implementation, which states $\gamma = 2.38/\sqrt{(2D)}$, where D is the dimension of the parameter space. In most cases this choice should provide an optimal acceptance ratio. The remaining tuning parameter is then the number of chains N, which should at least be $N = 2D$ and needs to be increased for more complex posterior distributions. No explicit Bayesian prior has been chosen, only the physical parameter boundaries have been enforced which are particularly $m_l, m_h > 0$ and $0 < \sin^2\theta_{\text{eff}} < 1$. To check convergence, the Gelman Rubin R diagnostic [GR92] has been used. Also denoted as potential scale reduction factor (PSRF), this is defined as the ratio of pooled variance V and the within-chain variance W,

$$R = \frac{V}{W} \;, \tag{5.16}$$

where the pooled variance is a function of W and the between-chain variance B,

$$R = \frac{L-1}{L} W + \frac{N+1}{NL} B \;, \tag{5.17}$$

with L denoting the number of samples per chain. Within-chain variance W and between-chain variance B are defined by

$$B = \frac{L}{N-1} \sum_{m=1}^{N} (\hat{\theta}_m - \hat{\theta})^2 \tag{5.18}$$

$$W = \frac{1}{N} \sum_{m=1}^{N} \sigma_m^2 , \tag{5.19}$$

where $\hat{\theta}_m$ is the sample posterior mean and σ_m^2 the variance of the m-th chain. The overall sample posterior mean $\hat{\theta}$ is defined as $\hat{\theta} = (1/N) \sum_{m=1}^{N} \hat{\theta}_m$. If the chains have converged, R should be close to one. A common convergence criterion is e.g. $R < 1.1$. However, due to strong non-linear correlations in the posterior distributions under investigation, the condition has been tightened to $R < 1.01$. This has been fulfilled in all cases, except with a free neutrino mass parameter (see below). All results have been cross-checked and could be reproduced with an independent simulation based on a classic Metropolis Hastings [Has70] algorithm without adaption. However, using the latter requires careful manual fine-tuning of the proposal distributions.

5.2.2 Results

Credible Intervals

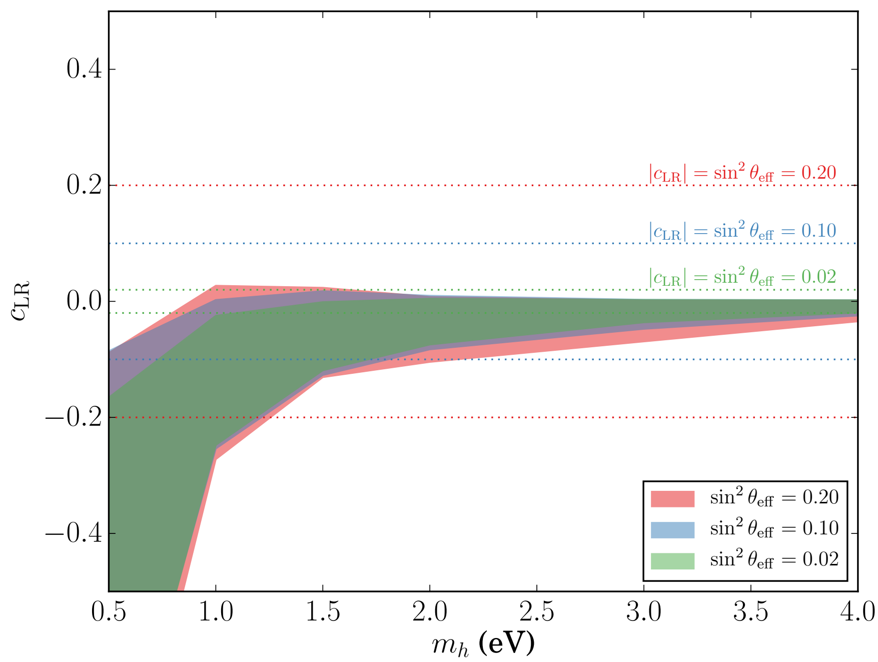

Figure 5.4: Bayesian credible intervals (95 % credibility level) on null hypothesis (5.13) for effective left-right interference strength $c_{\mathrm{LR}} = 0$ as a function of fixed sterile neutrino mass m_h with different effective mixing angles $\sin^2\theta_{\mathrm{eff}}$. The null hypothesis further includes $m_h = 0$, $E_0 = 18.575$ keV, $b = 10$ mcps and the KATRIN default signal amplitude. The dotted horizontal lines represent the hard limit of $|c_{\mathrm{LR}}| < \sin^2\theta_{\mathrm{eff}}$ in case of LR symmetry. Figure first published in [Ste+17b].

Figure 5.4 shows the 95 % credible interval of the effective left-right interference strength c_{LR}, given a null-hypothesis of $c_{\mathrm{LR}} = 0$ in (5.13) for different sterile neutrino masses and effective mixing angles with light neutrino mass of $m_l = 0$, background rate of $b = 10$ mcps and the KATRIN default signal amplitude. The sterile neutrino mass has been fixed in the MCMC runs, so the plot can be interpreted as statistical sensitivity on an excess at a certain mass m_h. The results are based on DEMC runs with 20000 iterations in each chain and an ensemble size $N = 4D$. Several pieces of information can be extracted from the plot. The average width of the interval varies from about 0.5 to 0.05 in terms of c_{LR}. One of the most distinct features is a strong bias. For a mass of $m_h = 0.5$ eV the null-hypothesis is not even in the 95 % credible interval. There is no a priori reason to not expect a bias. It can be attributed to a *volume effect* in the space of the posterior. While the point of maximum likelihood is indeed identical with the fiducial point Θ_0 (within a small numerical uncertainty), the marginalized posterior in the c_{LR} subspace has its maximum at $c_{\mathrm{LR}} \neq 0$, since it is integrated over all other dimensions. This will be looked at in more detail in the next subsection.

Besides that, a very strong dependence on the mass of the sterile neutrino can be seen, where the sensitivity improves drastically for heavier sterile neutrinos. This is prima facie a consequence of the proportionality of the left-right mixing terms in (5.9) to the neutrino mass. But besides that, for small sterile neutrino masses the interference terms for the active and sterile part cancel each other partly since they have opposite signs. Furthermore, the information about left-right interference, active-sterile mixing and the active neutrino mass is distributed in a broader region of the spectrum if the sterile neutrino mass is heavier. The sensitivity is less dependent on the effective mixing angle. However, smaller mixing angles seem to be slightly favorable. This is plausible, since the left-right interference term in (5.9) depends only on the sterile mass, not on the eff. mixing angle. A smaller eff. mixing angle is thus expected to lead to a slightly clearer right-handed current signature. Nevertheless, for each effective mixing angle there is also a theoretical boundary for c_{LR}, if LR symmetry is assumed. From eqs. (5.6), (5.7) and (5.8) we can conclude a hard limit $|c_{\mathrm{LR}}| < \sin^2\theta_{\mathrm{eff}}$, which is also shown in fig. 5.4.

Parameter Correlations

A closer understanding of these observations can be accomplished by studying the parameter correlations in the posterior distribution. Figures 5.5 and 5.6 show the marginalized posterior distributions for $\sin^2\theta_{\mathrm{eff}} = 0.1$ with $m_h = 1$ eV and $m_h = 4$ eV, respectively. Two things are worth noticing.

First, the distributions are significantly broader in the $m_h = 1$ eV case for all parameters except the background rate. Especially the effective mixing angle reaches zero in a large number of samples. This suggests that for a low sterile neutrino mass, the signatures of an active neutrino, a sterile neutrino and the right-handed current, along with an unknown endpoint, are too close to be distinguished. This is different in the case of $m_h = 4$ eV, where more distinct linear correlations can be seen, but in total the parameter signatures are well distinguishable. This argument is sound in light of the findings from the last section, where a larger sterile neutrino mass has been shown to increase both the strength and the width of the right-handed current signature.

Second, there is a strong linear correlation between the endpoint and the left-right interference strength. This correlation is weakened in the case of $m_h = 4$ eV and the point of highest density is closer to the fiducial null-hypothesis value (blue lines). Especially in the latter case there is a significant asymmetry which favors a lower left-right interference strength c_{LR} and a higher endpoint. That means most likely that changes in this direction

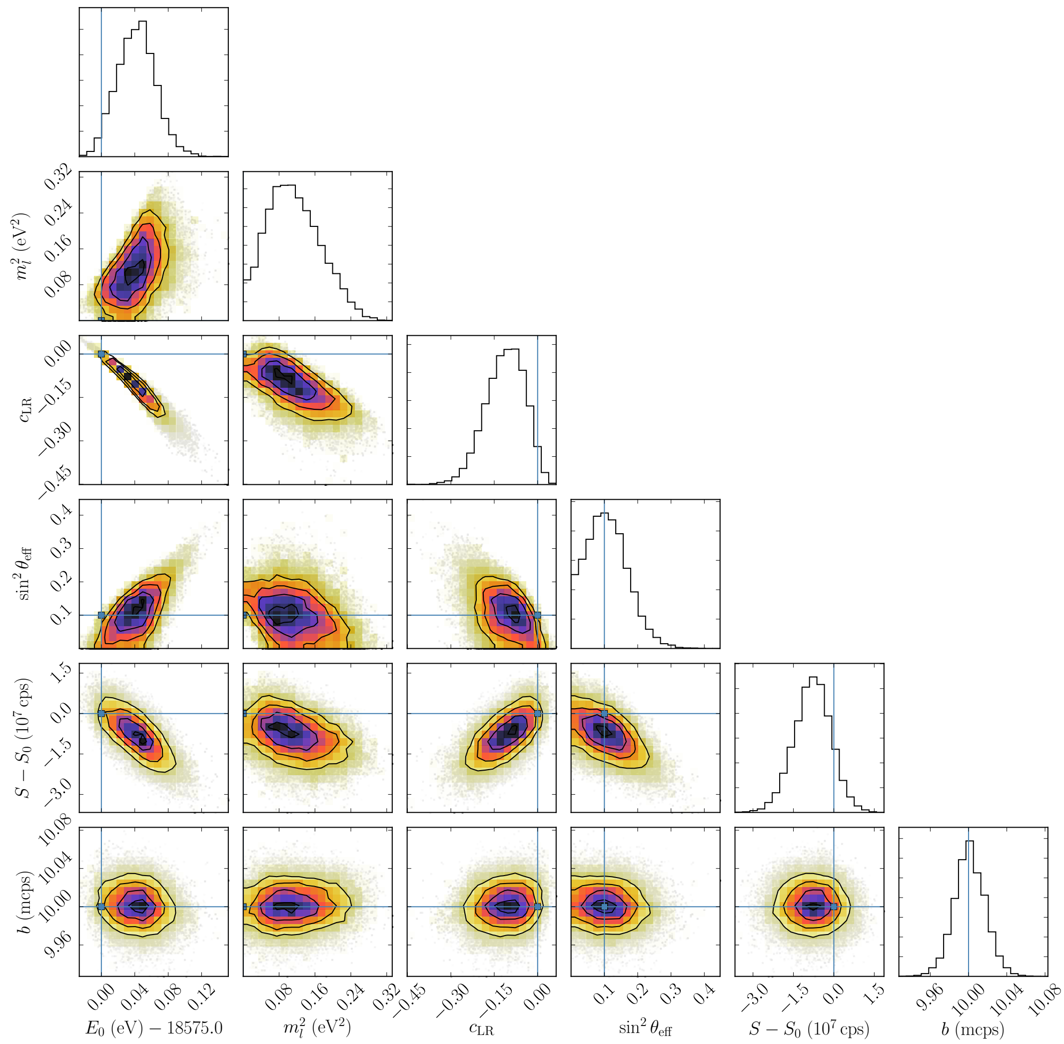

Figure 5.5: Marginalized posterior distributions for MCMC run with fixed sterile neutrino mass $m_h = 1$ eV, effective mixing angle $\sin^2\theta_{\mathrm{eff}} = 0.1$ and left-right interference strength $c_{\mathrm{LR}} = 0$ for all combinations of the free fit parameters used. Contours are 0.5, 1, 1.5 and 2 σ, respectively. The blue lines show the fiducial values. Strong correlation between effective left right interference strength c_{LR} and β-decay endpoint E_0 can be observed. The Gelman Rubin statistic R is well below 1.01 for all parameters. Figure first published in [Ste+17b].

are possible to compensate by choices of the other parameters but not vice versa. This leads to the supposition that endpoint-interference-correlation plays a central role in the volume effect, leading to the bias observed in fig. 5.4.

Fixed Endpoint

The influence of the endpoint-interference correlation on the bias has been confirmed by repeating the simulation with a fixed endpoint, fig. 5.7. The bias is reduced to a minimum. Further, the credible intervals narrow significantly, nearly by an order of magnitude. The sensitivity is still slightly better without sterile contribution, but not significantly. Fig. 5.8 shows the corresponding marginal posterior distributions for $m_h = 1$ eV. There is still a big uncertainty on the effective mixing angle. It continues to be correlated with the active neutrino mass, where the spectral shape consistent with the null hypothesis of an effective

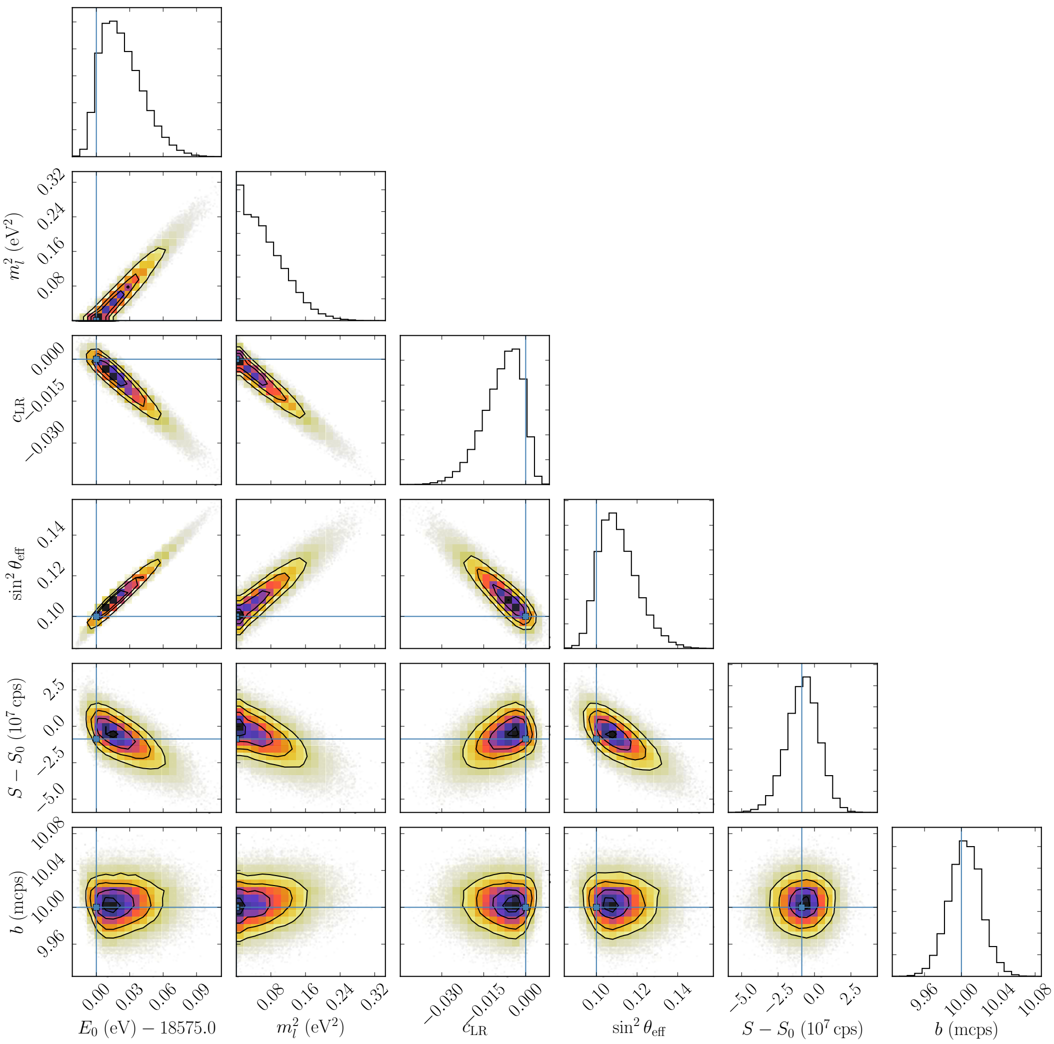

Figure 5.6: Marginalized posterior distributions for MCMC run with fixed sterile neutrino mass $m_h = 4\,\mathrm{eV}$, effective mixing angle $\sin^2\theta_{\mathrm{eff}} = 0.1$ and left-right interference strength $c_{\mathrm{LR}} = 0$ for all combinations of the free fit parameters used. Contours are 0.5, 1, 1.5 and 2 σ, respectively. The blue lines show the fiducial values. The correlation between effective left right interference strength c_{LR} and β-decay endpoint E_0 becomes slightly weaker. The correlations between c_{LR} and the sterile neutrino parameters $\sin^2\theta_{\mathrm{eff}}$ and m_h as well as the light neutrino mass m_l become more distinct. However, with all correlated parameters the uncertainty decreases. The Gelman Rubin statistic R is well below 1.01 for all parameters. Figure first published in [Ste+17b].

mixing $\sin^2\theta_{\mathrm{eff}} = 0.1$ can also be interpreted as a non-vanishing active neutrino mass. However, the distribution in the c_{LR}-space is now unbiased and symmetric, since no other parameter choices are now possible any more which would fake a right handed current signature.

Constrained Endpoint

That leads to the question, if it is possible to constrain the endpoint by external measurements [Str+14], how such a constraint will influence the sensitivity quantitatively. To this end, the initial likelihood function (5.13) is modified by a prior on E_0,

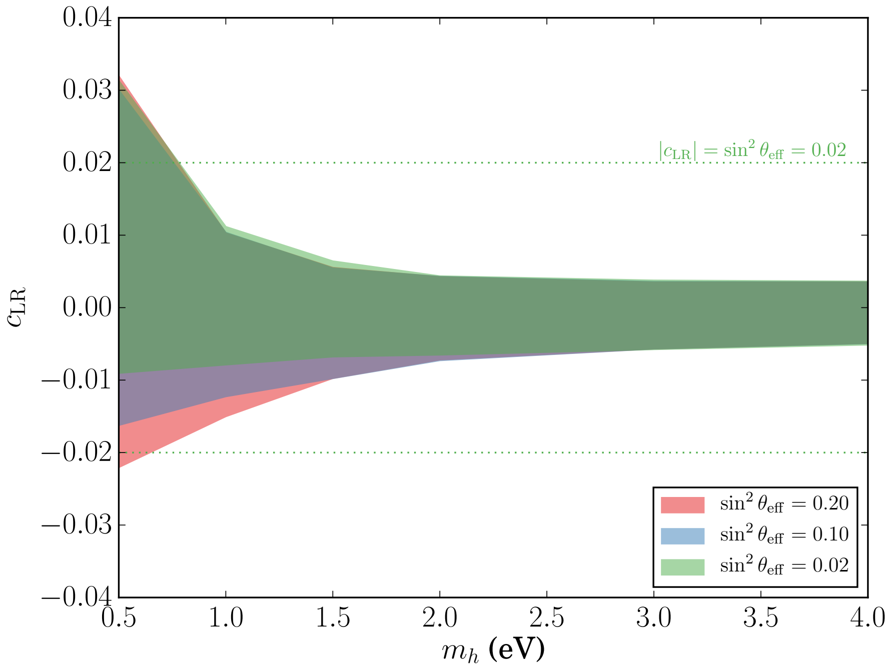

Figure 5.7: Bayesian credible intervals (95 % credibility level) on null hypothesis (5.13) for effective left-right interference strength $c_{LR} = 0$ as a function of fixed sterile neutrino mass m_h with different effective mixing angles $\sin^2\theta_{eff}$. The endpoint has been fixed at $E_0 = 18.575$ keV. The fixation of the endpoint causes the bias largely to disappear. Figure first published in [Ste+17b].

$$\log L'(\Theta) = \log L(\Theta) - \frac{1}{2}\frac{(\langle E_0\rangle - E_0)^2}{\Delta E_0^2}\,, \tag{5.20}$$

where $\langle E_0\rangle = 18.575$ keV is the null-hypothesis value and ΔE_0 is the one σ uncertainty on E_0.

The credible intervals are shown as function of the one σ endpoint uncertainty ΔE_0 for different sterile masses m_h in fig. 5.9. It can be seen that with decreasing endpoint uncertainty, the bias is reduced and the sensitivity increased. This is especially clear for lower sterile neutrino masses. There is however no significant effect unless the constraint exceeds 0.1 eV precision. Current Q value bounds from ^{3}H-^{3}He mass measurements with precision Penning traps [Mye+15] can be translated into a constraint of ~ 0.1 eV. Future experiments aim for a bound of ~ 30 meV [Str+14]. However, molecular effects and nuclear recoil have to be taken into account, which can possibly weaken the constraint on the endpoint [BPR15].

Sterile Neutrino Mass as Free Parameter

In the simulations presented up till now, the sterile neutrino mass has been fixed. This has been motivated by the degeneracy one runs into when c_{rh} and $\sin^2\theta_{eff}$ become small. This is a valid strategy for an exclusion, where the upper and lower limits, respectively, on these parameters can be determined as a function of the mass. However, in case a non-vanishing effective mixing angle is measured, the sterile neutrino mass either needs to be put in externally or treated as a free fit parameter in order to determine the correct credible intervals for c_{LR} and $\sin^2\theta_{eff}$. While for a model without right-handed currents, KATRIN is able to test

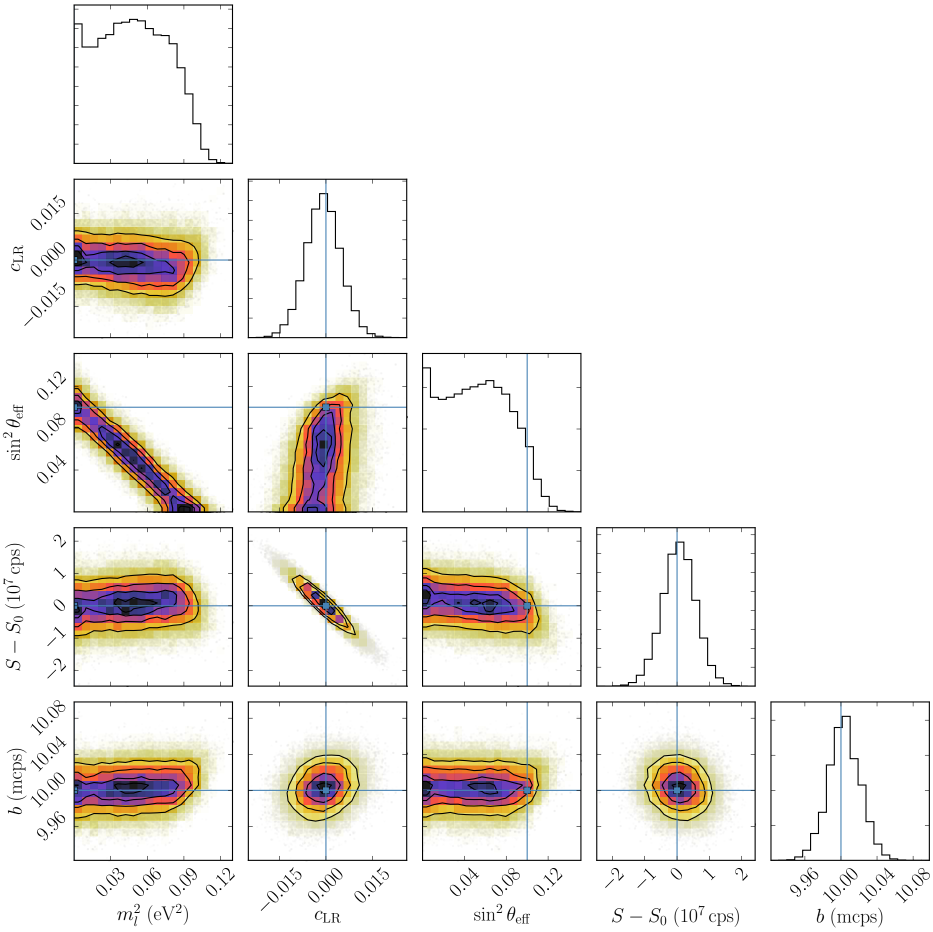

Figure 5.8: Marginalized posterior distributions for MCMC run with fixed sterile neutrino mass $m_h = 1\,\text{eV}$, effective mixing angle $\sin^2\theta_{\text{eff}} = 0.1$, left-right interference strength $c_{\text{LR}} = 0$ and a fixed endpoint $E_0 = 18.575\,\text{keV}$ for all combinations of the free fit parameters used. Contours are 0.5, 1, 1.5 and 2 σ, respectively. The blue lines show the fiducial values. The Gelman Rubin statistic R is well below 1.01 for all parameters. Figure first published in [Ste+17b].

the sterile neutrino parameter space favored by the reactor antineutrino anomaly [SH11], the additional degeneracy brought in by the free parameter c_{LR}, makes the situation more complicated. Fig. 5.10 shows the marginalized posterior distribution in the (c_{LR}, m_h^2)-space (upper panel) and the $(c_{\text{LR}}, \sin^2\theta_{\text{eff}})$-space (lower panel) for selected fiducial sterile neutrino masses. Due to the higher non-linearity of the posterior distribution, the ensemble size has been increased to $N = 10D$. Still, convergence is limited with a Gelman Rubin statistic $R < 1.01$ only for $m_h = 4\,\text{eV}$ and $R < 1.1$ for the other two examples. It can be seen that for $m_h = 1\,\text{eV}$ (left) neither the fiducial sterile neutrino mass nor the eff. mixing angle can be reasonably estimated. Most plausibly, it is not possible to extract enough information from the integral β-spectrum if the active neutrino, sterile neutrino and right-handed current signatures are all together concentrated on a region scarcely larger than the energy resolution of $\approx 1\,\text{eV}$. For $m_h = 2\,\text{eV}$ (middle), the posterior distribution is significantly sharper. However, there is still a strong, slightly non-linear, correlation which leads to a rather large uncertainty on the eff. left-right interference and eff. mixing angle. The correlation pattern shows that it is still difficult to disentangle the signatures of the active-sterile mixing and the right handed currents, yet, there is a clear relation between both. For $m_h = 4\,\text{eV}$ (right),

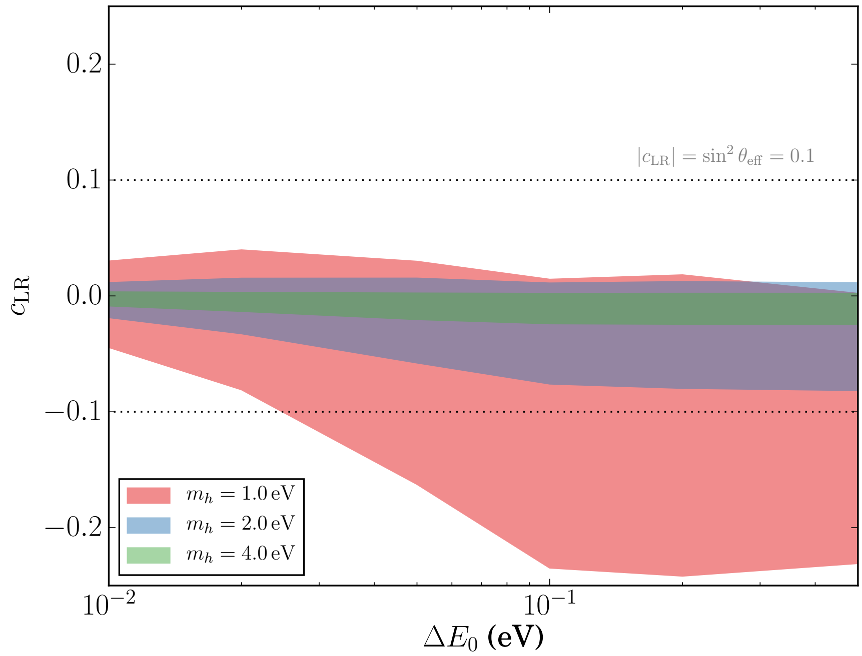

Figure 5.9: Bayesian credible intervals (95 % credibility level) on null hypothesis (5.13) for effective left-right interference strength $c_{\mathrm{LR}} = 0$ and eff. mixing angle $\sin^2\theta_{\mathrm{eff}} = 0.1$ with constrained endpoint (5.20) as a function of one σ endpoint uncertainty ΔE_0 with fixed sterile neutrino masses m_h. Figure first published in [Ste+17b].

the uncertainties and correlations become smaller, allowing to define reasonable credible intervals for both the sterile neutrino and the right-handed current parameters at the same time. Still, the correlation between c_{LR} and $\sin^2\theta_{\mathrm{eff}}$ shows that for allowing c_{LR} to be a free parameter, one loses precision on estimating the mixing angle.

5.3 Discussion

It has been shown that KATRIN is sensitive to right-handed currents in combination with light sterile neutrinos. Without constrained endpoint, the average statistical sensitivity varies from about 0.5 to 0.05 in terms of c_{LR}, depending on the sterile neutrino mass, plus a significant estimation bias. With a constrained endpoint, the sensitivity improves by up to an order of magnitude, depending on the prior uncertainty on the endpoint.

For a non-LRSM scenario of right-handed currents in absence of any sterile neutrino, it has been shown in [SHW11] that KATRIN is unlikely to improve the limit, especially because of the correlation between endpoint and interference parameter. In the scenario with additional light sterile neutrinos, which has been investigated in the present work, KATRIN performs significantly better. If LRSM is assumed as underlying model, giving rise both to sterile neutrinos and right-handed currents, the hard mathematical boundary $|c_{\mathrm{LR}}| < \sin^2\theta_{\mathrm{eff}}$ has to be kept in mind. The chances to significantly go below this hard limit rise with increasing mixing angle, increasing sterile neutrino mass and most importantly more stringent bounds on the endpoint. Additionally, it has been shown that, given a fit model with right-handed currents, the possibility of reasonably estimating the sterile neutrino mass and mixing angle is only given for higher masses $m_h \gtrsim 2\,\mathrm{eV}$. That certainly is in conflict with the parameter space favored by the reactor neutrino anomaly [Ath+98;

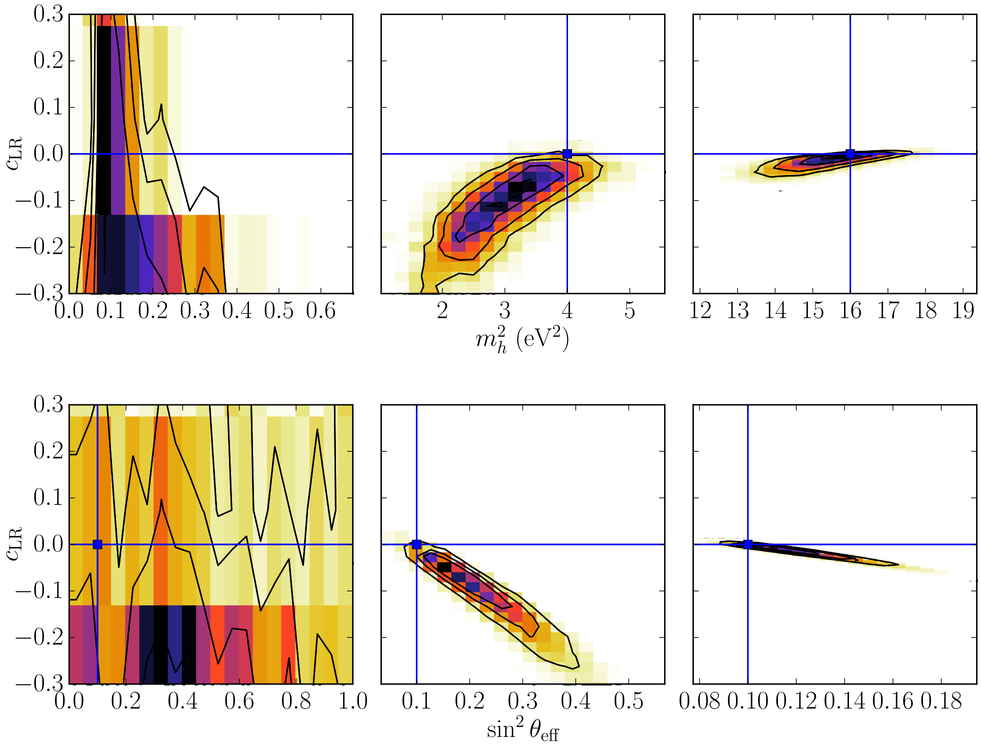

Figure 5.10: Selected marginalized posterior distributions for MCMC run with free sterile neutrino mass parameter and free endpoint, using fiducial values $m_h = 1\,\mathrm{eV}$ (left), 2 eV (middle), 4 eV (right) and $\sin^2\theta_{\mathrm{eff}} = 0.1$ (all). Contours are 0.5, 1, 1.5 and 2 σ, respectively. Upper panel: effective left-right interference strength vs. squared sterile neutrino mass m_h^2; lower panel: effective left-right interference strength vs. effective mixing angle. The blue lines show the fiducial values. Clearly, the fiducial mass and effective mixing angle fail to be estimated for smaller sterile neutrino masses $m_h \lesssim 2\,\mathrm{eV}$. Only the chains in the case of $m_h^2 = 4\,\mathrm{eV}$ are well converged with a Gelman Rubin statistic of $R < 1.01$. Figure first published in [Ste+17b].

Agu+07]. However, this parameter region has recently been excluded by IceCube [Aar+16], which nevertheless still allows higher masses $m_h \gtrsim 1.5\,\mathrm{eV}$ with at least $\sin^2\theta \lesssim 0.1$ (fig. 5.11).

Regarding the current experimental limits on a left-right symmetric c_{LR}, the current LHC bounds roughly state $m_{W_{\mathrm{R}}} \gtrsim 3\,\mathrm{TeV}$ [CMS14; ATL12] which can be translated via theoretical arguments into a bound on the LR mixing angle of about $|\xi| \lesssim 10^{-3}$ [BR13]. The maximum left-right interference (5.8) is then given for a negative ξ and vanishing *CP* violating phase, which yields the bound $c_{\mathrm{LR}} \gtrsim -0.003 \cdot \sin\theta$ for small θ. On the other side, a bound of $c_{\mathrm{LR}} \lesssim 0.001 \cdot \sin\theta$ can be derived for $m_{W_{\mathrm{R}}} \to \infty$ and $\xi > 0$ or $\cos\alpha < 0$. While the KATRIN sensitivity is not able to surpass these boundaries (fig. 5.11), it nevertheless provides a useful complementary measurement without additional cost. Moreover, these bounds are only valid for LRSM-based right-handed currents, which require a right-handed weak boson. If a Fiertz-like interference term as in (5.9) is caused by a different mechanism, there can well be a chance for KATRIN to test such models.

As shown, the sensitivity and robustness on the method depends on the ability to constrain the endpoint. A significant improvement of the sensitivity and normalization of the estimation bias is only expected if the endpoint can be constrained with a precision better than 0.1 eV (at 1σ). The most promising way of achieving this aim are ^{3}H-^{3}He mass mea-

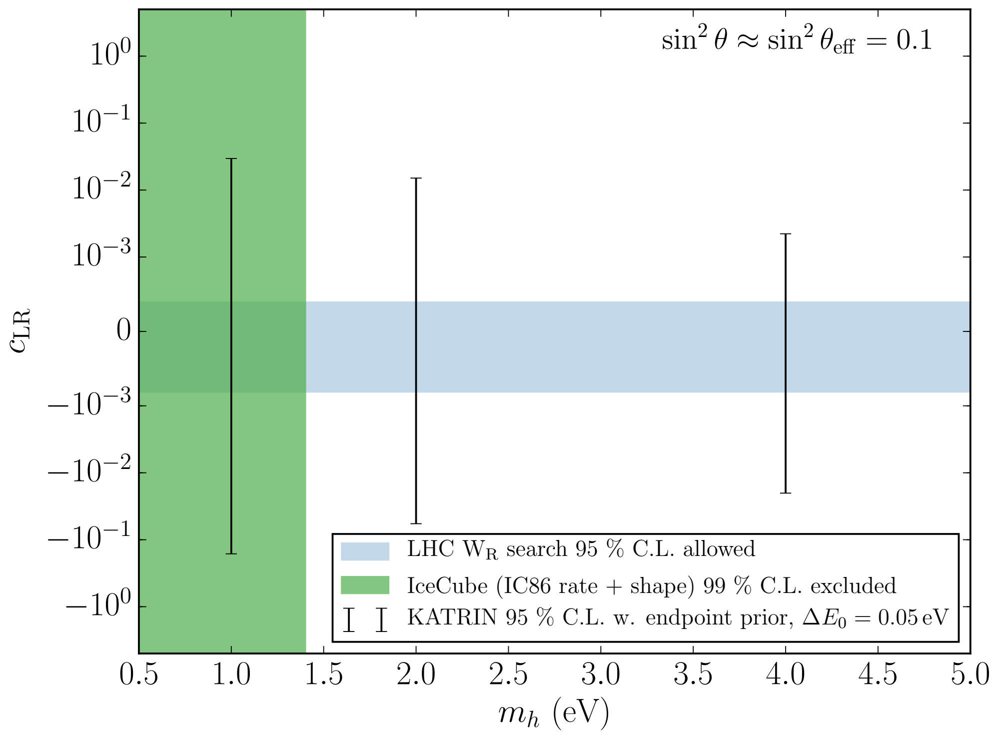

Figure 5.11: Bayesian credible intervals for configuration with endpoint prior (5.20) of $\Delta E_0 = 50\,\text{meV}$ and $\sin^2\theta\text{eff} = 0.1$ (black error bars, cf. fig. 5.9), contrasted with 99 % C.L. exclusion from IceCube [Aar+16] in the "IC86 rate+shape" analysis configuration for $\sin^2\theta = 0.1$ (green region) and limits from W_R search at the LHC [CMS14; ATL12] which state $m_{W_R} \gtrsim 3\,\text{TeV}$ at 95 % C.L., translated into bounds on c_{LR} by (5.8), assuming $|\xi| \lesssim 10^{-3}$ [BR13] for $\sin^2\theta = 0.1$ (shaded blue region). Figure first published in [Ste+17b].

surements with precision Penning traps [Mye+15; Str+14]. As future experiments aim for a bound of $\sim 30\,\text{meV}$ [Str+14], there is realistic hope to set stronger constraints on E_0 in the future. Since the endpoint is washed out by rotational-vibrational excitations of the daughter molecules, this means, regarding any future study of the systematics, that all molecular effects will need to be known sufficiently precise as well [BPR15]. Also plasma-effects in the WGTS [Kuc+17] and the high-voltage stability and calibration [Res17] as well as the work-function of the main spectrometer need to be known at that level. As KATRIN is expected to take first tritium measurements in the second half of 2017, the next milestone in the right-handed current search will be a test of the simulations on real data.

Chapter 6

Conclusion and Outlook

The Standard Model (SM) has been tremendously successful in providing a comprehensive theory of particle physics and in making concise predictions which could be confirmed experimentally, such as the Higgs boson most lately. However, certain experimental discoveries and various unsolved problems point at the *incompleteness* of the Standard Model. The confirmation of neutrino oscillation contradicts the SM assumption of massless neutrinos. The present information about dark matter especially from the anisotropy of the CMB [Ade+16] and the Bullet Cluster [Clo+06] are impossible to be explained by pure SM matter. Besides these two most prominent examples, there is a plethora of issues, such as inflation and dark energy, where the SM provides no explanation, in conjunction with conceptual problems, such as the strong CP problem and the hierarchy problem.

It is disputable if the confirmation of neutrino oscillation is a direct falsification of the SM. Historically, the zero-neutrino mass hypothesis has been rather an *ad hoc* assumption due to the non-observance of the neutrino mass. A modification of the SM with massive neutrinos does not touch its conceptual essence. Yet, without additional assumptions such as right-handed neutrinos, only pure Dirac-masses are possible for neutrinos, which is unsatisfying due to their smallness. Despite these evidences for new physics, the Standard Model remains the effective theory of particle physics as a low-energy approximation of a new fundamental theory yet to find. The incompleteness of the SM, therefore, can arguably be counted as an example of the continuity of the structural content during theory change as claimed by proponents of an epistemic structural realism [Wor89].

Despite great efforts as for instance the hunt for supersymmetry at the LHC, the search for a fundamental theory beyond the Standard Model has not been successful yet. Until there is evidence for a particular model, all experimental options to search for new phenomena or to set limits on these have to be to be followed. In this thesis, some of the options to increase the sensitivity of the KATRIN experiment to the absolute neutrino mass scale and to extend it to phenomena beyond the Standard Model in the neutrino sector, have been discussed. The prospects can be significantly enhanced if new approaches, such as the time-of-flight (TOF) mode introduced in chapter 3, are explored and utilized.

Extending the Neutrino Mass Sensitivity by TOF Spectroscopy

The implementation of TOF spectroscopy to measure the neutrino mass has strong potential in so far that it is able to increase the statistical sensitivity on the squared neutrino mass by a factor of ~ 5 for an ideal measurement. That would correspond purely statistically to a factor ~ 2.2 regarding the absolute neutrino mass scale, which would push the KATRIN limit closer to the transition region between the quasi-degenerate and hierarchical mass scale. In addition, such an approach is expected to decrease the systematic uncertainty as well, since a lower number of retarding potentials for the measurement is necessary, which can be set closer to the endpoint.

The power of the TOF method depends on the success of finding a sufficiently sensitive measurement method. The most sensitive strategy would be the detection of passing electrons with minimal interference (electron tagging). Conceivable ideas for an implementation would be based, e.g., on the interaction with the electrons inside a HF microwave cavity or the detection of the electron cyclotron emission inside the magnetic field. However, there has been no breakthrough yet. A possibility based on the existing hardware would be the periodic blocking of the electron beam by pulsing the pre-spectrometer potential (gated filtering). However, without further adjustments, there is no statistical gain.

It is therefore recommended to pursue the development of a sensitive TOF measurement method. Both the research of electron tagging and the exploration of alternative methods are viable strategies. In case of a positive outcome it is essential to study the full impact on the systematic uncertainty, which is likely to be improved as well.

Search for keV Scale Sterile Neutrinos with TOF Spectroscopy

Sterile neutrinos with masses of a few keV are suitable candidates for dark matter. Current constraints arise only from astrophysical and cosmological data and need to be complemented by laboratory searches for keV scale sterile neutrinos. Only β-decay experiments like KATRIN are currently capable of this, providing the unique opportunity of contribution to dark matter physics.

Also the search for keV scale sterile neutrinos can profit from a TOF mode. It has been shown that via TOF spectroscopy the statistical uncertainty on $\sin^2\theta$ can be pushed in the ideal case by nearly half an order of magnitude down to $\sim 5\times10^{-9}$. If an exemplary systematic uncertainty in the form of an unknown source column density is considered, the combined uncertainty amounts to over an order of magnitude less than that of the integral mode.

In comparison to the active neutrino mass measurement, the search for a sufficiently sensitive TOF measurement method is an even stronger challenge, since, due to the high count-rate, electron tagging is most likely not a viable option. The gated filter mode seams feasible from a technical point of view only for a sterile neutrino mass of a few keV and constitutes no overall improvement due to the loss of count-rate. However, it can have some benefits for a small scale measurement prior to the main neutrino mass runs of KATRIN, if the detector readout is slightly modified, since the count rate needs to be reduced for the FPD. In the long-term, a dedicated differential detector [Mer+15a] is a promising strategy, which could possibly be complemented by a TOF measurement.

Search for Right-handed Currents with eV Scale Sterile Neutrinos

Certain non-standard neutrino interactions, such as right-handed currents, can have a signature in the tritium β-spectrum. The scenario of right-handed currents in conjunction with sterile neutrinos on the eV mass scale has been investigated, which is particularly motivated by the left-right symmetric model (LRSM). It has been shown that KATRIN is able to set limits on the left-right interference strength. The sensitivity is significantly increased if the endpoint can be sufficiently constrained by mass difference measurements in Penning traps. For the case of LRSM-based right-handed currents, KATRIN can not improve the current limits from right-handed boson searches at the LHC, but complement these measurements. However, since the signature is not model-dependent, other mechanisms giving rise to right-handed currents are not excluded. The next milestone will be to perform the analysis with early data from the KATRIN tritium runs which are expected to start in late 2017/early 2018.

Appendix A

Proof: Unchanged χ^2 Properties with SCIS

In the following, it is shown that the properties of the χ^2 function defining the sensitivity, which are position and width of the minimum with respect to any parameter of interest, are independent of the choice of the background model Φ'_B. This works as well for a Poissonian log-likelihood, but for brevity it is shown on a χ^2 example. First, we define the SCIS prediction for the i-th bin,

$$\lambda'_i = \lambda_{S_i} + \lambda'_{B_i} = n\,(c_S \Phi_{S_i} + c_B \Phi'_{B_i})\,, \tag{A.1}$$

using the definition of the SCIS model (4.12), and assume that the background prediction λ'_{B_i} is independent of the parameter of interest μ,

$$\frac{\mathrm{d}}{\mathrm{d}\mu}\lambda'_{B_i} = 0\,. \tag{A.2}$$

For the proof we differentiate χ^2 with respect to μ and demand that the result is approximately independent of the choice of the background model Φ'_B:

$$\chi^2(\mu) = \sum_i \frac{(n_i - \lambda'_i(\mu))^2}{\lambda'_i(\mu)} \tag{A.3}$$

$$\begin{aligned}
\frac{\mathrm{d}}{\mathrm{d}\mu}\chi^2 &= \sum_i \frac{\lambda'_i \frac{\mathrm{d}}{\mathrm{d}\mu}(n_i - \lambda'_i)^2 - (n_i - \lambda'_i)^2 \frac{\mathrm{d}}{\mathrm{d}\mu}\lambda'_i}{\lambda'^2_i} \\
&= \sum_i \frac{-2\lambda'_i(n - \lambda'_i)\frac{\mathrm{d}}{\mathrm{d}\mu}\lambda_{S_i} - (n - \lambda'_i)^2 \frac{\mathrm{d}}{\mathrm{d}\mu}\lambda_{S_i}}{\lambda'^2_i} \\
&= -\sum_i \frac{(n_i^2 - \lambda'^2_i)\frac{\mathrm{d}}{\mathrm{d}\mu}\lambda_{S_i}}{\lambda'^2_i} \\
&= \sum_i \left(1 - \frac{n_i^2}{\lambda'^2_i}\right)\frac{\mathrm{d}}{\mathrm{d}\mu}\lambda_{S_i} \\
&= \sum_i \left(1 - \frac{n_i^2}{(\lambda'_{B_i} + \lambda_{S_i})^2}\right)\frac{\mathrm{d}}{\mathrm{d}\mu}\lambda_{S_i} \\
&= \sum_i \left(1 - \left(\frac{\lambda'_{B_i}}{n_i} + \frac{\lambda_{S_i}}{n_i}\right)^{-2}\right)\frac{\mathrm{d}}{\mathrm{d}\mu}\lambda_{S_i}
\end{aligned} \tag{A.4}$$

The variable n_i is Poisson distributed with mean $\lambda'_i(\mu_0) = \lambda_{S_i}(\mu_0) + \lambda'_{B_i}$, where μ_0 is the null-hypothesis for μ. Due to self-consistency, $\frac{\lambda'_{B_i}}{n_i}$ is approximately independent from the choice of Φ'_B, as long as the order of magnitude is in agreement $\Phi'_B \sim \Phi_B$. The latter condition ensures that the Poissonian uncertainty of n_i, which is given by $\sqrt{\lambda'_i(\mu_0)}$, is approximately conserved. $\square$

Note that the proof is only correct in the simplified case of one parameter of interest and no correlation with nuisance parameters. However, the simulation results from section 4.3.3 show that there is valid reason to expect the method to work also for more complex problems as long as there are no heavy parameter correlations.

Bibliography

[Aar+16] M. G. Aartsen et al., IceCube Collaboration. "Searches for Sterile Neutrinos with the IceCube Detector". *Phys. Rev. Lett.* 117 (2016), p. 071801. DOI: 10.1103/PhysRevLett.117.071801.

[Aba+] K. N. Abazajian et al. "Light Sterile Neutrinos: A White Paper" (). arXiv: 1204.5379.

[Abd+02] J. N. Abdurashitov et al., SAGE Collaboration. "Solar neutrino flux measurements by the Soviet-American gallium experiment (SAGE) for half the 22-year solar cycle". *J. Exp. Theor. Phys.* 95 (2002), pp. 181–193. DOI: 10.1134/1.1506424. arXiv: 0204245 [astro-ph].

[Abd+06] J. N. Abdurashitov et al., SAGE Collaboration. "Measurement of the response of a Ga solar neutrino experiment to neutrinos from a ^{37}Ar source". *Phys. Rev. C* 73 (2006), p. 45805. DOI: 10.1103/PhysRevC.73.045805.

[Abd+09] J. N. Abdurashitov et al., SAGE Collaboration. "Measurement of the solar neutrino capture rate with gallium metal. III. Results for the 2002-2007 data-taking period". *Phys. Rev. C* 80 (2009), p. 015807. DOI: 10.1103/PhysRevC.80.015807. arXiv: 0901.2200.

[Abe+11] K. Abe et al., T2K Collaboration. "The T2K experiment". *Nucl. Instr. Meth. Phys. Res. A* 659 (2011), pp. 106–135. DOI: 10.1016/j.nima.2011.06.067. arXiv: 1106.1238 [physics.ins-det].

[Abe+16] K. Abe et al., Hyper-Kamiokande proto-collaboration. *Physics Potentials with the Second Hyper-Kamiokande Detector in Korea.* Preprint. 2016. arXiv: 1611.06118v1 [hep-ex].

[Abr+91] P. Abreu et al., DELPHI Collaboration. "Determination of Z0 resonance parameters and couplings from its hadronic and leptonic decays". *Nucl. Phys. B* 367 (1991), pp. 511–574. DOI: 10.1016/0550-3213(91)90007-K.

[ABS05] T. Asaka, S. Blanchet, and M. Shaposhnikov. "The νMSM, dark matter and neutrino masses". *Phys. Lett. B* 631 (2005), pp. 151–156. DOI: 10.1016/j.physletb.2005.09.070. arXiv: 0503065 [hep-ph].

[Ada+11] P. Adamson et al., MINOS Collaboration. "First Direct Observation of Muon Antineutrino Disappearance". *Phys. Rev. Lett.* 107 (2011), p. 021801. DOI: 10.1103/PhysRevLett.107.021801. arXiv: 1104.0344.

[Ade+16] P. Ade et al., Planck Collaboration. "Planck 2015 results - cosmological parameters". *Astron. Astrophys.* 594 (2016), p. 63. DOI: 10.1051/0004-6361/201525830.

[Ago+17] M. Agostini et al., GERDA Collaboration. "Background-free search for neutrinoless double-β-decay of ^{76}Ge with GERDA". *Nature* 544 (2017), pp. 47–52. DOI: 10.1038/nature21717.

[Agu+07] A. A. Aguilar-Arevalo et al., MiniBooNE Collaboration. "Search for electron neutrino appearance at the $\Delta m^2 \sim 1\,\text{eV}^2$ scale." *Phys. Rev. Lett.* 98 (2007), p. 231801. DOI: 10.1103/PhysRevLett.98.231801. arXiv: 0704.1500.

[Ahm+01] Q. Ahmad et al., SNO Collaboration. "Measurement of the Rate of $\nu_e + d \to p + p + e$-Interactions Produced by ^8B Solar Neutrinos at the Sudbury Neutrino Observatory". *Physical Review Letters* 87 (2001). DOI: 10.1103/physrevlett.87.071301.

[Ale+16] I. Alekseev et al., DANSS Collaboration. "DANSS: Detector of the reactor AntiNeutrino based on Solid Scintillator". *J. Instr.* 11 (2016), p. 11011. DOI: 10.1088/1748-0221/11/11/P11011. arXiv: 1606.02896.

[Alt+05] M. Altmann et al., GNO Collaboration. "Complete results for five years of GNO solar neutrino observations". *Phys. Lett. B* 616 (2005), pp. 174–190. DOI: 10.1016/j.physletb.2005.04.068.

[Ams+15] J. Amsbaugh et al. "Focal-plane detector system for the KATRIN experiment". *Nucl. Instr. Meth. Phys. Res. A* 778 (2015), pp. 40–60. DOI: 10.1016/j.nima.2014.12.116. arXiv: arXiv:1404.2925v1.

[An+12] F. P. An et al., Daya Bay Collaboration. "Observation of electron-antineutrino disappearance at Daya Bay". *Phys. Rev. Lett.* 108 (2012), pp. 1–7. DOI: 10.1103/PhysRevLett.108.171803. arXiv: 1203.1669.

[Ans+95] P. Anselmann et al., GALLEX Collaboration. "GALLEX solar neutrino observations: complete results for GALLEX II". *Phys. Lett. B* 357 (1995), pp. 237–247. DOI: 10.1016/0370-2693(95)00897-T.

[Arc+15] M. Archidiacono, S. Hannestad, R. S. Hansen, and T. Tram. "Cosmology with self-interacting sterile neutrinos and dark matter: A pseudoscalar model". *Phys. Rev. D* 91 (2015), p. 065021. DOI: 10.1103/PhysRevD.91.065021.

[Arc+16] M. Archidiacono et al. "Pseudoscalar—sterile neutrino interactions: reconciling the cosmos with neutrino oscillations". *J. Cosmol. Astropart. Phys.* 2016 (2016), p. 067. DOI: 10.1088/1475-7516/2016/08/067.

[Are+16] M. Arenz et al., KATRIN Collaboration. "Commissioning of the vacuum system of the KATRIN Main Spectrometer". *Journal of Instrumentation* 11 (2016), P04011–P04011. DOI: 10.1088/1748-0221/11/04/p04011.

[AS05] T. Asaka and M. Shaposhnikov. "The νMSM, dark matter and baryon asymmetry of the universe". *Phys. Lett. B* 620 (2005), pp. 17–26. DOI: http://dx.doi.org/10.1016/j.physletb.2005.06.020.

[Ase+00] V. N. Aseev et al. "Energy loss of 18 keV electrons in gaseous T_2 and quench condensed D_2 films". *Eur. Phys. J. D* 10 (2000), pp. 39–52. DOI: 10.1007/s100530050525.

[Ase+11] V. N. Aseev et al. "Upper limit on the electron antineutrino mass from the Troitsk experiment". *Physical Review D* 84 (2011). DOI: 10.1103/physrevd.84.112003.

[Asn+15] D. M. Asner et al. "Single-Electron Detection and Spectroscopy via Relativistic Cyclotron Radiation". *Phys. Rev. Lett.* 114 (2015), p. 162501. DOI: 10.1103/PhysRevLett.114.162501. arXiv: 1408.5362.

[Ath+98] C. Athanassopoulos et al., LSND Collaboration. “Results on $\nu_\mu \rightarrow \nu_e$ Neutrino Oscillations from the LSND Experiment”. *Phys. Rev. Lett.* 81 (1998), pp. 1774–1777. DOI: 10.1103/PhysRevLett.81.1774. arXiv: 9709006 [nucl-ex].

[ATL12] ATLAS Collaboration. “Search for heavy neutrinos and right-handed W bosons in events with two leptons and jets in pp collisions at $\sqrt{s}$ = 7 TeV with the ATLAS detector”. *Eur. Phys. J. C* 72 (2012), p. 2056. DOI: 10.1140/epjc/s10052-012-2056-4.

[Ayr+05] D. Ayres et al., NOvA Collaboration. *NOvA Proposal to Build a 30 Kiloton Off-Axis Detector to Study Neutrino Oscillations in the Fermilab NuMI Beamline.* Proposal 0929. Fermilab, 2005. arXiv: hep-ex/0503053v1 [hep-ex].

[Bab+12] M. Babutzka et al. “Monitoring of the operating parameters of the KATRIN Windowless Gaseous TRItium Source”. *New J. Phys.* 14 (2012), p. 103046. DOI: 10.1088/1367-2630/14/10/103046. arXiv: arXiv:1205.5421v3.

[Bau+13] S. Bauer et al. “Next generation KATRIN high precision voltage divider for voltages up to 65kV”. *J. Instrum.* 8 (2013), P10026–P10026. DOI: 10.1088/1748-0221/8/10/P10026. arXiv: 1309.4955v1.

[BBK11] M. Boylan-Kolchin, J. S. Bullock, and M. Kaplinghat. “Too big to fail? The puzzling darkness of massive Milky Way subhaloes”. *Mon. Not. R. Astron. Soc. Lett.* 415 (2011), pp. L40–L44. DOI: 10.1111/j.1745-3933.2011.01074.x. arXiv: 1103.0007.

[Bec+10] M. Beck et al. “Effect of a sweeping conductive wire on electrons stored in a Penning-like trap between the KATRIN spectrometers”. *Eur. Phys. J. A* 44 (2010), pp. 499–511. DOI: 10.1140/epja/i2010-10959-1. arXiv: 0909.3337.

[Bec+14] M. Beck et al. “An angular-selective electron source for the KATRIN experiment”. *J. Instrum.* 9 (2014), P11020–P11020. DOI: 10.1088/1748-0221/9/11/P11020.

[Beh+17] J. Behrens et al. “A pulsed, mono-energetic and angular-selective UV photo-electron source for the commissioning of the KATRIN experiment” (2017). Submitted to EPJ C, pp. 1–19. arXiv: 1703.05272.

[Beh16] J. Behrens. “Design and commissioning of a mono-energetic photoelectron source and active background reduction by magnetic pulse at the KATRIN spectrometers”. PhD Thesis. Westfälische Wilhelms Universität Münster, 2016.

[Bel+13] A. I. Belesev et al. “Upper limit on additional neutrino mass eigenstate in 2 to 100 eV region from "Troitsk nu-Mass” data”. *JETP Lett.* 97 (2013), pp. 67–69. DOI: 10.1134/S0021364013020033.

[BGP02] J. N. Bahcall, C. M. Gonzalez-Garcia, and C. Pena-Garay. “Before and After: How has the SNO NC measurement changed things?” *J. High Energy Phys.* 2002 (2002), pp. 054–054. DOI: 10.1088/1126-6708/2002/07/054. arXiv: 0204314 [hep-ph].

[BHL10] F. Bezrukov, H. Hettmansperger, and M. Lindner. “KeV sterile neutrino dark matter in gauge extensions of the standard model”. *Phys. Rev. D* 81 (2010), pp. 1–13. DOI: 10.1103/PhysRevD.81.085032. arXiv: 0912.4415.

[BHR14] J. Barry, J. Heeck, and W. Rodejohann. “Sterile neutrinos and right-handed currents in KATRIN”. *J. High Energy Phys.* 2014 (2014). DOI: 10.1007/JHEP07(2014)081. arXiv: 1404.5955.

[Bok13] K. Bokeloh. “Calibration of hot and cold dark matter experiments: An angular-selective photoelectron source for the KATRIN experiment and an apparatus to determine the reflection properties of PTFE for vacuum UV light”. PhD Thesis. University of Münster, 2013.

[Bon+11] J. Bonn et al. “The KATRIN sensitivity to the neutrino mass and to right-handed currents in beta decay”. *Phys. Lett. B* 703 (2011), pp. 310–312. DOI: 10.1016/j.physletb.2011.08.005.

[Bon+99] J. Bonn, L. Bornschein, B. Degen, E. W. Otten, and C. Weinheimer. “A high resolution electrostatic time-of-flight spectrometer with adiabatic magnetic collimation”. *Nucl. Instr. Meth. Phys. Res. A* 421 (1999), pp. 256–265. DOI: 10.1016/S0168-9002(98)01263-7.

[Bor16] D. Borah. “Light Sterile Neutrino and Dark Matter in Left-Right Symmetric Models Without Higgs Bidoublet”. 075024 (2016), pp. 1–13. DOI: 10.1103/PhysRevD.94.075024. arXiv: 1607.00244.

[Boy+06] A. Boyarsky, A. Neronov, O. Ruchayskiy, and M. Shaposhnikov. “Constraints on sterile neutrinos as dark matter candidates from the diffuse X-ray background”. *Mon. Not. R. Astron. Soc.* 370 (2006), pp. 213–218. DOI: 10.1111/j.1365-2966.2006.10458.x. arXiv: 0512509 [astro-ph].

[Boy+14] A. Boyarsky, O. Ruchayskiy, D. Iakubovskyi, and J. Franse. “Unidentified line in X-ray spectra of the andromeda galaxy and perseus galaxy cluster”. *Phys. Rev. Lett.* 113 (2014). DOI: 10.1103/PhysRevLett.113.251301. arXiv: 1402.4119.

[Boy14] L. Boyle. 2014. URL: https://commons.wikimedia.org/wiki/File:Standard_Model_Of_Particle_Physics--Most_Complete_Diagram.png (visited on 02/12/2017).

[BPR15] L. I. Bodine, D. S. Parno, and R. G. H. Robertson. “Assessment of molecular effects on neutrino mass measurements from tritium β-decay”. *Phys. Rev. C* 91 (2015), p. 035505. DOI: 10.1103/PhysRevC.91.035505. arXiv: 1502.03497.

[BR13] J. Barry and W. Rodejohann. “Lepton number and flavour violation in TeV-scale left-right symmetric theories with large left-right mixing”. *J. High Energy Phys.* 2013 (2013), p. 153. DOI: 10.1007/JHEP09(2013)153. arXiv: 1303.6324.

[Bra+16] D. Bravo-Berguno et al., SOX Collaboration. “SOX : Short Distance Neutrino Oscillations with Borexino”. *Nucl. Part. Phys. Proc.* 273-275 (2016), pp. 1760–1764. DOI: 10.1016/j.nuclphysbps.2015.09.283.

[BRZ11] J. Barry, W. Rodejohann, and H. Zhang. “Light sterile neutrinos: models and phenomenology”. *J. High Energy Phys.* 2011 (2011), p. 91. DOI: 10.1007/JHEP07(2011)091. arXiv: 1105.3911.

[BSB05] J. N. Bahcall, A. M. Serenelli, and S. Basu. “New Solar Opacities, Abundances, Helioseismology, and Neutrino Fluxes”. *Astrophys. J.* 621 (2005), pp. L85–L88. DOI: 10.1086/428929.

[Bul+14] E. Bulbul et al. “Detection of an Unidentified Emission Line in the Stacked X-Ray Spectrum of Galaxy Clusters”. *Astrophys. J.* 789 (2014), p. 13. DOI: 10.1088/0004-637X/789/1/13. arXiv: 1402.2301.

[BY98] M. Bando and K. Yoshioka. “Sterile Neutrinos in a Grand Unified Model”. *Prog. Theor. Phys.* 100 (1998), pp. 1239–1250. DOI: 10.1143/ptp.100.1239.

[Cle+98] B. T. Cleveland et al. "Measurement of the Solar Electron Neutrino Flux with the Homestake Chlorine Detector". *Astrophys. J.* 496 (1998), pp. 505–526. DOI: 10.1086/305343.

[Clo+06] D. Clowe et al. "A Direct Empirical Proof of the Existence of Dark Matter". *Astrophys. J.* 648 (2006), pp. L109–L113. DOI: 10.1086/508162.

[CMS12] CMS Collaboration. "A new boson with a mass of 125 GeV observed with the CMS experiment at the Large Hadron Collider." *Science* 338 (2012), pp. 1569–75. DOI: 10.1126/science.1230816.

[CMS14] CMS Collaboration. "Search for heavy neutrinos and W bosons with right-handed couplings in proton-proton collisions at $\sqrt{s} = 8$ TeV". *Eur. Phys. J. C* 74 (2014), p. 3149. DOI: 10.1140/epjc/s10052-014-3149-z. arXiv: 1407.3683.

[Coo+14] R. J. Cooke et al. "Precision measurements of the primal abundance of deuterium." *Astrophys. J.* 781 (2014), p. 31. DOI: 10.1088/0004-637X/781/1/31.

[Cow+56] C. L. Cowan, F. Reines, F. B. Harris, H. W. Kruse, and A. D. McGu. "Detection of the Free Neutrino: a Confirmation". *Science* 124 (1956), pp. 103–104. DOI: 10.1126/science.124.3212.103.

[Cow98] G. Cowan. *Statistical Data Analysis.* Oxford: Oxford University Press, 1998. ISBN: 978-0198501558.

[Cyb+16] R. H. Cyburt, B. D. Fields, K. A. Olive, and T.-H. Yeh. "Big bang nucleosynthesis: Present status". *Rev. Mod. Phys.* 88 (2016), p. 015004. DOI: 10.1103/RevModPhys.88.015004.

[Dan+62] G. Danby et al. "Observation of High-Energy Neutrino Reactions and the Existence of Two Kinds of Neutrinos". *Phys. Rev. Lett.* 9 (1962), pp. 36–44. DOI: 10.1103/physrevlett.9.36.

[DBM12] M. K. Das, D. Borah, and R. Mishra. "Quasidegenerate neutrinos in type II seesaw models". *Phys. Rev. D* 86 (2012), p. 095006. DOI: 10.1103/PhysRevD.86.095006. arXiv: 1209.0280.

[DDS13] C. Destri, H. J. De Vega, and N. G. Sanchez. "Warm dark matter primordial spectra and the onset of structure formation at redshift z". *Phys. Rev. D* 88 (2013). DOI: 10.1103/PhysRevD.88.083512. arXiv: 1308.1109.

[DI02] S. Davidson and A. Ibarra. "A lower bound on the right-handed neutrino mass from leptogenesis". *Phys. Lett. B* 535 (2002), pp. 25–32. DOI: http://dx.doi.org/10.1016/S0370-2693(02)01735-5.

[Dos+06] N. Doss, J. Tennyson, A. Saenz, and S. Jonsell. "Molecular effects in investigations of tritium molecule β-decay endpoint experiments". *Phys. Rev. C* 73 (2006). DOI: 10.1103/PhysRevC.73.025502.

[Dre+13] G. Drexlin, V. Hannen, S. Mertens, and C. Weinheimer. "Current direct neutrino mass experiments". *Adv. High Energy Phys.* 2013 (2013). DOI: 10.1155/2013/293986. arXiv: 1307.0101.

[Dre+17] M. Drewes, T. Lasserre, A. Merle, and S. Mertens, Editors. "A White Paper on keV Sterile Neutrino Dark Matter". *JCAP* 1701 (2017), p. 025. DOI: 10.1088/1475-7516/2017/01/025. arXiv: 1602.04816.

[DT08] N. Doss and J. Tennyson. "Excitations to the electronic continuum of $^3HeT^+$ in investigations of T_2 β-decay experiments". *J. Phys. B* 41 (2008), p. 125701. DOI: 10.1088/0953-4075/41/12/125701.

[DVS13] C. Destri, H. J. de Vega, and N. G. Sanchez. “Quantum WDM fermions and gravitation determine the observed galaxy structures”. *Astropart. Phys.* 46 (2013), pp. 14–22. DOI: 10.1016/j.astropartphys.2013.04.004.

[DW94] S. Dodelson and L. M. Widrow. “Sterile neutrinos as dark matter”. *Phys. Rev. Lett.* 72 (1994), pp. 17–20. DOI: 10.1103/PhysRevLett.72.17.

[Egu+03] K. Eguchi et al., KamLAND Collaboration. “First Results from KamLAND: Evidence for Reactor Antineutrino Disappearance”. *Phys. Rev. Lett.* 90 (2003), p. 021802. DOI: 10.1103/PhysRevLett.90.021802. arXiv: 0212021 [hep-ex].

[Eli+15] S. Eliseev et al. “Direct Measurement of the Mass Difference of Ho^{163} and Dy^{163} Solves the Q-Value Puzzle for the Neutrino Mass Determination”. *Phys. Rev. Lett.* 115 (2015). DOI: 10.1103/physrevlett.115.062501.

[Eno] S. Enomoto. To be published.

[EP12] A. Esmaili and O. L. G. Peres. “KATRIN sensitivity to sterile neutrino mass in the shadow of lightest neutrino mass”. *Phys. Rev. D* 85 (2012), pp. 1–5. DOI: 10.1103/PhysRevD.85.117301. arXiv: 1203.2632.

[Erh+14] M. Erhard et al. “High-voltage monitoring with a solenoid retarding spectrometer at the KATRIN experiment”. *J. Instr.* 9 (2014), p. 06022. DOI: 10.1088/1748-0221/9/06/p06022.

[Erl] Erlangen Center for Astroparticle Physics. URL: http://www.ecap.physik.uni-erlangen.de/nexo/research.shtml (visited on 02/17/2017).

[EV02] S. R. Elliott and P. Vogel. “Double Beta Decay”. *Ann. Rev. Nucl. Part. Sci.* 52 (2002), pp. 115–151. DOI: 10.1146/annurev.nucl.52.050102.090641.

[FB11] J. A. Formaggio and J. Barrett. “Resolving the reactor neutrino anomaly with the KATRIN neutrino experiment”. *Phys. Lett. B* 706 (2011), pp. 68–71. DOI: 10.1016/j.physletb.2011.10.069. arXiv: 1105.1326.

[FC97] G. J. Feldman and R. D. Cousins. “A Unified Approach to the Classical Statistical Analysis of Small Signals”. *Phys. Rev. D* 57 (1997), pp. 3873–3889. DOI: 10.1103/PhysRevD.57.3873. arXiv: 9711021 [physics].

[Fix09] D. J. Fixsen. “The Temperature of the Cosmic Microwave Background”. *Astrophys. J.* 707 (2009), p. 916. DOI: 10.1088/0004-637X/707/2/916.

[FL04] G. Fogli and E. Lisi. “Evidence for the MSW effect”. *New J. Phys.* 6 (2004), pp. 139–139. DOI: 10.1088/1367-2630/6/1/139.

[Fow31] R. H. Fowler. “The Analysis of Photoelectric Sensitivity Curves for Clean Metals at Various Temperatures”. *Phys. Rev.* 38 (1931), pp. 45–56. DOI: 10.1103/PhysRev.38.45.

[Frä+14] F. M. Fränkle et al. “Penning discharge in the KATRIN pre-spectrometer”. *J. Instr.* 9 (2014), P07028–P07028. DOI: 10.1088/1748-0221/9/07/P07028.

[Fuk+98] Y. Fukuda et al., SuperKamiokande Collaboration. “Evidence for Oscillation of Atmospheric Neutrinos”. *Physical Review Letters* 81 (1998), pp. 1562–1567. DOI: 10.1103/physrevlett.81.1562.

[FY86] M. Fukugita and T. Yanagida. “Barygenesis without grand unification”. *Phys. Lett. B* 174 (1986), pp. 45–47. DOI: 10.1016/0370-2693(86)91126-3.

[GGS58] M. Goldhaber, L. Grodzins, and A. W. Sunyar. “Helicity of Neutrinos”. *Phys. Rev.* 109 (1958), pp. 1015–1017. DOI: 10.1103/physrev.109.1015.

[Gil83] D. T. Gillespie. “A theorem for physicists in the theory of random variables”. *Am. J. Phys.* 51 (1983), p. 520. DOI: 10.1119/1.13221.

[Giu13] C. Giunti. “Phenomenology of sterile neutrinos”. *J. Phys. Conf. Ser.* 408 (2013), p. 012009. DOI: 10.1088/1742-6596/408/1/012009. arXiv: 1110.3914.

[GJ08] A. de Gouvêa and J. Jenkins. “Physical range of majorana neutrino mixing parameters”. *Phys. Rev. D* 78 (2008). DOI: 10.1103/physrevd.78.053003.

[Glü] F. Glück. to be published.

[Glü+13] F. Glück et al. “Electromagnetic design of the large-volume air coil system of the KATRIN experiment”. *New J. Phys.* 15 (2013), p. 083025. DOI: 10.1088/1367-2630/15/8/083025. arXiv: 1304.6569.

[GR92] A. Gelman and D. B. Rubin. “Inference from Iterative Simulation Using Multiple Sequences”. *Stat. Sci.* 7 (1992), pp. 457–472. DOI: doi:10.1214/ss/1177011136.

[Gro15] S. Groh. “Modeling of the response function and measurement of transmission properties of the KATRIN experiment”. PhD Thesis. Karlsruhe Institute of Technology, 2015.

[Ham+99] W. Hampel et al., GALLEX Collaboration. “GALLEX solar neutrino observations: results for GALLEX IV”. *Phys. Lett. B* 447 (1999), pp. 127–133. DOI: 10.1016/S0370-2693(98)01579-2.

[Han+17] V. Hannen, I. Heese, C. Weinheimer, A. Sejersen Riis, and K. Valerius. “Deconvolution of the energy loss function of the KATRIN experiment”. *Astropart. Phys.* 89 (2017), pp. 30–38. DOI: 10.1016/j.astropartphys.2017.01.010.

[Has+16] C. Hassel et al. “Recent Results for the ECHo Experiment”. *J. Low Temp. Phys.* 184 (2016), pp. 910–921. DOI: 10.1007/s10909-016-1541-9.

[Has70] B. Hastings. “Monte Carlo sampling methods using Markov chains and their applications”. *Biometrika* 57 (1970), pp. 97–109. DOI: 10.1093/biomet/57.1.97.

[HHT14] S. Hannestad, R. S. Hansen, and T. Tram. “How Self-Interactions can Reconcile Sterile Neutrinos with Cosmology”. *Phys. Rev. Lett.* 112 (2014), p. 031802. DOI: 10.1103/PhysRevLett.112.031802.

[Hol92] E. Holzschuh. “Measurement of the neutrino mass from tritium beta -decay”. *Rep. Prog. Phys.* 55 (1992), pp. 1035–1091. DOI: 10.1088/0034-4885/55/7/004.

[HS95] P. Huet and E. Sather. “Electroweak baryogenesis and standard model CP violation”. *Phys. Rev. D* 51 (1995), pp. 379–394. DOI: 10.1103/PhysRevD.51.379.

[JR75] F. James and M. Roos. “Minuit - a system for function minimization and analysis of the parameter errors and correlations”. *Comput. Phys. Comm.* 10 (1975), pp. 343–367. DOI: 10.1016/0010-4655(75)90039-9.

[Kae+10] F. Kaether, W. Hampel, G. Heusser, J. Kiko, and T. Kirsten. “Reanalysis of the Gallex solar neutrino flux and source experiments”. *Phys. Lett. B* 685 (2010), pp. 47–54. DOI: 10.1016/j.physletb.2010.01.030.

[KAT04] KATRIN Collaboration. *KATRIN Design Report.* Scientific report 7090. FZKA, 2004.

[KK77] W. Konetschny and W. Kummer. “Nonconservation of total lepton number with scalar bosons”. *Phys. Lett. B* 70 (1977), pp. 433–435. DOI: 10.1016/0370-2693(77)90407-5.

[Kle14] M. Kleesiek. “A Data-Analysis and Sensitivity-Optimization Framework for the KATRIN Experiment”. PhD Thesis. Karlsruhe Institute of Technology, 2014.

[Kly+99] A. Klypin, A. V. Kravtsov, O. Valenzuela, and F. Prada. “Where Are the Missing Galactic Satellites?” *Astrophys. J.* 522 (1999), pp. 82–92. DOI: 10.1086/307643. arXiv: 9901240 [astro-ph].

[Kod+01] K. Kodama et al., DONUT Collaboration. “Observation of tau neutrino interactions”. *Physics Letters B* 504 (2001), pp. 218–224. DOI: 10.1016/s0370-2693(01)00307-0.

[Kra+05] C. Kraus et al. “Final Results from phase II of the Mainz Neutrino Mass Search in Tritium β Decay”. *Eur. Phys. J. C* 40 (2005), pp. 447–468. DOI: 10.1140/epjc/s2005-02139-7. arXiv: 0412056 [hep-ex].

[Kra+13] C. Kraus, A. Singer, K. Valerius, and C. Weinheimer. “Limit on sterile neutrino contribution from the Mainz Neutrino Mass Experiment”. *Eur. Phys. J. C* 73 (2013), pp. 1–8. DOI: 10.1140/epjc/s10052-013-2323-z. arXiv: 1210.4194.

[Kra16] M. Kraus. “Energy-Scale Systematics at the KATRIN Main Spectrometer”. PhD Thesis. Karlsruhe Institute of Technology, 2016.

[KRS85] V. Kuzmin, V. Rubakov, and M. Shaposhnikov. “On anomalous electroweak baryon-number non-conservation in the early universe”. *Phys. Lett. B* 155 (1985), pp. 36–42. DOI: 10.1016/0370-2693(85)91028-7.

[KTY10] A. Kusenko, F. Takahashi, and T. T. Yanagida. “Dark matter from split seesaw”. *Phys. Lett. B* 693 (2010), pp. 144–148. DOI: 10.1016/j.physletb.2010.08.031. arXiv: arXiv:1006.1731v2.

[Kuc+17] L. Kuckert et al. *to be published.* 2017.

[Las16] T. Lasserre. “Latest Double Chooz results”. *Journal of Physics: Conference Series* 718 (2016), p. 062034. DOI: 10.1088/1742-6596/718/6/062034.

[LMN11] M. Lindner, A. Merle, and V. Niro. “Soft L e − L $_\mu$ − L $_\tau$ flavour symmetry breaking and sterile neutrino keV Dark Matter”. *J. Cosmol. Astropart. Phys.* 2011 (2011), p. 034. DOI: 10.1088/1475-7516/2011/01/034. arXiv: 1011.4950.

[Lov+12] M. R. Lovell et al. “The haloes of bright satellite galaxies in a warm dark matter universe”. *Mon. Not. R. Astron. Soc.* 420 (2012), pp. 2318–2324. DOI: 10.1111/j.1365-2966.2011.20200.x. arXiv: 1104.2929.

[LP14] J. Lesgourgues and S. Pastor. “Neutrino cosmology and Planck”. *New J. Phys.* 16 (2014), p. 065002. DOI: 10.1088/1367-2630/16/6/065002. arXiv: 1404.1740.

[LS08] M. Laine and M. Shaposhnikov. “Sterile neutrino dark matter as a consequence of νMSM-induced lepton asymmetry”. *J. Cosmol. Astropart. Phys.* 2008 (2008), p. 031. DOI: 10.1088/1475-7516/2008/06/031.

[LS89] P. Langacker and S. U. Sankar. “Bounds on the mass of W_R and the W_L–W_R mixing angle ξ in general $SU(2)_L \times SU(2)_R \times U(1)$ models”. *Phys. Rev. D* 40 (1989), pp. 1569–1585. DOI: 10.1103/physrevd.40.1569.

[Luk+12] S. Lukić et al. “Measurement of the gas-flow reduction factor of the KATRIN DPS2-F differential pumping section”. *Vacuum* 86 (2012), pp. 1126–1133. DOI: 10.1016/j.vacuum.2011.10.017.

[Men+11] G. Mention et al. “Reactor antineutrino anomaly”. *Phys. Rev. D* 83 (2011). DOI: 10.1103/PhysRevD.83.073006. arXiv: 1101.2755.

[Mer+13] S. Mertens et al. "Background due to stored electrons following nuclear decays in the KATRIN spectrometers and its impact on the neutrino mass sensitivity". *Astropart. Phys.* 41 (2013), pp. 52–62. DOI: 10.1016/j.astropartphys.2012.10.005.

[Mer+15a] S. Mertens et al. "Sensitivity of next-generation tritium beta-decay experiments for keV-scale sterile neutrinos". *J. Cosmol. Astropart. Phys.* 2015 (2015), p. 020. DOI: 10.1088/1475-7516/2015/02/020.

[Mer+15b] S. Mertens et al. "Wavelet approach to search for sterile neutrinos in tritium β-decay spectra". *Phys. Rev. D* 91 (2015). DOI: 10.1103/PhysRevD.91.042005. arXiv: 1410.7684.

[MFL12] N. Menci, F. Fiore, and A. Lamastra. "Galaxy formation in warm dark matter cosmology". *Mon. Not. R. Astron. Soc.* 421 (2012), pp. 2384–2394. DOI: 10.1111/j.1365-2966.2012.20470.x. arXiv: 1201.1617.

[MN11] A. Merle and V. Niro. "Deriving models for keV sterile neutrino Dark Matter with the Froggatt-Nielsen mechanism". *J. Cosmol. Astropart. Phys.* 2011 (2011), p. 023. DOI: 10.1088/1475-7516/2011/07/023. arXiv: 1105.5136.

[MNS62] Z. Maki, M. Nakagawa, and S. Sakata. "Remarks on the Unified Model of Elementary Particles". *Prog. Theor. Phys.* 28 (1962), pp. 870–880. DOI: 10.1143/PTP.28.870.

[Moh+07] R. N. Mohapatra et al. "Theory of neutrinos: a white paper". *Rep. Prog. Phys.* 70 (2007), pp. 1757–1867. DOI: 10.1088/0034-4885/70/11/R02. arXiv: 0510213 [hep-ph].

[MP04] R. N. Mohapatra and P. B. Pal. *Massive Neutrinos in Physics and Astrophysics.* 3rd ed. World Scientific Publishing Company, 2004. ISBN: 981238071X.

[MP75] R. N. Mohapatra and J. C. Pati. ""Natural" left-right symmetry". *Physical Review D* 11 (1975), pp. 2558–2561. DOI: 10.1103/physrevd.11.2558.

[MS80] R. N. Mohapatra and G. Senjanović. "Neutrino mass and spontaneous parity nonconservation". *Phys. Rev. Lett.* 44 (1980), pp. 912–915. DOI: 10.1103/PhysRevLett.44.912.

[MS85] S. P. Mikheyev and A. Y. Smirnov. "Resonance enhancement of oscillations in matter and solar neutrino spectroscopy". *Yad. Fiz.* 42 (1985), pp. 1441–1448.

[Mur14] H. Murayama. 2014. URL: http://hitoshi.berkeley.edu/neutrino/ (visited on 02/17/2017).

[Mye+15] E. G. Myers, A. Wagner, H. Kracke, and B. A. Wesson. "Atomic Masses of Tritium and Helium-3". *Phys. Rev. Lett.* 114 (1 2015), p. 013003. DOI: 10.1103/PhysRevLett.114.013003.

[Ney37] J. Neyman. "Outline of a theory of statistical estimation based on the classical theory of probability". *Phil. Trans. R. Soc. Lond.* A237 (1937), pp. 333–380. DOI: 10.1098/rsta.1937.0005.

[NFW96] J. F. Navarro, C. S. Frenk, and S. D. M. White. "The Structure of Cold Dark Matter Halos". *Astrophys. J.* 462 (1996), p. 563. DOI: 10.1086/177173. arXiv: 9508025 [astro-ph].

[OW08] E. W. Otten and C. Weinheimer. "Neutrino mass limit from tritium β-decay". *Reports Prog. Phys.* 71 (2008), p. 086201. DOI: 10.1088/0034-4885/71/8/086201.

[Pap+15] E. Papastergis, R. Giovanelli, M. P. Haynes, and F. Shankar. "Is there a "too big to fail" problem in the field?" *Astron. Astrophys.* 574 (2015), A113. DOI: 10.1051/0004-6361/201424909. arXiv: 1407.4665.

[Pat+16] C. Patrignani et al., Particle Data Group. "Review of Particle Physics". *Chin. Phys. C* 40 (2016), p. 010001. DOI: 10.1103/PhysRevD.86.010001. arXiv: 0601168 [astro-ph].

[Pau30] W. Pauli. *Offener Brief an die Gruppe der Radioaktiven bei der Gauvereins-Tagung zu Tübingen.* Letter. 1930.

[Peq15] M. Pequignot, Nucifer and Stereo Collaborations. "The Nucifer and Stereo reactor antineutrino experiments". *Nuclear and Particle Physics Proceedings* 265-266 (2015), pp. 126–128. DOI: 10.1016/j.nuclphysbps.2015.06.032.

[Pic+92] A. Picard et al. "A solenoid retarding spectrometer with high resolution and transmission for keV electrons". *Nucl. Instr. Meth. Phys. Res. B* 63 (1992), pp. 345–358. DOI: 10.1016/0168-583X(92)95119-C.

[Pon57] B. Pontecorvo. "Mesonium and Antimesonium". *J. Exptl. Theoret. Phys. (U.S.S.R.)* 33 (1957).

[PP13] M. K. Parida and S. Patra. "Left-right models with light neutrino mass prediction and dominant neutrinoless double beta decay rate". *Phys. Lett. B* 718 (2013), pp. 1407–1412. DOI: 10.1016/j.physletb.2012.12.036. arXiv: arXiv:1211.5000v2.

[PS74] J. C. Pati and A. Salam. "Lepton number as the fourth "color"". *Phys. Rev. D* 10 (1974), pp. 275–289. DOI: 10.1103/PhysRevD.10.275.

[Pun03] G. Punzi. "Sensitivity of searches for new signals and its optimization". In: *Conf. Stat. Probl. Part. Physics, Astrophys. Cosmol.* 2003, p. 5. arXiv: 0308063 [physics]. URL: http://arxiv.org/abs/physics/0308063$%5Cbackslash$nhttp://www.slac.stanford.edu/econf/C030908/proceedings.html.

[QV15] X. Qian and P. Vogel. "Neutrino mass hierarchy". *Prog. Part. Nucl. Phys.* 83 (2015), pp. 1–30. DOI: 10.1016/j.ppnp.2015.05.002. arXiv: 1505.01891.

[Res17] O. Rest. PhD thesis, to be published. 2017.

[RK08] R. Y. Rubinstein and D. P. Kroese. *Simulation and the monte carlo method.* John Wiley & Sons, 2008. ISBN: 9780470177945.

[RK88] R. G. H. Robertson and D. A. Knapp. "Direct Measurements of Neutrino Mass". *Annual Review of Nuclear and Particle Science* 38 (1988), pp. 185–215. DOI: 10.1146/annurev.ns.38.120188.001153.

[Sak91] A. D. Sakharov. "Violation of CP invariance, C asymmetry, and baryon asymmetry of the universe". *Sov. Phys. Usp.* 34 (1991), p. 392.

[SBN06] N. Severijns, M. Beck, and O. Naviliat-Cuncic. "Tests of the standard electroweak model in nuclear beta decay". *Rev. Mod. Phys.* 78 (2006), pp. 991–1040. DOI: 10.1103/RevModPhys.78.991. arXiv: 0605029 [nucl-ex].

[Sch+12] A. Schneider, R. E. Smith, A. V. Maccio, and B. Moore. "Non-linear evolution of cosmological structures in warm dark matter models". *Mon. Not. R. Astron. Soc.* 424 (2012), pp. 684–698. DOI: 10.1111/j.1365-2966.2012.21252.x. arXiv: 1112.0330.

[Seo16] H. Seo, RENO Collaboration. “Recent result from RENO”. *Journal of Physics: Conference Series* 718 (2016), p. 062053. DOI: 10.1088/1742-6596/718/6/062053.

[SF99] X. Shi and G. M. Fuller. “New Dark Matter Candidate: Nonthermal Sterile Neutrinos”. *Phys. Rev. Lett.* 82 (1999), pp. 2832–2835. DOI: 10.1103/PhysRevLett.82.2832.

[SG98] G. J. Stephenson and T. Goldman. “A possible solution to the tritium endpoint problem”. *Phys. Lett. B* 440 (1998), pp. 89–93. DOI: 10.1016/S0370-2693(98)01092-2.

[SGM00] G. J. Stephenson, T. Goldman, and B. H. J. McKellar. “Tritium beta decay, neutrino mass matrices, and interactions beyond the standard model”. *Phys. Rev. D* 62 (2000), p. 093013. DOI: 10.1103/PhysRevD.62.093013. arXiv: 0006095 [hep-ph].

[SH11] A. Sejersen Riis and S. Hannestad. “Detecting sterile neutrinos with KATRIN like experiments”. *J. Cosmol. Astropart. Phys.* 2011 (2011), p. 011. DOI: 10.1088/1475-7516/2011/02/011. arXiv: 1008.1495.

[Sha08] M. Shaposhnikov. “The νMSM, leptonic asymmetries, and properties of singlet fermions”. *J. High Energy Phys.* 2008 (2008), pp. 008–008. DOI: 10.1088/1126-6708/2008/08/008.

[SHW11] A. Sejersen Riis, S. Hannestad, and C. Weinheimer. “Analysis of KATRIN data using Bayesian inference”. *Phys. Rev. C* 84 (2011), p. 045503. DOI: 10.1103/PhysRevC.84.045503. arXiv: 1105.6005.

[SJF00] A. Saenz, S. Jonsell, and P. Froelich. “Improved molecular final-state distribution of HeT^+ for the beta-decay process of T_2”. *Phys. Rev. Lett.* 84 (2000), pp. 242–245. DOI: DOI10.1103/PhysRevLett.84.242.

[SM75] G. Senjanović and R. N. Mohapatra. “Exact left-right symmetry and spontaneous violation of parity”. *Phys. Rev. D* 12 (1975), pp. 1502–1505. DOI: 10.1103/PhysRevD.12.1502.

[Ste+13] N. Steinbrink et al. “Neutrino mass sensitivity by MAC-E-Filter based time-of-flight spectroscopy with the example of KATRIN”. *New J. Phys.* 15 (2013), p. 113020. DOI: 10.1088/1367-2630/15/11/113020. arXiv: 1308.0532.

[Ste+17a] N. M. N. Steinbrink, J. D. Behrens, S. Mertens, P. C.-O. Ranitzsch, and C. Weinheimer. “keV-Scale Sterile Neutrino Sensitivity Estimation with Time-Of-Flight Spectroscopy in KATRIN using Self Consistent Approximate Monte Carlo” (2017). Submitted to EPJ C. arXiv: 1710.04939.

[Ste+17b] N. M. N. Steinbrink et al. “Statistical sensitivity on right-handed currents in presence of eV scale sterile neutrinos with KATRIN”. *J. Cosmol. Astropart. Phys.* 06 (2017), p. 015. DOI: 10.1088/1475-7516/2017/06/015.

[Str+14] S. Streubel et al. “Toward a more accurate Q value measurement of tritium: status of THe-Trap”. *Appl. Phys. B* 114 (2014), pp. 137–145. DOI: 10.1007/s00340-013-5669-x.

[Ter06] C. J. F. Ter Braak. “A Markov Chain Monte Carlo version of the genetic algorithm Differential Evolution: Easy Bayesian computing for real parameter spaces”. *Stat. Comput.* 16 (2006), pp. 239–249. DOI: 10.1007/s11222-006-8769-1.

[TG79] S. Tremaine and J. E. Gunn. "Dynamical Role of Light Neutral Leptons in Cosmology". *Phys. Rev. Lett.* 42 (1979), pp. 407–410. DOI: 10.1103/PhysRevLett.42.407.

[Val+11] K. Valerius et al. "Prototype of an angular-selective photoelectron calibration source for the KATRIN experiment". *J. Instr.* 6 (2011), p. 01002. DOI: 10.1088/1748-0221/6/01/P01002.

[Val09] K. Valerius. "Spectrometer-related background processes and their suppression in the KATRIN experiment". PhD Thesis. Westfälische Wilhelms-Universität Münster, 2009.

[Val10] K. Valerius. "The wire electrode system for the KATRIN main spectrometer". *Prog. Part. Nucl. Phys.* 64 (2010), pp. 291–293. DOI: 10.1016/j.ppnp.2009.12.032.

[Veg+13] H. J. de Vega, O. Moreno, E. Moya de Guerra, M. Ramón Medrano, and N. G. Sánchez. "Role of sterile neutrino warm dark matter in rhenium and tritium beta decays". *Nucl. Phys. B* 866 (2013), pp. 177–195. DOI: 10.1016/j.nuclphysb.2012.08.019. arXiv: 1109.3452.

[Vie+05] M. Viel, J. Lesgourgues, M. G. Haehnelt, S. Matarrese, and A. Riotto. "Constraining warm dark matter candidates including sterile neutrinos and light gravitinos with WMAP and the Lyman α forest". *Phys. Rev. D* 71 (2005), p. 063534. DOI: 10.1103/PhysRevD.71.063534. arXiv: astro-ph/0501562.

[VSS14] H. J. de Vega, P. Salucci, and N. G. Sanchez. "Observational rotation curves and density profiles vs. the Thomas-Fermi galaxy structure theory". *Mon. Not. R. Astron. Soc.* (2014), pp. 2717–2727. DOI: 10.1093/mnras/stu972. arXiv: 1309.2290.

[Wat+06] C. R. Watson, J. F. Beacom, H. Yüksel, and T. P. Walker. "Direct x-ray constraints on sterile neutrino warm dark matter". *Phys. Rev. D* 74 (2006), pp. 1–7. DOI: 10.1103/PhysRevD.74.033009. arXiv: astro-ph/0605424 [astro-ph].

[Wei+93] C. Weinheimer et al. "Improved limit on the electron-antineutrino rest mass from tritium β-decay". *Phys. Lett. B* 300 (1993), pp. 210–216. DOI: 10.1016/0370-2693(93)90355-L.

[Wei03] C. Weinheimer. "Laboratory Limits on Neutrino Masses". In: *Neutrino Mass*. Ed. by G. Altarelli and K. Winter. Vol. 190. Springer Tracts in Modern Physics. Springer Verlag Berlin Heidelberg New York, 2003, pp. 25–51. ISBN: 3-540-40328-0.

[WLP12] C. R. Watson, Z. Li, and N. K. Polley. "Constraining sterile neutrino warm dark matter with Chandra observations of the Andromeda galaxy". *J. Cosmol. Astropart. Phys.* 2012 (2012), pp. 018–018. DOI: 10.1088/1475-7516/2012/03/018. arXiv: 1111.4217.

[Wol78] L. Wolfenstein. "Neutrino oscillations in matter". *Phys. Rev. D* 17 (1978), pp. 2369–2374. DOI: 10.1103/physrevd.17.2369.

[Wor89] J. Worrall. "Structural Realism: The Best of Both Worlds?" *dialectica* 43 (1989), pp. 99–124. DOI: 10.1111/j.1746-8361.1989.tb00933.x.

[Wu+57] C. S. Wu, E. Ambler, R. W. Hayward, D. D. Hoppes, and R. P. Hudson. "Experimental Test of Parity Conservation in Beta Decay". *Phys. Rev.* 105 (1957), pp. 1413–1415. DOI: 10.1103/physrev.105.1413.

[YBW08] H. Yüksel, J. F. Beacom, and C. R. Watson. "Strong upper limits on sterile neutrino warm dark matter". *Phys. Rev. Lett.* 101 (2008), pp. 1–4. DOI: 10.1103/PhysRevLett.101.121301. arXiv: arXiv:0706.4084v2.

List of Figures

List of Tables

List of Abbreviations

$0\nu\beta\beta$	Neutrinoless Double Beta Decay
$2\nu\beta\beta$	Two Neutrino Double Beta Decay
BAO	Baryonic Acoustic Oscillations
BBN	Big Bang Nucleosynthesis
CC	Charged Current
CDM	Cold Dark Matter
C.L.	Confidence Level
CMB	Cosmic Microwave Background
CνB	Cosmic Neutrino Background
CPS	Cryogenic Pumping Section
DEMC	Differential Evolution Monte Carlo
DPS	Differential Pumping Section
FPD	Focal Plane Detector
GF	Gated Filter
GUT	Grand Unified Theory
HDM	Hot Dark Matter
HF	High Frequency
LMA	Large Mixing Angle
LRSM	Left-Right Symmetric Model
LSS	Large Scale Structure
MAC-E-Filter	Magnetic Adiabatic Collimation with an Electrostatic Filter
MC	Monte Carlo
MCMC	Markov Chain Monte Carlo
MMC	Metallic Magnetic Calorimeter
MSW	Mikheyev–Smirnov–Wolfenstein effect
NC	Neutral Current
νMSM	Neutrino Minimal Standard Model
PIN	Positive-Intrinsic-Negative
PMNS	Pontecorvo-Maki-Nakagawa-Sakata matrix
QD	Quasi-Degenerate scenario
SM	Standard Model
SNP	Solar Neutrino Problem
SBL	Short Baseline
SCIS	Self Consistent Importance Sampling
SDS	Spectrometer and Detector Section
SQUID	Superconducting Quantum Interference Device
TOF	Time-Of-Flight
VEV	vacuum expectation value
WDM	Warm Dark Matter
WIMP	Weakly Interacting Massive Particle
WGTS	Windowless Gaseous Tritium Source

Curriculum Vitae

Personal Information

Name	Nicholas Martin Norman Steinbrink
Date of Birth	July 25th 1985
Place of Birth	Soest, Germany
Nationality	German

Education

2012 – 2017	PhD in Physics, University of Münster, Germany
11/2015 – 02/2016	Research Project at Aarhus University, Denmark
2005 – 2012	Diploma in Physics, University of Münster, Germany
09/2007 – 06/2008	Erasmus Exchange Student, University of Lund, Sweden
1996 – 2005	Abitur, Archigymnasium Soest, Germany

Awards

2012	1st Price, Essay Competition, Center for Philosophy of Science, University of Münster

Publications

First Author

2013	N. Steinbrink et al., Neutrino mass sensitivity by MAC-E-Filter based time-of-flight spectroscopy with the example of KATRIN, New J. Phys. 15 (2013) 113020
2017	N. Steinbrink et al., Statistical sensitivity on right-handed currents in presence of eV scale sterile neutrinos with KATRIN, arXiv:1703.07667, submitted to JCAP

Co-Authored

2015	S. Mertens et al., Sensitivity of next-generation tritium beta-decay experiments for keV-scale sterile neutrinos, JCAP 02 (2015) 020
2016	M. Arenz et al. (KATRIN Collaboration), Commissioning of the vacuum system of the KATRIN Main Spectrometer, JINST 11 (2016) P04011
2017	R. Adhikari et al., A White Paper on keV sterile neutrino Dark Matter, JCAP 01 (2017) 025

Acknowledgements

These couple of pages called "thesis", distilled from blood, sweat and tons of freshly brewed coffee, would not have been possible without all these helpful and dear people who supported me. In particular, I would like to thank:

- My supervisor, Christian Weinheimer, for all the selfless work he has invested to ensure that my thesis would become a success and for supporting me even in difficult times.
- Gernot Münster, for evaluating the thesis as second reviewer, additional supervision within the graduate school and interesting philosophical discussions.
- Steen Hannestad, for inviting me to Aarhus, teaching me the mysterious ways of theoretical particle physics and ensuring that I had a great stay.
- Alexander Kappes for agreeing to be the third examiner for the disputation.
- My long-term office buddy, Jan Behrens, for his outstanding support, proof-reading my thesis, teaching me the plethora of collaboration-internal analysis tools and installing $n \to \infty$ packages on my office PC.
- The Hand of the King, Volker Hannen, for additional supervision and help, being always down-to-earth and having great musical taste.
- The whole AG Weinheimer crew, including all old veterans, for an uncomplicated working atmosphere, taking care of each other and lots of dark humour at the coffee round. In order of appearance: Hans-Werner Ortjohann, Michael Zacher, Stephan Rosendahl, Daniel Winzen, Olli Rest, Alex Fieguth, Michael Murra, Stephan Dyba, Maik Schneider, Raffi Busse, Philipp C.-O. Ranitzsch, Simon Peters, and Rudolf Sack.
- All organizers and members of the DFG graduate school 2149 for great research and learning opportunities, a pleasant discussion atmosphere and tearing down the invisible wall between theoretical and experimental physics.
- The IP@WWU program for funding my stay abroad.
- Kathrin Valerius, Marco Kleesiek, Florian Heizman and Ferenc Glück for collaborating with me on right-handed currents, inviting me to Karlsruhe and increasing my Bayesian inference skills.
- Hamish Robertson and Eric Martin for their contributions to our time-of-flight paper and their dedicated work on electron tagging.
- Our institute secretaries, Uta Mayer, Michaela Erdmann and Petra Voß for all their work and being patient with me when i accidentally forgot to hand in a form or to pay my coffee bill.

Last but not least I would like to thank my girlfriend Hanna, my sister Johanna, my brother-in-law Daniel, my parents, Axel and Ursel, my grandparents, Thea and Fritz, my parents-in-law to be, Ulli and Holger and my grandparents-in-law to be, Ulla and Martin, for being so patient, always believing in me and being there.

```
 *   *
   u
\___/
 v v
```